1992-04-15

Ocean general circulation from a global eddy-resolving model

Semtner, Albert J., Jr.

American Geophysical Union

Journal of Geophysical Research, v. 97, no. C4, April 15, 1992, pp.5493-5550.

JOURNAL OF GEOPHYSICAL RESEARCH, VOL. 97, NO. C4, PAGES 5493–5550, APRIL 15, 1992

Ocean General Circulation From a Global Eddy-Resolving Model

ALBERT J. SEMTNER, JR.

Naval Postgraduate School, Monterey, California

ROBERT M. CHERVIN

National Center for Atmospheric Research, Boulder, Colorado

A concerted effort has been made to simulate the global ocean circulation with resolved eddies, using a highly optimized model on the best available supercomputer. An earlier 20-year spin-up has been extended for 12.5 additional years: the first 2.5 with continued annual mean forcing and the final 10.0 with climatological monthly forcing. Model output archived at 3-day intervals has been analyzed into mean fields, standard deviations, products, and covariances on monthly, annual, and multiyear time scales. The multiyear results are examined here in order to give insight into the general circulation of the world ocean. The three-dimensional flow fields of the model are quite realistic, even though resolution of eddies in high latitudes is marginal with a 0.5°, 20-level grid. The use of seasonal forcing improves the simulation, especially in the tropics and high northern latitudes. Mid-latitude gyre circulations, western boundary currents, zonal equatorial flows, and the Antarctic Circumpolar Current (ACC) all show mean and eddy characteristics similar to those observed. There is also some indication of eddy intensification of the mean flow of the ACC and of separated boundary jets. A global thermohaline circulation of North Atlantic Deep Water is identified in deep western boundary currents connected by the ACC. This deep circulation rises mainly in the equatorial Pacific. Several zonal jets are an integral part of this circulation near the equator. The deep flow rises toward the surface in a series of switchbacks. Much of the thermohaline return flow then follows an eddy-rich warm-water route through the Indonesian archipelago and around the southern tip of Africa. However, some intermediate level portions of the thermohaline circulation return south into the ACC and follow a cold water route through the Drake Passage. The representation of a global "conveyor belt" circulation with narrow and relatively high-speed currents along most of its path may be the most important result of this modeling study. Statistics of scalar fields such as transport stream function and surface height are exhibited, as are time series and frequency spectra of certain variables at selected points. These provide a baseline for comparison both with observations and with other model studies at higher resolution. Mean and eddy characteristics of the near-surface temperature and salinity fields are discussed, and surface forcing fields are examined. In particular, combined thermal and hydrological forcing effects are found to drive a conveyor belt circulation between the tropical Pacific and the high-latitude North Atlantic. The effect of weak restoring terms to observed temperature and salinity at great depth and in polar latitudes is found mainly to augment the model's convective processes, which are poorly resolved with 0.5° grid spacing. However, the deep restoring terms are insignificant in both the tropics and the mid-latitudes. The geographical distributions of eddy heat and salt transport are discussed. The eddies transport heat and salt down the gradients and along the mean flow in many regions of strong currents. Net meridional transports of heat and salt by both the total currents and the eddies are computed for the Atlantic, the Indo-Pacific, and the global ocean. The total currents provide for poleward heat transport (except near 40°S, where the contribution from ACC instabilities is rather weak) and, in particular, for that needed to sustain the conveyor belt transport. Meridional eddy transports are especially important for warming the Pacific upwelling branch of the thermohaline circulation and for transporting salt across the equator into the North Pacific. Planned improvements to the model include a free-surface treatment of the barotropic mode and additions of the Arctic Basin and sea ice. A fully prognostic extension of the existing integration is intended, with subsequent transitioning of the model onto a 0.25° grid having very realistic geometry. The 0.25° version of the model will run effectively on newly available supercomputers.

1. INTRODUCTION

A previous study [*Semtner and Chervin*, 1988] has demonstrated the feasibility of modeling the global ocean circulation with resolved eddies. The phenomenology of unstable currents in a number of geographic regions was investigated in that paper. Subsequently, additional model integrations and extensive analyses of model output have been carried out, in order to permit examination of the statistics and dynamics of ocean circulation. The phenomenology of a new, seasonally forced phase has been illustrated in a videotape animation of temperature and salinity fields and particle trajectories prepared by M. McCann (personal communication, 1991). VHS copies of that tape are available in American NTSC or European PAL format from the authors of the present paper upon request. This paper describes the mean fields and statistical variability of the model ocean, as well as the maintenance of the circulation by fluxes and transports which include the effects of explicitly resolved eddies. Some of the effects which can be attributed to seasonal forcing are examined as well. The goal is thus to describe the oceanic general circulation, as portrayed by the global model.

Global ocean modeling plays a prominent role in ongoing programs such as the World Ocean Circulation Experiment

Paper number 92JC00095.
0148-0227/92/92JC-00095$05.00

(WOCE) and the Global Change Research Program. The primary objectives of these international efforts are to understand global ocean circulation and to improve our ability to predict global climate change, respectively. To the extent that the present study is successful in portraying the ocean general circulation, the existing model output can be further analyzed for dynamical information relevant to WOCE, and the model itself can be more confidently employed in studies of global climatic change.

Aside from programmatic needs for a treatment of the whole ocean, there are sound physical reasons for studying the entire ocean. Two prominent global-scale ocean circulations, namely the thermohaline "conveyor belt" and the Antarctic Circumpolar Current (ACC), are difficult to treat on an individual or partial basis. As will be seen in this paper, these two circulations interact extensively with each other, via both mean and eddy flows; and the two are jointly affected by thermohaline and wind forcing. Thus many ocean regions and processes are significantly interdependent, and the use of a global model is advisable.

Previous ocean modeling studies with resolved eddies have been regional in extent, in order to maximize local resolution. Recent examples with realistic geometry and active thermodynamics are the U.S./German Community Modeling Effort (CME) for the North Atlantic [*Bryan and Holland*, 1989; *Schott and Böning*, 1991; *Böning et al.*, 1991] and the U.K. Fine Resolution Antarctic Model [*FRAM Group*, 1991]. By employing a highly optimized ocean model, it is possible to approach the resolution of these regional models on a global basis. In the present study, the discussion of specific phenomena within regions is not emphasized, although the quality of representation of many features is often comparable to that from regional models. Instead, global-scale ocean currents are emphasized, such as the three-dimensional thermohaline circulation and the ACC. Also, exchanges between regions (which are often specified ad hoc in regional models) are examined here and are discussed further in a forthcoming paper by M. P. McCann et al. (Volume, heat, and self budgets and transports from a global eddy-resolving ocean model, submitted to *Journal of Geophysical Research*, 1992, hereinafter referred to as McCann et al., 1992). However, much of the material is presented through large global maps which not only provide a unified global view but also give sufficient detail for those readers who may be especially interested in specific areas.

Section 2 describes the model strategy that was employed in the simulation and analysis of global circulation with resolved eddies. Vector maps of near-surface, thermocline, deep, and abyssal flow fields are discussed in section 3. Section 4 describes the three-dimensional structure of a simulated global conveyor belt circulation. Section 5 describes the spatial and temporal aspects of model variability. Sections 6 and 7 analyze the fields of temperature and salinity and the transports and fluxes of heat and salt. Section 8 summarizes the results, section 9 describes intended future studies, and section 10 has some final remarks.

2. STRATEGY

The construction of the global model and the preparation of the bathymetric and forcing fields are described by *Semtner and Chervin* [1988] and *Chervin and Semtner* [1990]. The unique feature of the model to date is its simultaneous use of all available processors on parallel vector supercomputers, while retaining relatively minimal memory requirements, in order to make global eddy-resolving calculations feasible and reasonable. The algorithms of the model derive from *Bryan*'s [1969] multilevel, primitive equation formulation, with specific versions due to *Cox* [1970, 1984] and *Semtner* [1974]. Vertical mixing is parameterized according to the method of *Pacanowski and Philander* [1981]. Surface fluxes of heat and salt are prescribed via the method of *Haney* [1971], using observed reference fields of surface temperature and salinity.

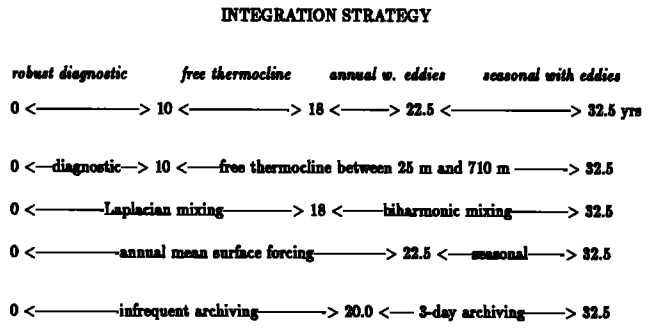

Fig. 1. Schematic for the overall time integration in simulated years.

All of the simulations described in this paper use 0.5° grid spacing in both latitude and longitude, with a maximum of 20 vertical levels in the deep ocean. To compare against regional studies with similar model formulations, the CME calculations with 0.33° by 0.4° horizontal grid structure and the FRAM simulations with 0.25° by 0.5° grid structure both have about twice as many horizontal grid points per unit area. Those two models have 30 and 32 vertical levels, respectively, so that all models have about the same ability to represent topographic slopes.

If prescribed internal damping is sufficiently small, a horizontal grid spacing of 0.5° degree or less will allow the explicit representation of some instabilities which mix momentum, heat, salt, and other properties in the ocean. In such circumstances, the models are "eddy-resolving," and they should begin to reproduce the state of the ocean from first principles. An additional desirable feature in such models is the capability to perform extended simulations on climatic time scales, as has been done by *Toggweiler et al.* [1989]. At present, the latter capability can only be attained by sacrificing grid resolution. As computer speed dramatically increases over the next decade, it will be possible to combine both eddy resolution and extended integrations to address climate issues. In the meantime, we shall investigate here the statistical equilibrium of present-day ocean circulation with some portion of resolved eddies.

Figure 1 illustrates the methodology of a 32.5-year simulation, the first 20 years of which are discussed by *Semtner and Chervin* [1988]. The methodology was designed to yield as much information as possible from the finite computational resources, in order to maximize the possible scientific payoff. Four phases of progressively increasing realism are involved: robust diagnostic, free thermocline, annual mean forcing with eddies, and seasonal forcing with eddies. The first two phases are similar to those in an Atlantic study of *Sarmiento and Bryan* [1982]. Weak restoring to observed gridded temperature and salinity data is used, first through-

out the water column and then primarily below the thermocline, to obtain quasi-steady, near-equilibrium ocean circulation that is consistent with the present-day density structure of the deep ocean. The last two phases allow eddies as a result of using scale-selective biharmonic mixing in the horizontal in place of Laplacian mixing.

The phase with seasonal forcing is new to this study and required the use of monthly wind forcing from *Hellerman and Rosenstein* [1983] and surface temperature and salinity on a respective monthly and seasonal basis from *Levitus* [1982]. These fields were spline interpolated to daily values for updating of forcing every 3 days in the running model. Since the seasonal cycle experiment is the culmination of the integration steps, we will sometimes refer to its specific time period as "years 1–10," leaving out the 22.5-year period of spin-up to quasi-equilibrium.

The use of the robust diagnostic method throughout the deep ocean (and in the thermocline within 10° of the southern and northern walls) gives assurance that the simulated circulation will not experience a long-term climatological drift. Equilibrium will be attained on the time scale of the upper 710 m, which is of the order of decades. The adjustment that takes place in the deep ocean, as constrained on a 3-year time scale to the historical observations, will be of two types. The first type of adjustment is one in which the model can horizontally "unsmooth" the observations, as gridded by *Levitus* [1982] with approximately a 4° smoothing. If deep velocities are of the order of 1 cm s^{-1}, then length scales of the order of 1000 km can be unsmoothed on a 3-year time scale. The second type of adjustment is one to remedy model deficiencies in certain vertical processes such as the physics of convection in the production of deep water masses or the dynamics of dense plumes descending continental slopes away from production regions. It is expected that the 3-year restoring time scale can have the benefits of not restricting local adjustments while providing for the effects of some unresolved physical processes.

The recent study by *Toggweiler et al.* [1989] indicates that the robust diagnostic method does not work well in certain situations. However, the quality of their simulated circulation was significantly impacted by the coarse (4°) grid, by high viscosity, by lack of seasonal forcing, and by the absence of a free thermocline. In the present study, these four shortcomings are alleviated in the hope of obtaining an improved high-resolution simulation, consistent with existing water mass distributions and without a prohibitively expensive calculation. One expects that in the limit of increasing resolution and improving physics, the effects of deep restoring terms become small in simulating present-day ocean circulation.

Figure 1 also indicates that history tapes were archived every 3 days beginning at year 20 of the simulation. A history tape has values of almost all model variables at every grid point for one instant of time. Each tape has approximately 20 megawords of output and contains the net results of about one-half hour of Cray X-MP/48 wall clock time. The 3-day tapes were analyzed by a procedure which produced monthly, annual, and multiyear tapes of mean quantities, standard deviations, selected products, and selected covariances. Output tapes from this procedure could then be viewed using a processing program [*Bettge*, 1987], which creates contour and vector maps and does time and space averaging as well. This program was further modified (McCann et al., 1992) to provide budget estimates of various quantities on a two- or three-dimensional basis. Additional tapes were produced from those described above to give ensemble statistics over the final 5 years of the seasonal run. These were made for the individual months of the year, and ensemble statistics for yearlong quantities were also generated. The totality of all tapes, which exceeds 250 gigabytes in size, is available on the Mass Storage System at the National Center for Atmospheric Research (NCAR).

3. CIRCULATION

It is a challenge to try to depict the flow fields of the global ocean with adequate spatial resolution. On the one hand, it is desirable to show the entire circulation, because of the interconnectedness of ocean currents. On the other hand, it is desirable to have vectors spaced at some fraction of a degree in latitude and longitude in order to adequately represent narrow but important currents. In this paper, fully global maps of velocity vectors at all horizontal grid points are shown as foldouts. These maps are given for four depth ranges that suitably characterize the vertical structure of the flows, namely, the near-surface (0–135 m), the thermocline (135–1000 m), the deep (1000–3300 m), and the abyssal (3300–5200 m). In each depth range, strong currents appear at first glance as dark ribbons and weak currents appear as shading. Individual current vectors can be discerned upon closer inspection. In most areas, quantitative information can be recovered from the plots, although information is sometimes obscured in regions of strong currents. However, the present maps have been chosen to show as much information as possible within the limitations of journal publication.

The vector plots in an given depth range actually show vertical integrals over that range for valid ocean points in each horizontal location, and thus they represent (areal) transports. This portrays the flows relatively smoothly, even in the abyssal range where bottom topography is quite variable. The vector plots for different vertical ranges can be easily intercompared in terms of transport. The flows in the near-surface and abyssal ranges have an identical transport scale such that 2.0° latitude/longitude equal 2500 m cm s^{-1}. Arrows in both the thermocline and deep ranges represent twice as much transport per unit length, i.e., an arrow of length 2.0° in latitude/longitude represents a transport of 5000 m cm s^{-1}.

Plates 1, 2, and 3 in succession show the near-surface time-averaged flow from the final 900 days of the experiment with annual mean forcing, the instantaneous flow in early October during year 10 with seasonal forcing, and the time-averaged flow for years 6–10 of the seasonal run. Plates 1 and 3 can be compared to see the effect of seasonal forcing on long-term flow patterns, and Plates 2 and 3 can be unfolded side by side to ascertain some instantaneous eddy characteristics. For the near-surface flows in Plates 1–3 a vector of 2° latitude/longitude in length has a speed of 18.5 cm s^{-1}. (This is just 2500 m cm s^{-1} divided by the 135-m depth range.) In all the vector plots, arrows longer than 4° are truncated to that size. Descriptions of the figures will concentrate on the most important aspects of the strong currents and on global interconnections.

Plate 1 shows a time mean Florida Current emanating from the Caribbean Sea and separating as a Gulf Stream near 37°N

in a standing-wave pattern. East of the area of the Grand Banks, an organized North Atlantic Current nearly reaches Ireland before turning north and connecting broadly at the closed 65°N wall to the East Greenland and Labrador currents. (The north wall of the global model is closed in a fashion similar to that of the CME models of the North Atlantic, involving restoring to observed temperature and salinity there but no mass flux through the wall.) In the tropical Atlantic, a strong North Brazil Current feeds eastward flow on the equator and retroflects mainly at 10°N. The South Atlantic has a complex and filamented Antarctic Circumpolar Current, which is fed by the Brazil Current from the north and by a double jet through the Drake Passage. The northernmost ACC filament that emanates from the Brazil-Malvinas (Falkland) confluence moves zonally across the Atlantic at about 40°S, passes close to and receives mass from the Agulhas Current and Retroflection, and proceeds across the South Indian Ocean.

In the north Indian Ocean, strong Indonesian throughflow enters via the Makassar Strait along the east side of the model's Southeast Asian landmass. The flow moves zonally across the Indian Ocean to the northeast coast of Madagascar. Thereupon, part of the flow forms an African Coastal Current which separates near the equator and diffusely joins the South Equatorial Countercurrent (SECC) flowing toward Indonesia. The rest of the throughflow volume converges onto the coast of Madagascar as it forms the East Madagascar Current, which then feeds the Agulhas Current. In the Arabian Sea, a circular flow near the Gulf of Aden is fed by a weak current along the Somali coast.

In the North Pacific, an intense recirculating gyre near the western boundary is fed by a broad part of the North Equatorial Current (NEC). It separates from the coast mainly south of Honshu in a Kuroshio Current and secondarily south of Hokkaido in an Oyashio Current. Subarctic latitudes have an Alaska Stream and a coastal part of the Oyashio flow that are weakly connected across the Bering Sea. In the low latitudes of the western Pacific, an intense part of the NEC feeds the Indonesian throughflow via the Mindanao Current (which is west of the slightly submerged island of the same name), and it also feeds the North Equatorial Countercurrent (NECC). Zonal currents such as the NECC, an equatorial part of the South Equatorial Current (SEC), and the flow feeding the Equatorial Undercurrent (EUC) are all displaced north of their mid-ocean latitudes by the presence of New Guinea and its coastal current. In the middle two thirds of the tropical Pacific, these currents are extremely zonal and located at their usual observed latitudes.

The South Pacific has a weak SECC, which splits the SEC and is fed by a recirculation southeast of New Guinea. Currents in the mid-latitude South Pacific are rather weak, including the East Australia Current, which flows zonally across the north end of the Tasman Sea and feeds the East Auckland Current. South of Tasmania, the intense ACC follows a path which is constrained by the subsurface Macquarie Rise and the Campbell Plateau. East of New Zealand, the ACC converges gradually toward the location (130°W, 55°S) of the Udintsev Fracture Zone between the East Pacific Rise and the Pacific-Antarctic Ridge. In the southeast Pacific, the ACC is weak and broad until it approaches the Drake Passage. Finally, in the eastern tropical Pacific, the NECC turns north along the Central American coast, and the EUC turns south back into the SEC.

Plate 2 shows instantaneous flows in the 0- to 135-m depth range for early October during year 10 of the seasonal run. It can be contrasted with the time mean flows of Plates 1 and 3 (which are nearly identical to each other). Closed eddies are identifiable in a number of areas, and waves superimposed on strong mean flows are evident in very many places. Generally speaking, the mid- and high-latitude eddies and meanders tend to have wavelengths of about 4° longitude (i.e., 8 grid points), while those in low latitudes span 8°–10° longitude (or 16–20 grid points). The grid really cannot resolve waves smaller than eight grid points in wavelength, even though some smaller waves may be maximally unstable. Both the friction and the grid truncation tend to eliminate them. Thus the eddies are probably well resolved in the tropics, suitably resolved in the subtropics, and marginally to poorly resolved in the middle to high latitudes.

The overall performance of the present model in treating eddies is consistent with a recent study which compares North Atlantic model results of the CME and Geosat observations [*Stammer and Böning*, 1992]. That study shows observed eddy scales to be dictated by the local radius of deformation. Because this length scale decreases as latitude increases, there is a need for finer grid meshes, if eddies are to be resolved at high latitudes. Thus the present study represents only the beginning of an effort to resolve eddies on a global basis, and higher resolution will be needed to represent adequately the length scales and energy levels of eddies at high latitudes.

As can be seen from the snapshot of circulation, closed eddies occur in such places as the Gulf of Mexico, the Caribbean Sea, the Agulhas Extension region, the Kuroshio recirculation, the East Australia Current, the Pacific equatorial current system, the Indonesian throughflow, the Somali Current, the East Madagascar Current, the Agulhas Current, and certain parts of the Antarctic Circumpolar Current. Weak eddies exist in some eastern boundary regimes, such as east of Central America and in the Leeuwin Current and the California Current. The videotape animations of temperature and salinity which were mentioned earlier show these features (and eddies in other areas as well) in relatively clear fashion; and formation, growth, and decay of eddies are all visible.

Almost all of the strong currents of the model show some degree of meandering, over and above that of any standing waves that may exist, for example, in high-latitude flow patterns. Many of these currents would undoubtedly shed eddies in higher-resolution simulations. In addition, there are many fluctuations on the weaker but still identifiable currents of the mid-ocean basins. In video animations of temperature and salinity, many of these latter features are advected along by the mean flow of the gyre circulations.

A look at Plate 3 (with 5-year average currents from the seasonally forced run) shows very little difference relative to the annually forced case of Plate 1. This is quite surprising, since some of the currents have a pronounced seasonal cycle, as is also evident in animations. Virtually the only significant differences other than in the Somali Current (which actually reverses on a seasonal basis) are in some of the separated high-velocity jets. Thus the Kuroshio Current, the Brazil-Malvinas confluence, the East Australia Current, the Pacific NECC, and the North Brazil Current show

offshore intensification with seasonal forcing. (For the Indian Ocean, very significant changes have occurred in the structure of the SECC and a separating Somali Current which feeds a Wyrtki jet on the equator; also, the Leeuwin Current is stronger with seasonal forcing.)

The increased offshore extension of separated jets in the seasonally forced case may be a sign of continuing adjustment of the free thermocline over an additional simulated time of almost 9 years. However, it is more likely to be a sign of nonlinearity in the seasonal cycle of these currents. The sequential design of the experiments makes it difficult to isolate the exact cause.

Thermocline flows in the depth range 135–1000 m are shown in Plates 4 and 5. They appear side by side in the foldout set to allow comparison of the instantaneous flow at year 18 for Laplacian mixing with the time-averaged flow with biharmonic mixing. An arrow 2° long represents a depth-averaged speed of 5.8 cm s^{-1} (as obtained by dividing the transport scale of 5000 m cm s^{-1} by the 865-m thickness). The instantaneous Laplacian case is nearly steady, aside from large-scale tropical waves in the Pacific and Indian Oceans. These waves may have been excited in spite of strong friction by the asynchronous time stepping that was used to accelerate the model integration up to year 18. Using a longer time step on temperature and salinity than on the momentum variables can lead to spurious baroclinic instabilities [*Bryan*, 1984].

Some of the strong mean currents of the biharmonic case are severely reduced by the Laplacian mixing of only 10^7 cm^2 s^{-1}. These include the Gulf Stream, the Kuroshio, the East Australia Current, and major portions of the Antarctic Circumpolar Current. Other currents such as the East Madagascar Current, the Agulhas Current, the Equatorial Undercurrent, and the North Brazil Current, are hardly affected. Some of the former currents may derive part of their strength and small width scale from the negative viscosity effect of baroclinic instability.

The fact that some strong currents cannot be well reproduced by a quasi-steady realization using Laplacian mixing at even 0.5° grid spacing may be a deficiency in regard to climate modeling. One would hope to represent time mean flows with proper size and intensity and be able to use accelerated time stepping on occasion because of quasi-steadiness. Parameterizing eddy effects at 0.5° grid size will be difficult numerically, since the positive Laplacian viscosity is already reduced as much as possible without exciting computational noise.

Plate 5 can be compared with Plate 3 to see that most of the high-latitude surface currents have significant extensions into 135- to 1000-m depths, but most of the tropical currents do not. Significant exceptions to the latter are the New Guinea Coastal Undercurrent and the Equatorial Undercurrent into which it retroflects. Note that there are subsurface westward flows in the 15°–25°S latitude belt of the Indian Ocean and in the 25°–35°S belt of the Atlantic Ocean. Some of the flow that rounds the tip of Africa seems to retain enough vorticity from its Indian Ocean crossing to make a northward swing to about 30°S before transiting the Atlantic. As will be seen later, these flows are strong because they are parts of the simulated thermohaline circulation between the tropical Pacific and the North Atlantic. Also, a recognizable northward flow along the east coasts of South America and North America begins near 30°S where the Atlantic cross-flow meets the coast.

Plates 6–8 depict simulated deep circulation in the depth range 1000–3300 m. An arrow 2° in length represents a layer-averaged speed of 2.2 cm s^{-1}, and speeds greater than 4.4 cm s^{-1} are truncated to that value.

Plate 6 shows the deep instantaneous motion field at the same time as for the near-surface fields of Plate 2. Closed eddies are found throughout much of the global domain. In spite of the presence of robust diagnostic forcing, these features appear to be relatively unaffected. Only the areas which are known from recent Geosat observations to be relatively eddy-free also appear as such in the model. These eddy deserts include large parts of the mid-latitude eastern Atlantic and Pacific oceans. Note that the ACC is quite strong, highly meandering, and very filamented in the 1000- to 3300-m depth range. Finally, diagonal currents exist on either side of the equator on the east sides of the Indian and Atlantic oceans. These are likely to be transient responses to wind-forced equatorial jets in these ocean basins, following energy reflection at eastern boundaries.

Plate 7 shows instantaneous motion with Laplacian friction at 1000- to 3300-m depth for the same time as for Plate 4. Large-scale tropical waves in both the Indian and Pacific oceans are evident. Although separated western boundary currents have all but disappeared, the ACC remains strong at this depth, indicating no intrinsic difficulty in maintaining strong quasi-steady currents with small cross-stream length scales. (In Plate 8 the deep ACC will be seen to become even stronger when biharmonic mixing is used.) The ACC is the dominant current at this depth, and it receives inflow from all three ocean basins for redistribution along its path.

Plate 7 also shows a pronounced southward moving western boundary undercurrent along the coasts of North and South America. This current was not inherent in the Levitus data because of its small scale. In addition, there is an indication that zonal jets may exist at this depth in the equatorial Pacific, although the tropical waves tend to obscure them in this instantaneous picture. The deep equatorial jets of the tropical Pacific are better seen in Plate 8, which gives the 5-year mean flow for the case with biharmonic mixing and seasonal forcing. There are five jets alternating in direction between westward flow (the central and outermost jets) and eastward flow (the other two). The fact that the jets were already present in the Laplacian case suggests that they are not being maintained by eddy effects from above in the biharmonic case. We shall investigate these jets further in the next section.

Note that the deep western boundary undercurrent in the Atlantic has intensified somewhat over the Laplacian case of Plate 7, as a result of reduced lateral damping of small length scales. Direct calculation of the amount of flow in this current at 5°S gives 14.3 Sv. Also, there are weaker south flowing western boundary currents along the southern parts of Australia and Africa. These flows will also be discussed further in the next section.

Finally, there are noticeable thin currents in Plate 8 which are organized in ways that suggest topographic steering. In fact some of the features that appear thicker, such as the deep equatorial jets and the western boundary undercurrent in the Atlantic, also have relatively thin length scales at individual levels in the model but appear broader because they extend over several model levels. (In the depth range

1000–3300 m, five vertical levels contribute information to the averaged results.)

The deep circulation of the North Atlantic does not show a very well defined boundary flow between 30°N and 50°N. This is probably due in part to the lack of specified inflow at the northern boundary of the model. Most of the southward flow of the deep Labrador Current converges with northward flow off the Grand Banks and proceeds eastward to Porcupine Bank near Ireland. There the flow turns mainly southwest and spreads back into the western boundary region over the latitude range 35°–45°N. Part of the flow also moves to latitudes of 25°–35°N on the east side of the Mid-Atlantic Ridge before crossing westward toward the boundary. The more dominant part of this deep North Atlantic circulation has the structure of an observed gyre which was first described by *Worthington* [1976].

The abyssal flow for the 5-year mean of the seasonally forced experiment is shown in Plate 9. The length scale for flow is now 1.3 cm s^{-1}, with truncation at 2.6 cm s^{-1}. At this depth the division of the ocean domains into subbasins is brought about by the many mid-ocean ridges, some of which have been referred to earlier because of their steering effect on currents. The Antarctic Circumpolar Current is broken into several pockets of deep mean flows, some of which may be maintained by eddy forcing from above. (The abyssal currents were rather weak in the South Atlantic and Southwest Indian oceans until biharmonic friction was used.)

There are abyssal mean flows in the three major ocean basins, although only the Pacific one is strong and clearly defined. In the Indian Ocean, flow enters the south end of the West Australia Basin and moves toward the Ninetyeast Ridge, where a complex pattern of currents exists on either side of the ridge in the latitude range 0°–10°S. In the Atlantic, the most organized flow develops from a confluence of north and south flowing boundary undercurrents which meet at the equator, turn eastward, and pass through the Romanche Fracture Zone. The northward flowing current is the model equivalent for the flow of Antarctic Bottom Water (AABW). Flow then divides to circulate near the equator in the Guinea Basin and to move poleward into an anticyclonic circulation east of the Mid-Atlantic Ridge. South of the equator, there are alternating zonal flows connected along the lateral margins in both the Brazil Basin and the Angola Basin.

In the Pacific, organized flow in the deep ACC south of the Tasman Rise flows south of the Macquarie Rise and around the perimeter of the Campbell Plateau and Chatham Rise, and then proceeds north via several paths across 10°S in the vicinity of the Samoan Passage. At 30°S the transport of the western boundary undercurrent is 9 Sv, and the mid-ocean flow contributes 1–2 Sv more. Between 10°S and 10°N there are complex zonal flows interacting with topography, which will be discussed further in the next section. However, some of the deep flow continues as a western boundary undercurrent to 50°N along deep topography near the Marshall Islands, the Izu Ridge, and the continental slope off Asia. Eastward spreading from the undercurrent toward the interior occurs north of 40°N.

East of the Emperor Seamount Chain near 40°N, there is a southeastward flowing current which feeds into coherent but weak southward flowing currents on the eastern side of the North Pacific. The latter currents follow the very deep topography and may also separate different water mass types, which support vertical shear toward the bottom. The wavy patterns in the northeast Pacific are similar to structures suggested in maps of observed abyssal properties. Many of the remaining deep basins are rather stagnant. These include the North American Basin and the basins east of the East Pacific Rise. In the southernmost basins and near Antarctica, flows move both eastward and westward in the abyss. In particular, some of the flows are moving to the west beneath the ACC south of Africa, northeast of the Falkland Plateau, and north of the Weddell continental slope.

Many of the abyssal circulations are suggestive of flow patterns inferred mainly from observed property distributions [*Mantyla and Reid*, 1983; *Warren*, 1981]. As modeled, their detailed structures are undoubtedly in error as a result of using smoothed topography as well as inadequately known density structure on even the large scale. However, the model characterization of the stronger abyssal currents as relatively well defined entities of fine cross-stream scale is probably quite accurate. It should be mentioned again that such fine scales were not present in the Levitus data set, which has a multidegree smoothing even in the areas with high density of observations. The abyssal currents seem to be manifestations of global water mass movements of the intrinsic fine scale dictated by dynamics, such as the radius of deformation and various length scales of boundary currents. The fact that this is true in the deep water as well as near the surface has important implications for modeling the global thermohaline circulation.

Finally, Plate 10 shows the abyssal circulation from the experiment with annual mean forcing. This differs very little from that with seasonally varying forcing. The similarity of Plates 9 and 10 suggests that modeled deep circulation features on the equator are not related to downward energy propagation from seasonally forced equatorial waves. Such a mechanism is likely to explain certain deep low-frequency phenomena [see *Ponte and Luyten*, 1989]. In the present simulation it cannot be ruled out that the deep restoring terms may be suppressing such effects.

It is difficult to imagine that the robust diagnostic forcing terms are playing very much of a role in constraining the details of the deep and abyssal circulation, since there are quite a number of very zonal flows at depth. Simple conservation of potential vorticity, as demonstrated by such motion, would be easily and visibly disrupted if deep restoring terms were anything but minor. In the interest of thoroughness, however, it makes sense to remove the deep forcing for at least a limited test integration of several years; and such an integration is now underway.

4. Global Conveyor Belt

It is evident from the horizontal flow patterns at various depths that the global ocean simulation has southward motion analogous to that of North Atlantic Deep Water (NADW) in western boundary undercurrents of the Atlantic Ocean and northward transport of abyssal water in western boundary currents of the Pacific Ocean. These circulations are connected by the Antarctic Circumpolar Current. This makes the model circulation relatively consistent with the concept of a global ocean "conveyor belt," as popularized by *Broecker* [1987, 1991]. Since there is near-surface transport through the Indonesian passage, the model results are also consistent with a "warm water" route for replenish-

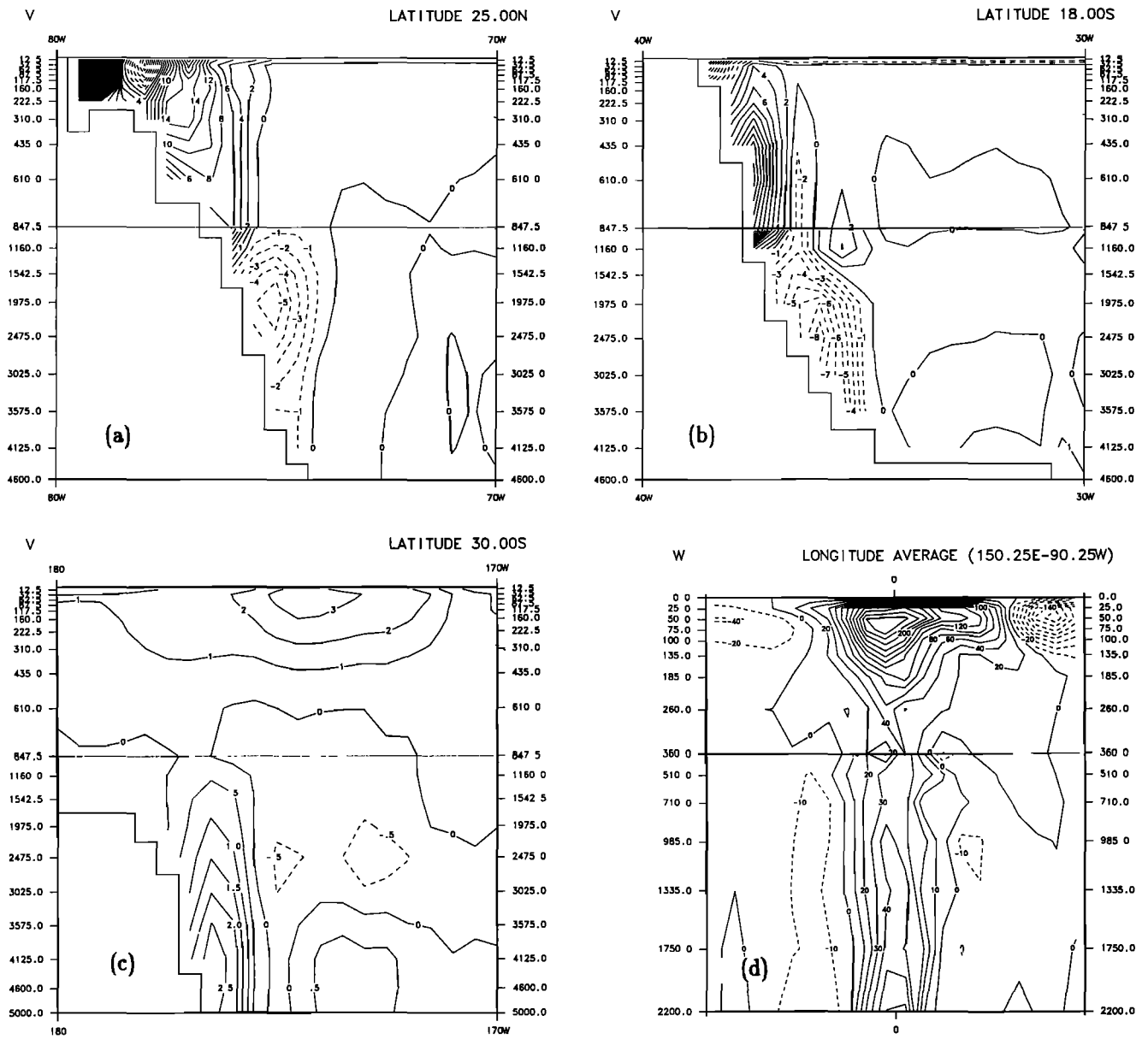

Fig. 2. Time mean meridional velocities (centimeters per second) in (*a*) the North Atlantic, (*b*) the South Atlantic, and (*c*) the South Pacific, and (*d*) vertical velocity (centimeters per day) between 5°S and 5°N, as averaged across the Pacific. Note the varying contour intervals and depth scales.

ment of the NADW source through the Indian Ocean, as suggested by *Gordon* [1986]. In this section, the three-dimensional nature of the model circulation is explored further.

Figures 2*a* and 2*b* indicate the presence of a well-defined deep undercurrent in the North Atlantic which descends along the continental slope from 2000 m to 3000 m between 25°N and 18°S. Figure 2*c* shows the north flowing bottom water at 30°S in the Pacific. These flows are 10 Sv, 14 Sv, and 9 Sv in magnitude, respectively. It is somewhat surprising to find in Figure 2*d* that a large amount of water is coming up at the equator in the Pacific. The vertical velocity averaged across the Pacific in a belt 2° latitude wide gives about 8 Sv of upward transport. In a separate calculation, McCann et al. (1992) show a transport through the Indonesian passage of 10 Sv in the upper 710 m of the water column. Thus a connection of the global thermohaline circulation via strong upwelling is possible in the equatorial Pacific.

To reinforce this concept and better delineate some earlier flow patterns in the depth ranges 0–135 m and 135–1000 m, Figure 3 shows flow passing from the Pacific to the Indian Ocean at 3°S, with a maximum southward speed of 45 cm s^{-1} at 160-m depth along the west side of the Indonesian passage (Figure 3*a*), flow crossing the Indian Ocean with a broad subsurface core (Figure 3*b*), some flow passing into the South Atlantic around Cape Agulhas from the Indian Ocean (Figure 3*c*), and another broad subsurface current crossing the South Atlantic (Figure 3*d*). The upper depth ranges of Figure 2*a* and 2*b* show the thermohaline flow then proceeding northward into the North Atlantic in general proximity to the western boundary. Plates 3 and 5 already revealed the overall consistent horizontal path of this upper

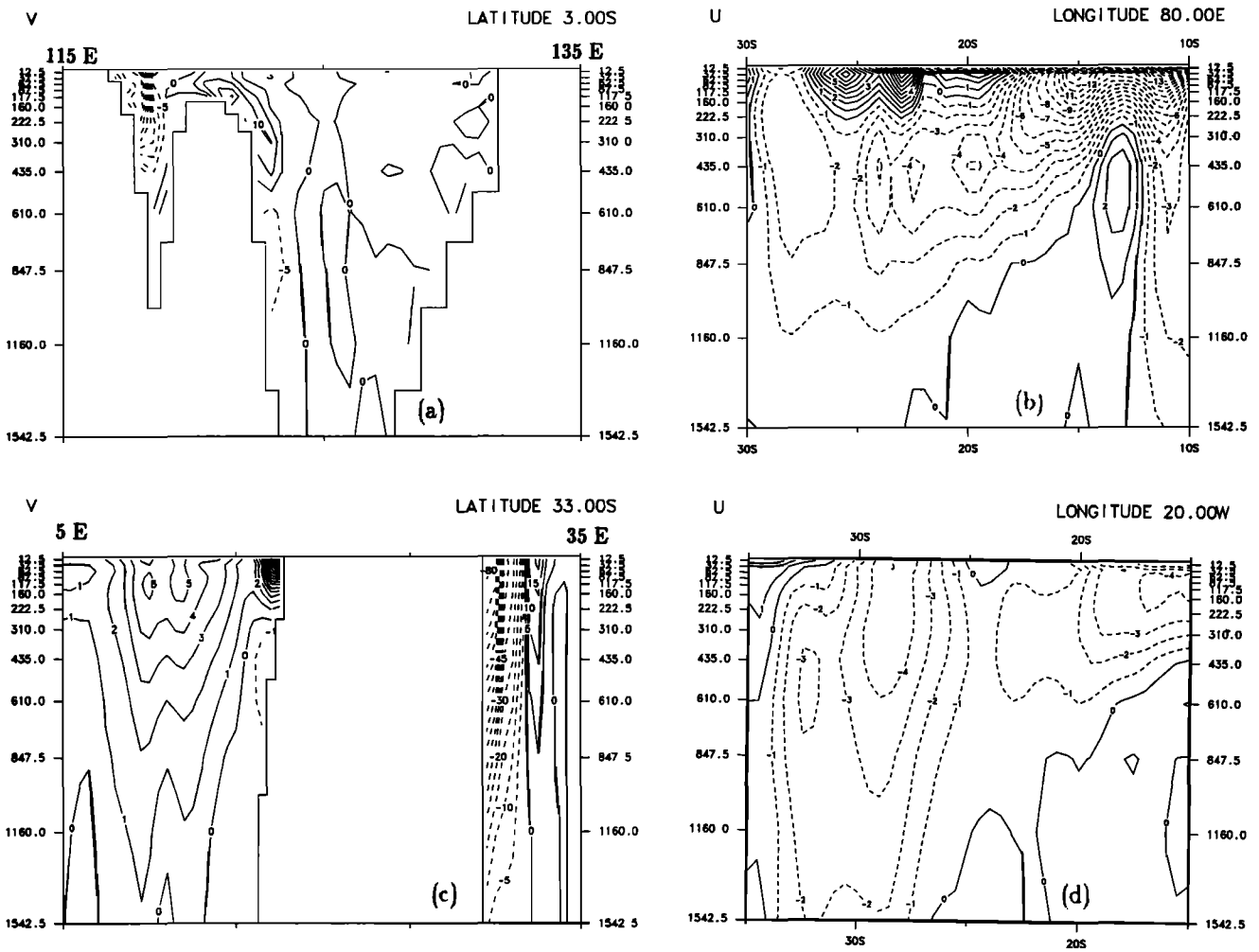

Fig. 3. Mean normal velocities (in centimeters per second, with varying contour intervals) for cross sections (*a*) at 3°S in the Indonesian passage, with Celebes shoaled to 160 m; (*b*) in the South Indian Ocean at 80°E; (*c*) at 33°S on either side of Africa (with different contour intervals); and (*d*) in the South Atlantic at 20°W.

ocean circulation. It thus appears that a global conveyor belt circulation of the order of 10 Sv exists, with strong equatorial upwelling toward the surface providing the connection between abyssal and thermocline flows in the Pacific.

Figure 4 shows the meridional stream function for the Equatorial Pacific. Although this representation suppresses exchanges in the longitudinal direction, such as flow from the Pacific into the Indian Ocean, it better quantifies the vertical circulations. The zero line separates 3–4 Sv of water which rises across a depth of about 700 m from north of the equator and 5–6 Sv which rises from the south. In the upper few hundred meters (top panel), a pair of strong wind-driven cells augment the thermohaline upwelling and would tend to stir the upper water column into which the upwelling occurs.

An upwelling of nearly 10 Sv below the equatorial thermocline is not widely anticipated on the basis of conventional oceanographic theory. To give assurance that such a circulation is not inconsistent with existing observations, Figure 5 compares the long-term prognostic temperature and salinity fields of the model with the high-resolution local observations from the Hawaii-Tahiti Shuttle Experiment in the 150°–160°W region [from *Wyrtki and Kilonsky*, 1984] and also with the lower-resolution global data set of *Levitus* [1982]. A number of observed features from the shuttle experiment are reproduced in the model. These include the tilt of isotherms in the latitude band 5°–8°N, the fanning out of isotherms near the equator, the salinity front at the equator, and salinity subsurface maxima and intermediate depth minima on either side of the equator. The prognostic fields conform better to the high-resolution data than do the low-resolution fields, suggesting that the model's equatorial flow patterns may be quite realistic.

Figure 6 gives added confidence in the model simulation. In Figures 6*a* and 6*b*, most of the observed geostrophic structure of zonal jets in the upper ocean is reproduced in the predicted fields. For the deep ocean, Figures 6*c* and 6*d* indicate that the absolute velocity measurements of *Firing* [1989] are also reasonably well simulated by the model. There is good agreement in regard to the eastward jet at 3-km depth a few degrees south of the equator, a westward jet at 4 km somewhat further south, and eastward jets above 1 km on either side of the equator. However, the vertical resolution of the model is insufficient for showing the details of the structure observed near the equator in the depth range 1–2 km.

The observed deep zonal jets have been suggested to be

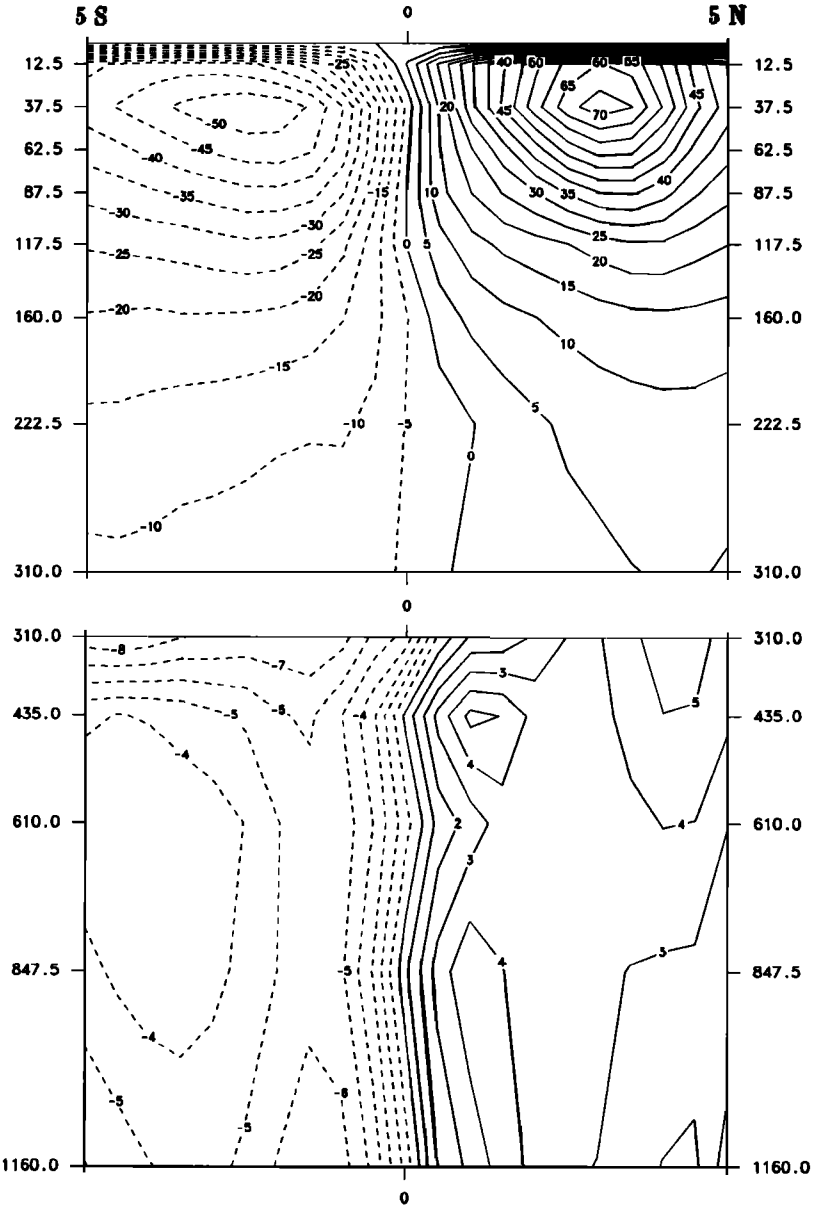

Fig. 4. Time-averaged meridional stream function of volume transport with 5° of the equator in the Pacific, for (top) surface to 310 m and (bottom) 310–1160 m. The contour intervals are 5 Sv and 1 Sv in the upper and lower panels, respectively.

part of the deep thermohaline circulation [*Firing*, 1989]. According to theoretical considerations [*Kawase*, 1987], they can occur in association with enhanced equatorial upwelling or mixing, as an alternative to the more commonly accepted possibility of near-uniform upwelling, which was developed by *Stommel and Arons* [1960]. In the present study, a parameterization of vertical mixing is used with a dependence on Richardson number [*Pacanowski and Philander*, 1981]. This parameterization may give rise to enough physically based vertical mixing for equatorial upwelling to be favored over more uniform upwelling.

Since the numerical model gives a three-dimensional view of time-averaged motion, it is possible to determine how the zonal jets and the upwelling fit together in a continuous way. Figure 7 shows vertical cuts of the deep zonal velocity every 20° longitude in the equatorial Pacific as well as flow patterns in the depth ranges 1000–3300 and 3300–5200 m. Schematic single and double arrows indicate a relatively consistent pattern of horizontal circulation in zonal jets that connect by turning and upwelling near topography. Figure 8 confirms the appropriate vertical motion across the interface between the two depth ranges, and it shows zonal sections of zonal velocity at 2°N and 2°S and at the equator. Schematic arrows indicate a series of rising jets near the equator traveling both east and west. These include the Equatorial Undercurrent in the upper few hundred meters and Tsuchiya Jets in the depth range 400–1200 m. The flow evidently undergoes a series of directional reversals as it rises from the ocean floor to the sea surface. These "thermohaline switchbacks" constitute the upward connection between the deep circulation coming from the South Pacific and the warm water route returning through the Indonesian archipelago.

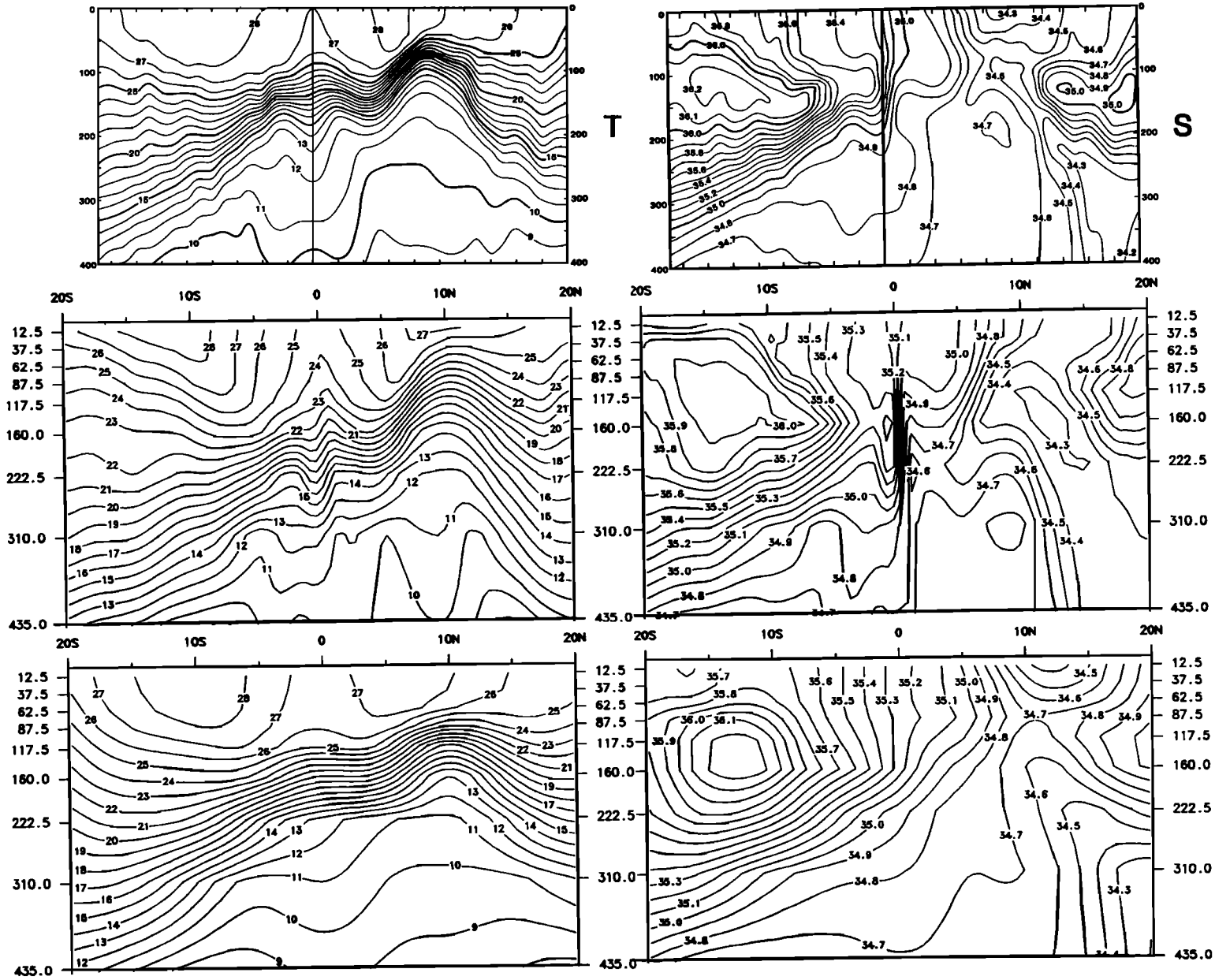

Fig. 5. (Left) Temperature and (right) salinity normal to the equator at a longitude of about 160°W. (Top) One-year averages from the Hawaii-Tahiti Shuttle Experiment [*Wyrtki and Kilonsky*, 1984]. (Middle) Averages from years 6–10 of the seasonal model run. (Bottom) Smoothed, gridded observations of *Levitus* [1982].

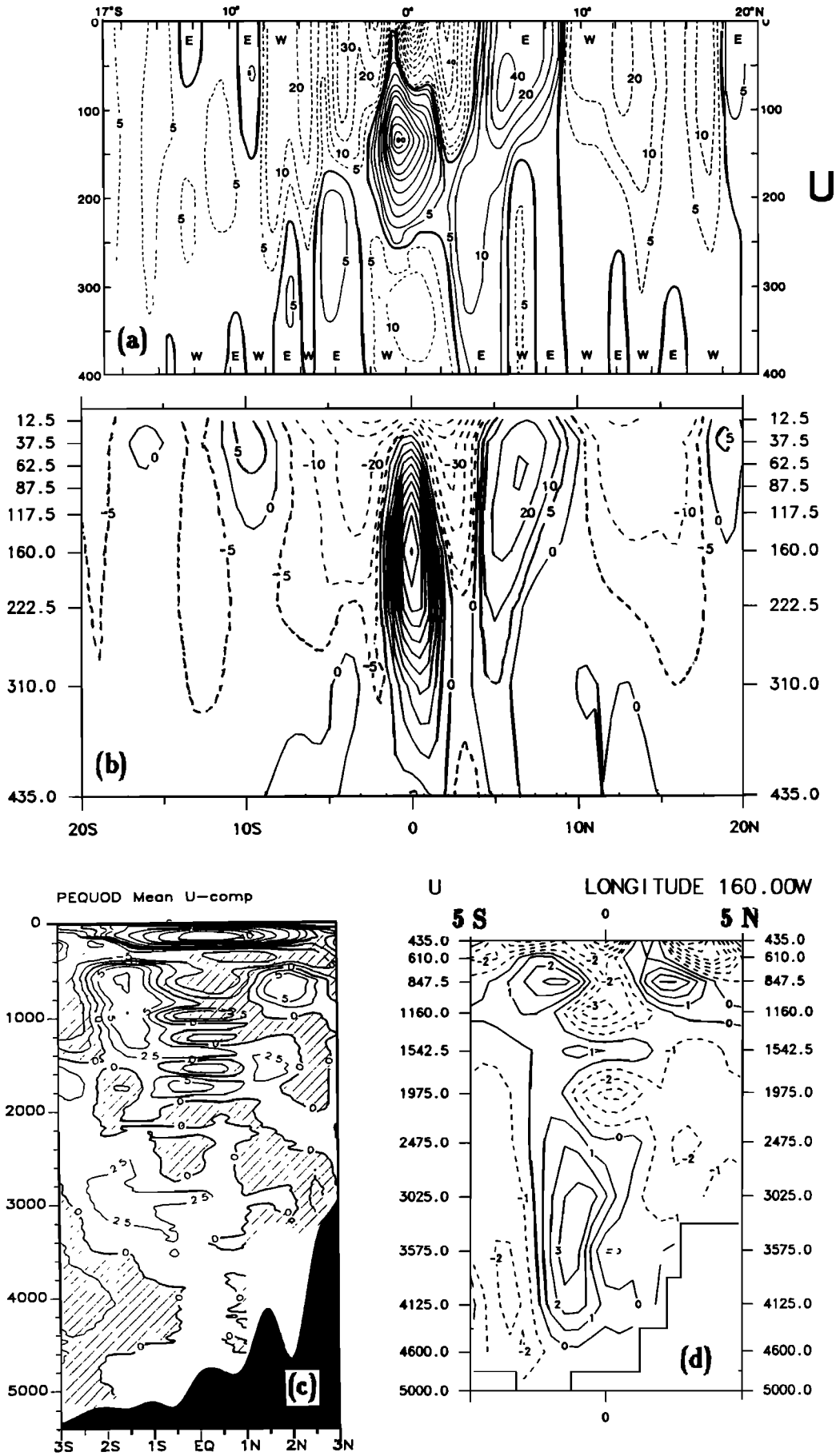

Fig. 6. Time-averaged near-surface and deep zonal mean velocities at about 160°W, (*a*) for an annual mean from the Hawaii-Tahiti Shuttle, (*b*) for seasonal years 6–10 of the model, (*c*) from 16-month, direct current measurements of *Firing* [1989], and (*d*) for years 6–10 of the model.

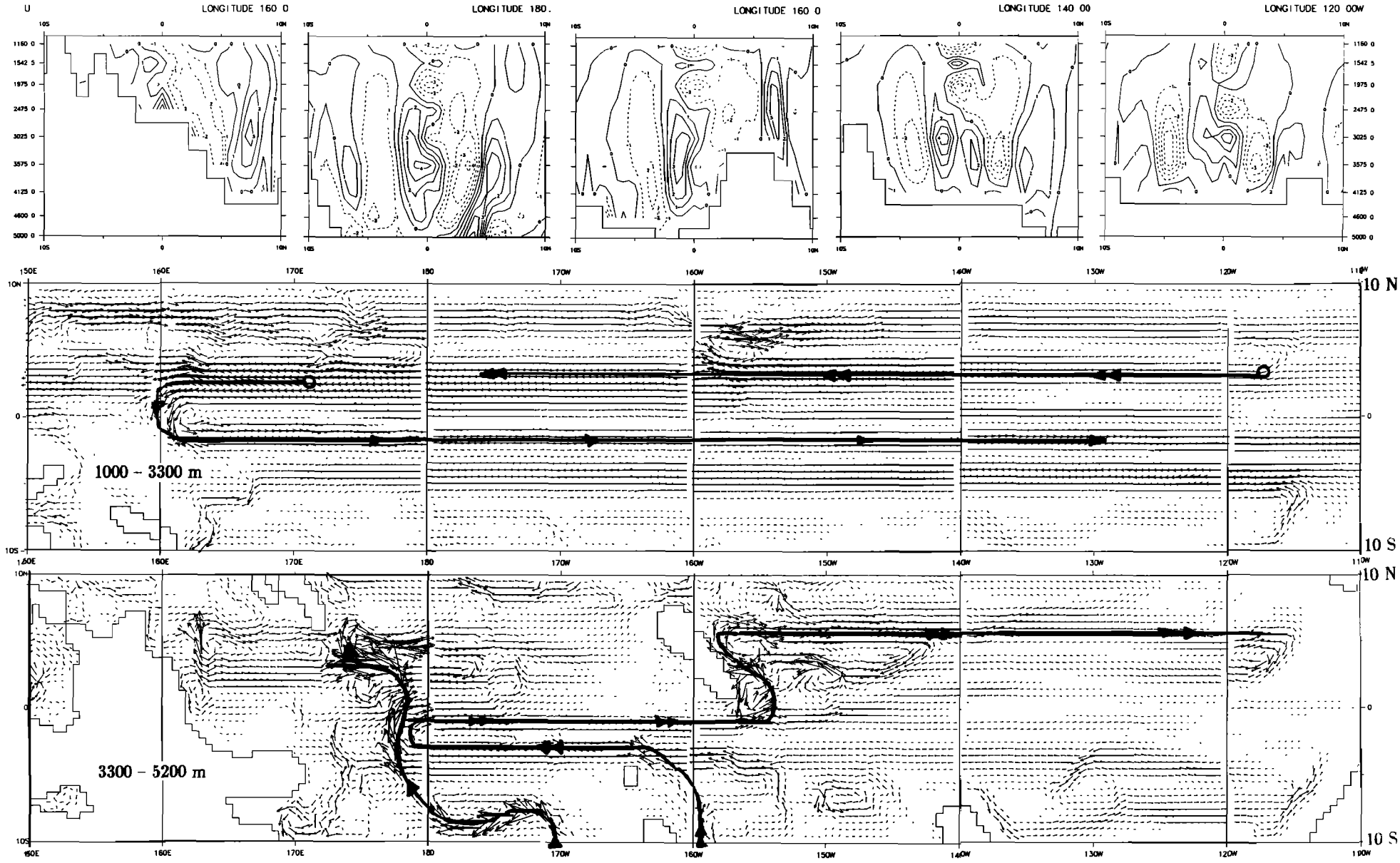

Fig. 7. Meridional cross sections of deep zonal velocity and vector maps of deep and abyssal flow in the band 10 S to 10 N of the Pacific.

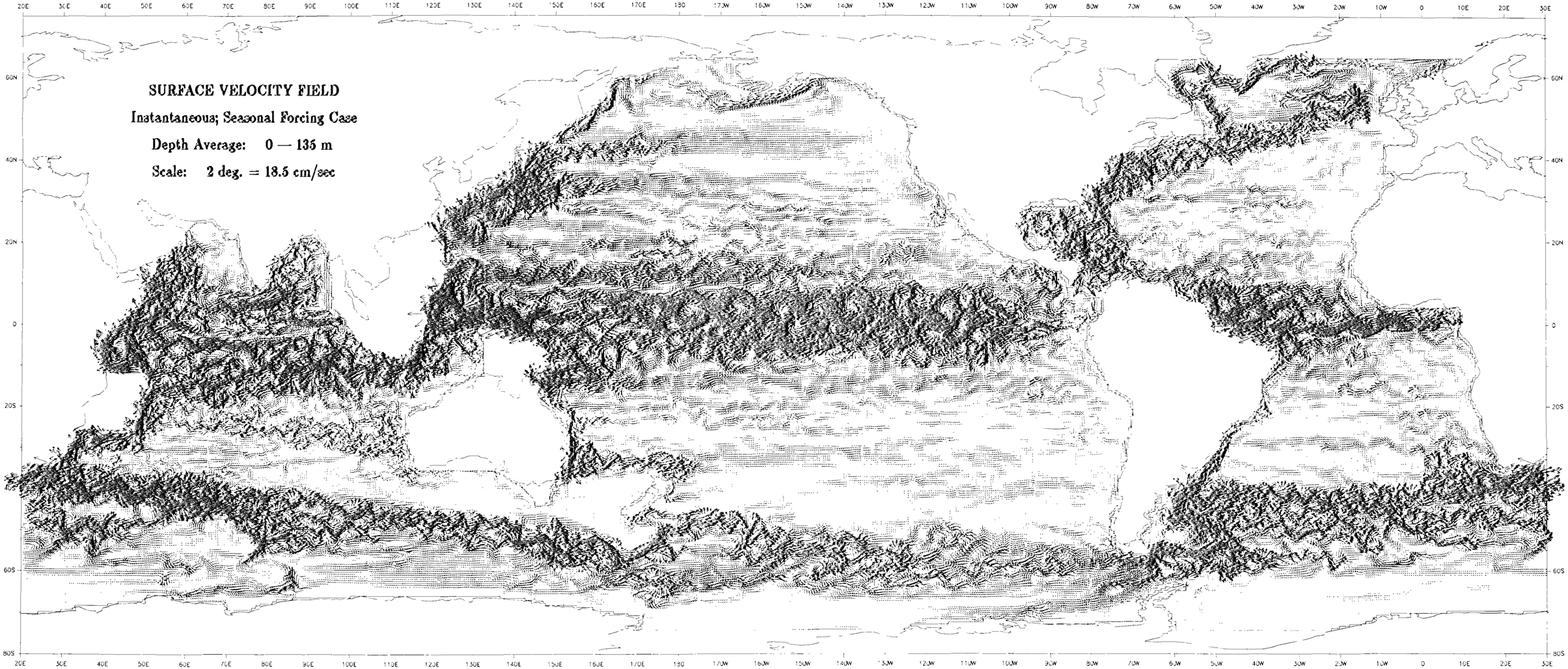

Plate 2. Instantaneous (October) near-surface velocity field for biharmonic friction and seasonal forcing.

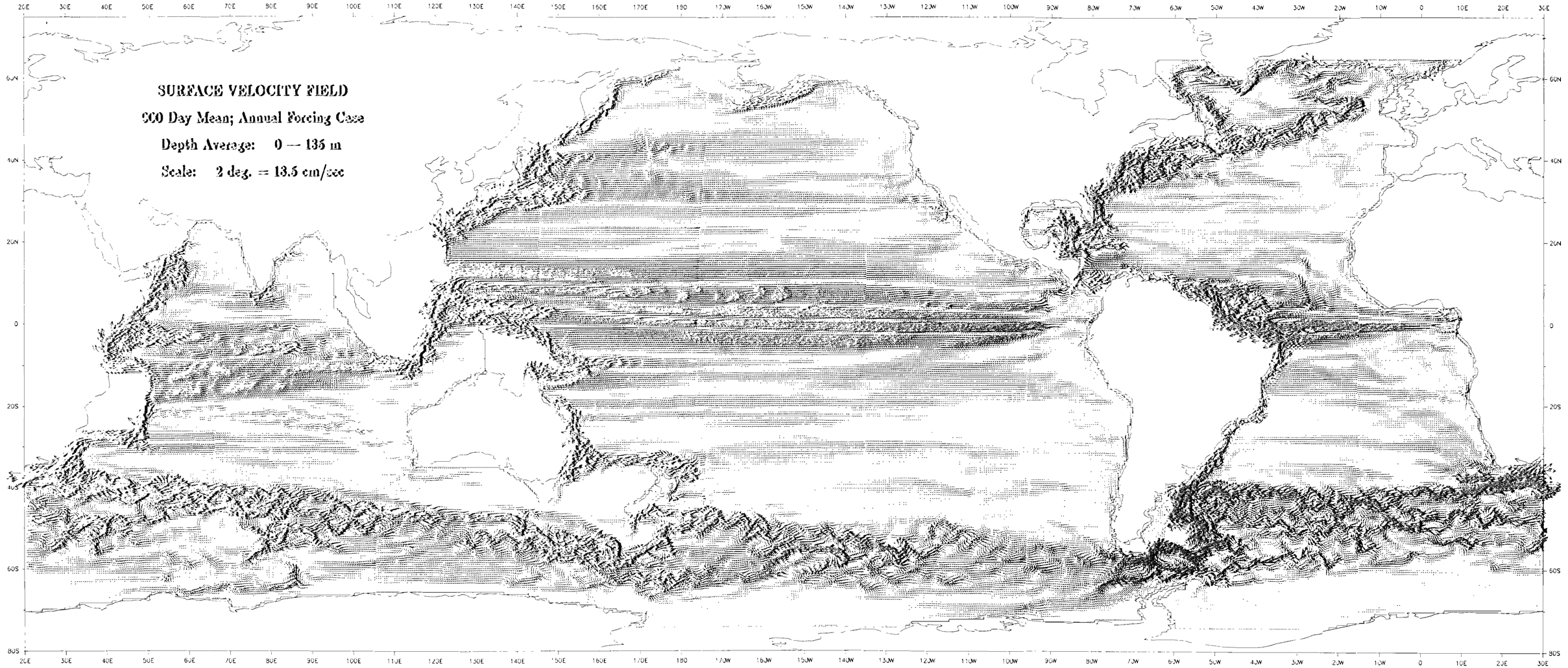

Plate 1. Time averaged near-surface velocity field for biharmonic friction and annual mean forcing. In all vector plots such as this, arrows that would exceed 4° latitude longitude in length are truncated to that size.

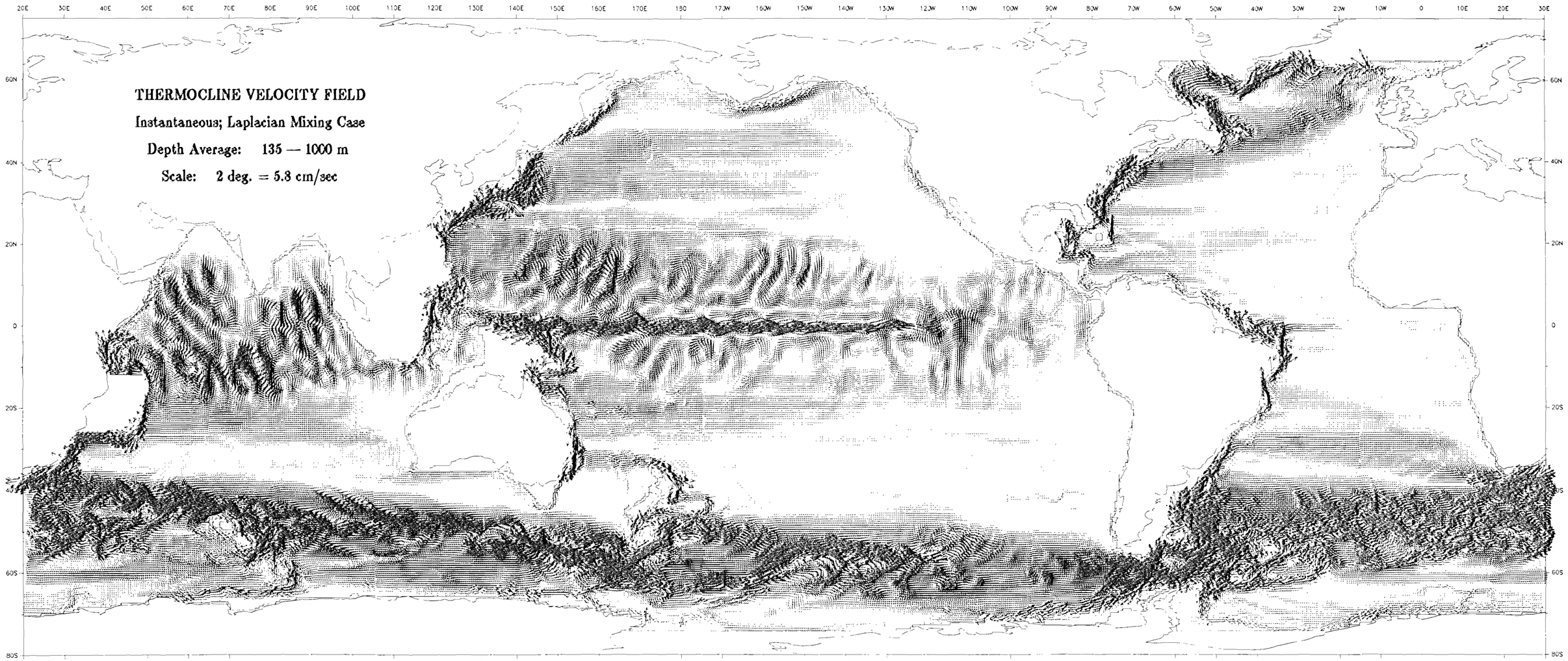

Plate 4. Instantaneous thermocline velocity field for Laplacian friction and annual mean forcing.

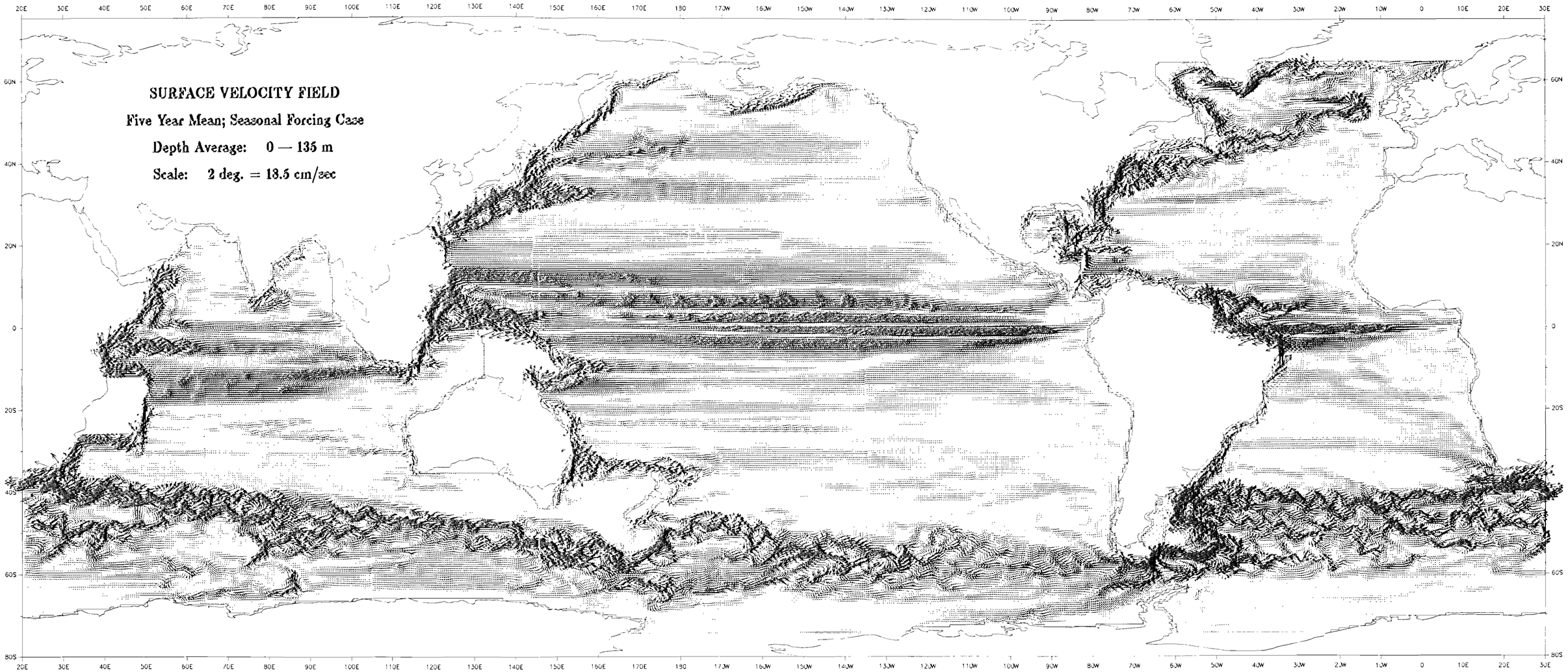

Plate 3. Time-averaged near-surface velocity field for biharmonic friction and seasonal forcing.

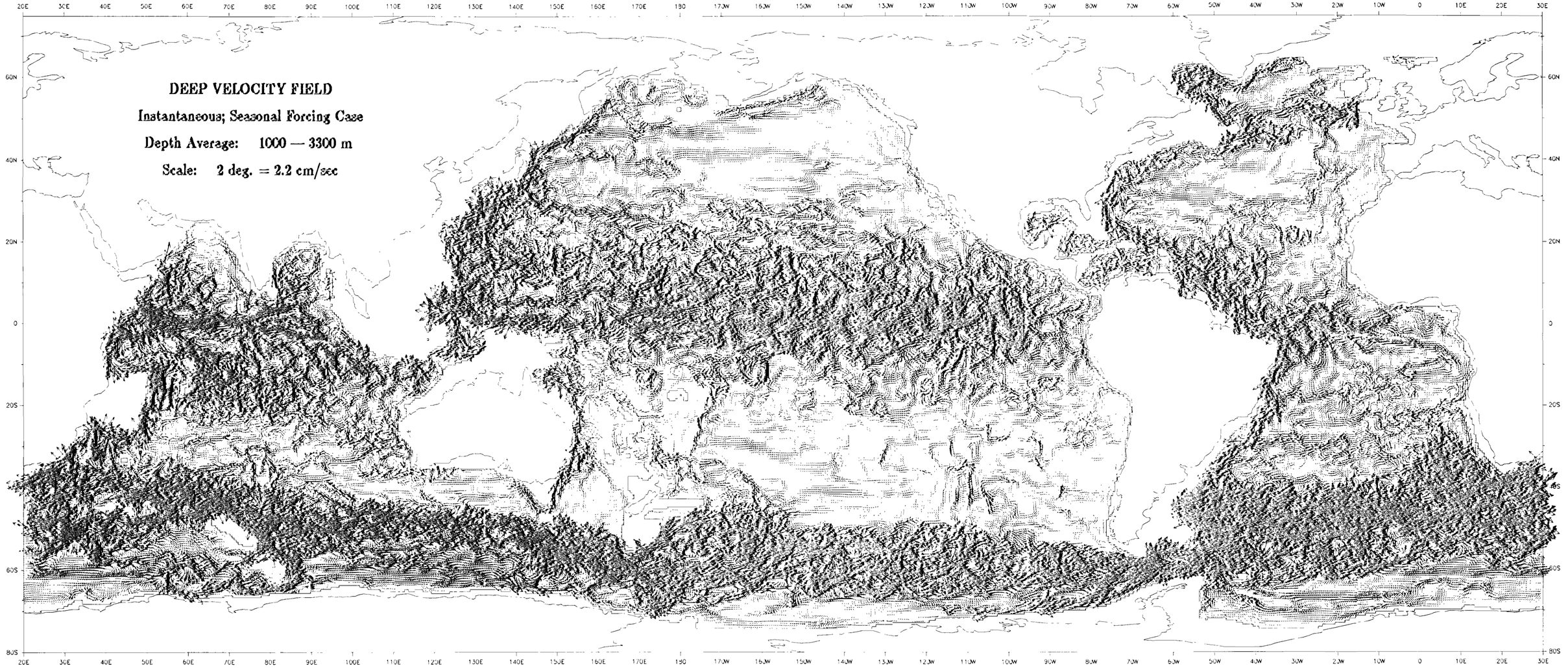

Plate 6. Instantaneous (October) deep-ocean velocity field for biharmonic friction and seasonal forcing.

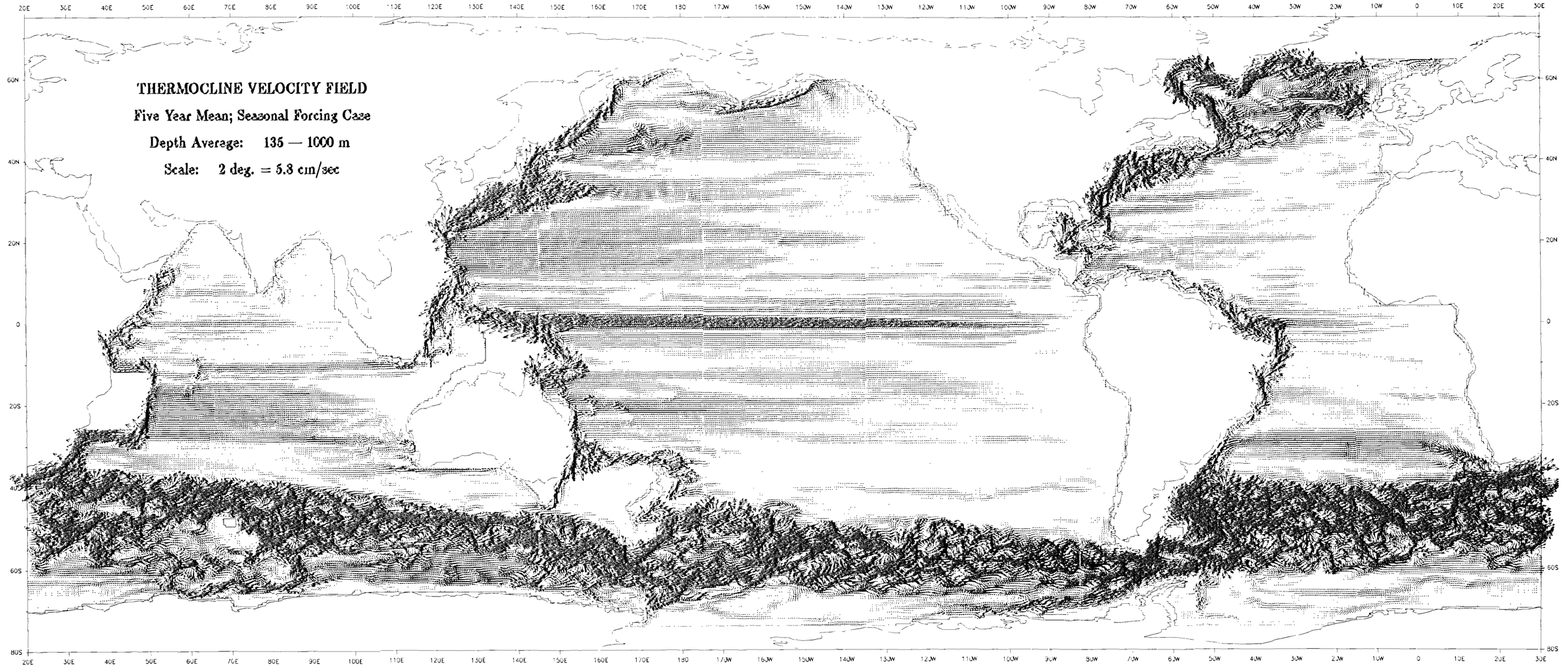

Plate 5. Time-averaged thermocline velocity field for biharmonic friction and seasonal forcing.

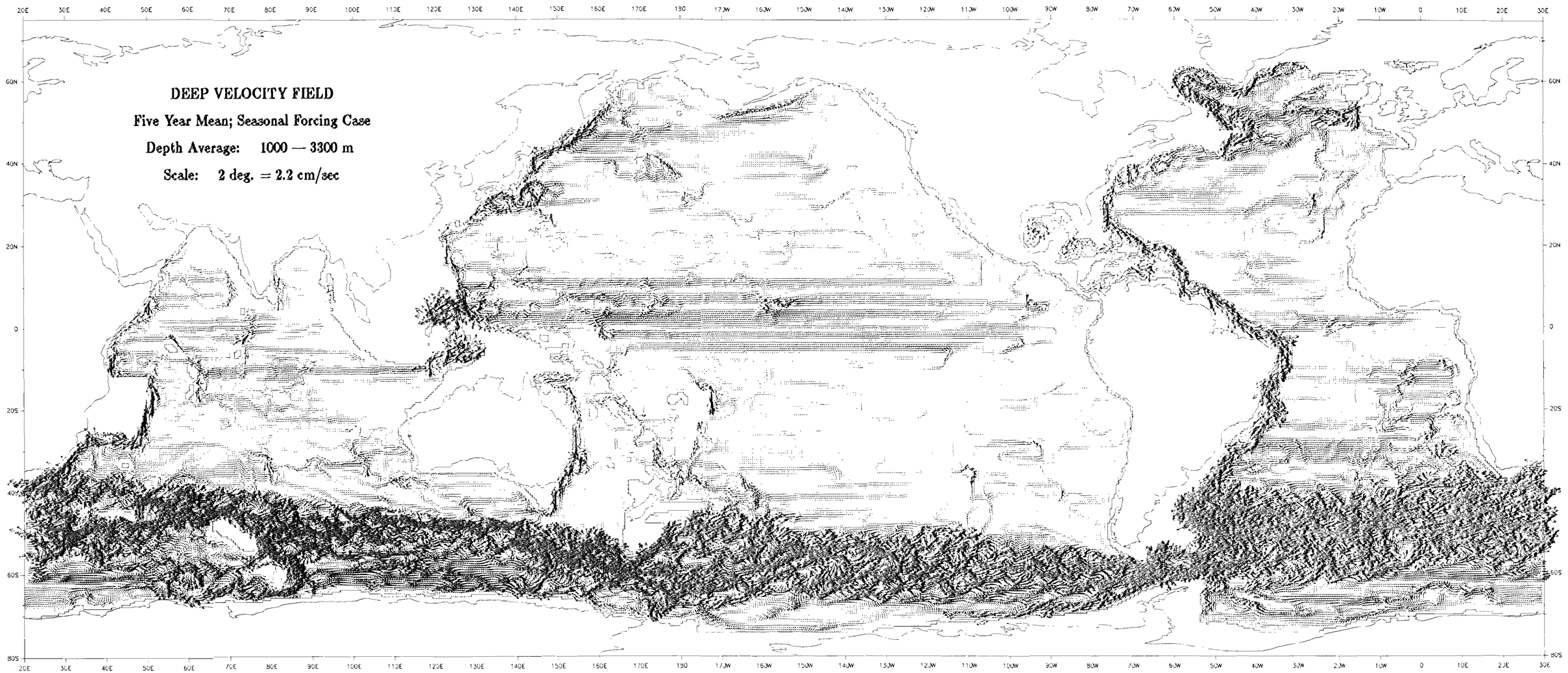

Plate 8. Time-averaged deep velocity field for biharmonic friction and seasonal forcing.

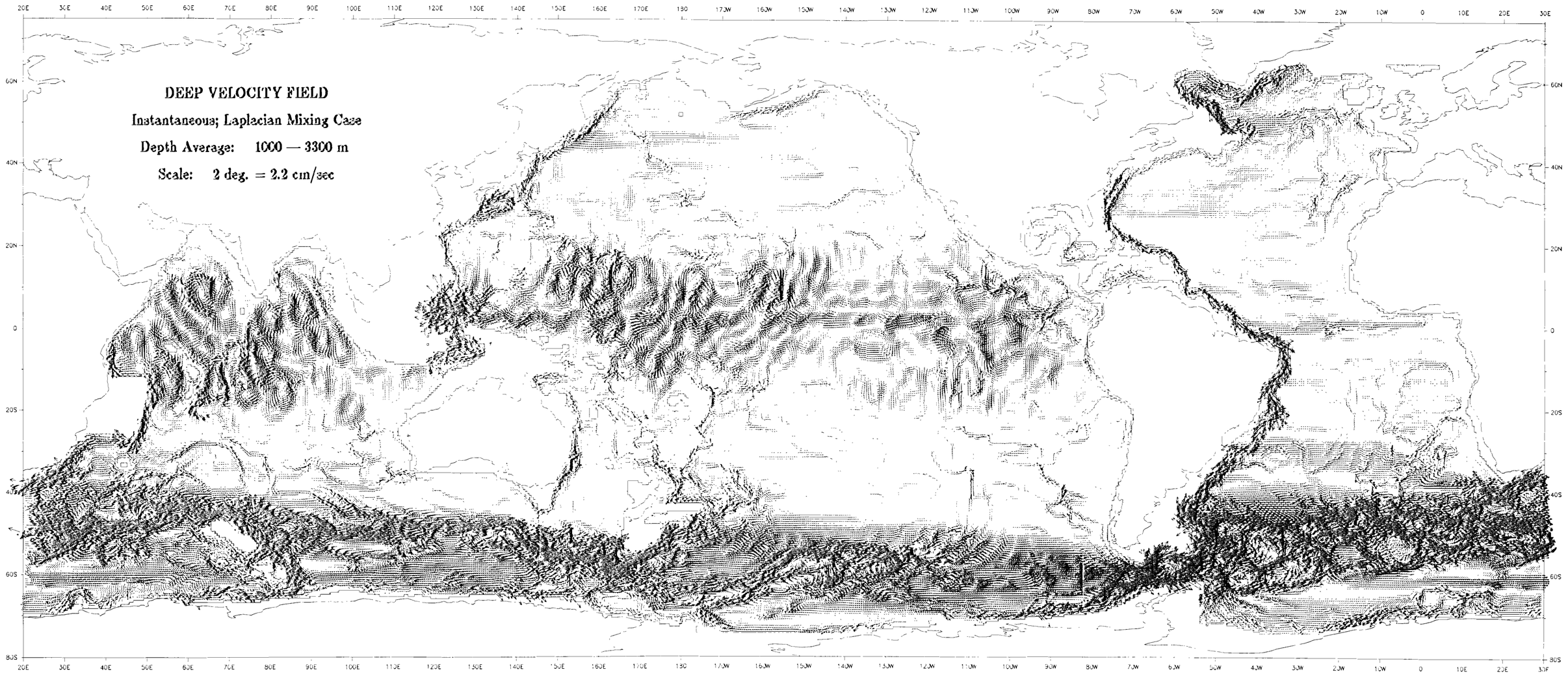

Plate 7. Instantaneous deep velocity field for Laplacian friction and annual mean forcing.

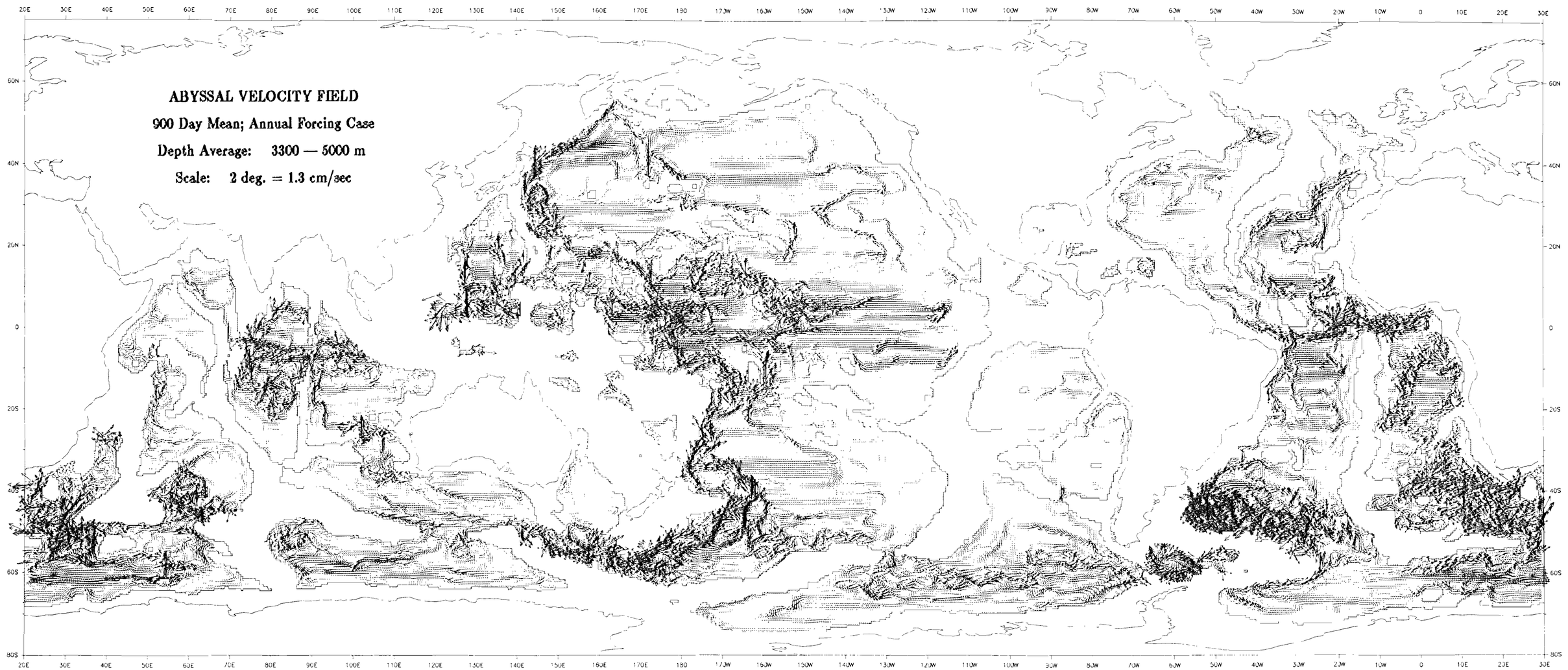

Plate 10. Time-averaged abyssal velocity field for biharmonic friction and annual mean forcing.

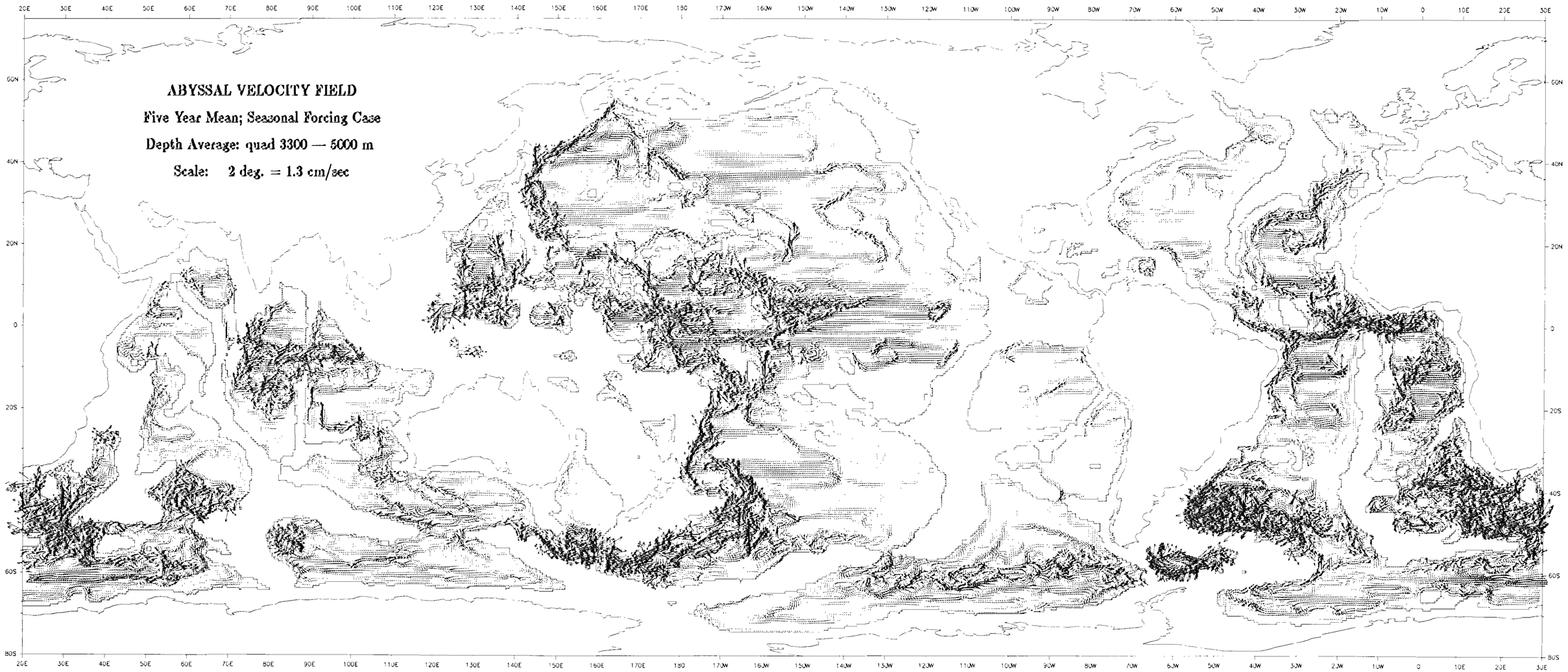

Plate 9. Time-averaged abyssal velocity field for biharmonic friction and seasonal forcing.

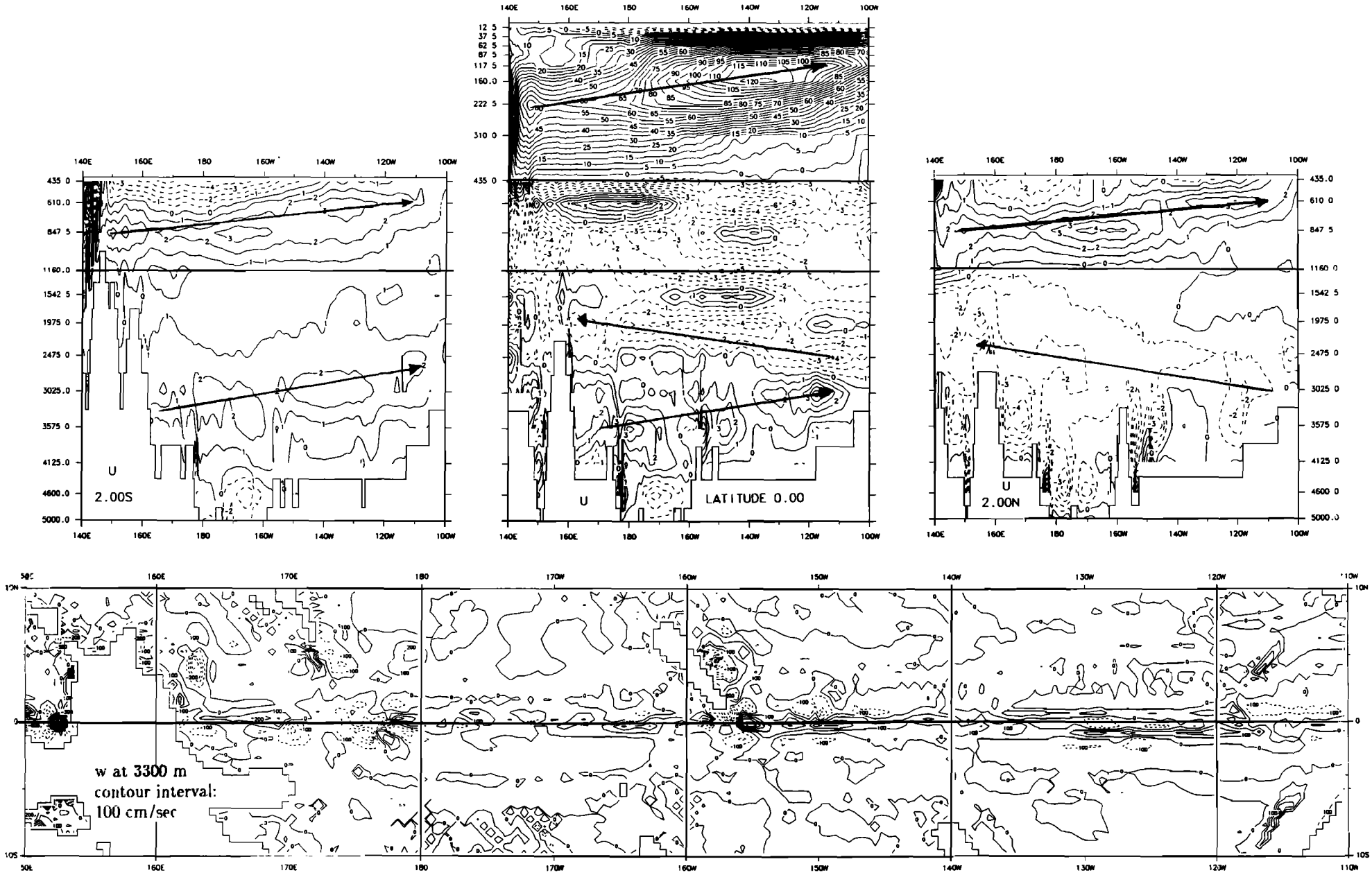

Fig. 8. Zonal sections of zonal velocity at 2°S, 0°, and 2°N in the Pacific, plus mean vertical velocity at 3300 m in the band 10°S to 10°N.

It is fairly clear from the model result in Figures 6–8 that the vertical resolution very near the equator is somewhat marginal. The vertical structure observed in the depth range 1–2 km (Figure 6*c*) is poorly resolved by the present model grid. However, it appears that the model is trying to resolve physical phenomena rather than merely being susceptible to computational noise. The present simulation does appear to be safely beyond a threshold for vertical resolution suggested by the study of *Weaver and Sarachik* [1990]. In future simulations it will be important to increase vertical resolution as well as horizontal resolution, in order to examine the sensitivity of structures like the thermohaline switchbacks to numerical truncation errors.

We now examine the thermohaline circulation in a way which is often used to display the results of coarse-grid simulations, i.e., the meridional stream functions. Figure 9*a* depicts NADW circulation in the Atlantic, with intensity of the same magnitudes at 25°N and 18°S as was already obtained from direct calculations in western boundary undercurrent cores. Thus the Atlantic circulation is not strictly a broad overturning as the figure might suggest, but a boundary current phenomenon in certain latitude ranges, as indicated by this high-resolution simulation.

The preceding remark is not meant to exclude the possibility of interior flows; in fact, they appear in animations of deep particle trajectories, especially north of 25°N. However, it appears that broad flows in the deep and abyssal waters are often accompanied by important boundary circulations of equal or greater magnitude. This is in qualitative agreement with the theory of *Stommel and Arons* [1960], although the present study typically shows equatorward rather than poleward interior flow in both the North Atlantic and the North Pacific.

Figure 9*b* shows the Indo-Pacific stream function with its intense equatorial upwelling. The strength of upwelling so confined on the equator could not be adequately reproduced in a coarse-grid model. However, the coarse-resolution simulation of *Maier-Reimer and Hasselmann* [1987] does suggest the possibility of such an equatorial connection.

As we have seen, the equatorial upwelling is intimately related to observables of a horizontal nature which are also of small scale, namely, the deep equatorial jets. Thus the high-resolution simulation has the possibility of being validated by standard oceanographic measurements in the deep Pacific. Not only can the tilting axes of the deep jets be measured, but also a predicted connection to the core circulation of the conveyor belt may be detectable in observations of transient tracers.

Net throughflow is also a verifiable quantity. In the Indian Ocean, recent measurements of the throughflow from the Pacific have been made by hydrographic sections between Bali and Australia. The total observed transport of approximately 17–18 Sv through Indonesia (J. Swallow, personal communication, 1991) agrees well with the total modeled throughflow of 17 Sv. More information about modeled throughflow and a comparison with observations and theory is given by J. S. Godfrey et al. (Why does the Indonesian throughflow appear to originate from the North Pacific, submitted to *Journal of Physical Oceanography*, 1992). Additional evidence that the modeled throughflow is relatively correct, based on interpreting salinity as a tracer, can be found in Figure 36 of the present paper.

Note in Figure 9*b* that some upward flow at the equator moves back toward 30°S in the depth range 1000–3300 m. In the flow patterns of Plate 8 the western boundary undercurrents of the Indian and Pacific oceans may be carrying a significant fraction of the approximately 8 Sv of southward flow. However in video animations there is also a general southward drift in the interior toward the ACC. That flow appears to acquire an eastward velocity as it approaches the ACC and is entrained into it. This would appear to be simple conservation of absolute angular momentum by the interior flow. After joining the ACC, the flow must pass through the Drake Passage before returning via upwelling into the conveyor belt system of the South Atlantic. Figure 9*c* depicts the global transport stream function, which indeed shows intensified upwelling of nearly 6 Sv in the latitude range of the Drake Passage. Thus some fraction of the thermohaline circulation follows a "cold water" route, as has recently been indicated by *Rintoul* [1991].

The results of the present simulation suggest that of the 14 Sv of NADW which flows south at 5°S in the Atlantic, 6 Sv or more comes back through an Indonesian warm water route and up to 6 Sv returns along a cold route also via the deep Equatorial Pacific, but returning back to high southern latitudes and going through the Drake Passage. An additional small amount (1–2 Sv) could very well pass south of Tasmania and along the southern coast of Australia, as is suggested by the flow in the thermocline and deep layers of Plates 5 and 6. The possibility of such a flow is consistent with a recent inverse calculation for the Indian Ocean by *Metzl et al.* [1990], as well as with temperature animations from the global model.

An important remark about the simulated thermohaline circulation is that no appreciable part of it appears to flow north into the deep Indian Ocean. This may be a result of the fact that very little circulation of Antarctic Bottom Water is predicted near Antarctica, as is indicated by the global stream function of Figure 9*c*. It is possible that under more favorable conditions for density forcing in the southern hemisphere, such a circulation would develop and in particular would ventilate the Indian Ocean more effectively, as well as the deep Atlantic and Pacific oceans. The possibility of such AABW circulation could be explored in further experiments that go beyond the scope of this paper.

Another issue concerns the extent of bottom water penetration into the mid-latitude North Pacific by the conveyor belt. In the Indo-Pacific stream function, such inflow appears negligible; however, the abyssal maps of Plates 9 and 10 show clear penetration of a deep western boundary undercurrent far into the North Pacific. It is likely that this flow is compensated by the southward moving deep flow on the eastern side of the North Pacific or by broad interior flow, so that cancellation occurs in the volume transport stream function. It is therefore possible that some of the 3–4 Sv that rises from the north on the equator, as shown in Figure 4, is from the conveyor belt via the deep North Pacific. This issue, as well as others concerning deep circulation, could be sorted out by using the already simulated velocity fields for predicting tracer distributions in the deep ocean.

It should be noted that much of the path of the conveyor belt is favorably aligned with prevailing winds, both near the surface in the tropics and subtropics and at depth in the Antarctic Circumpolar Current. Much of the remaining flow is in western boundary currents. It may well be the case that the thermohaline circulation is significantly wind driven.

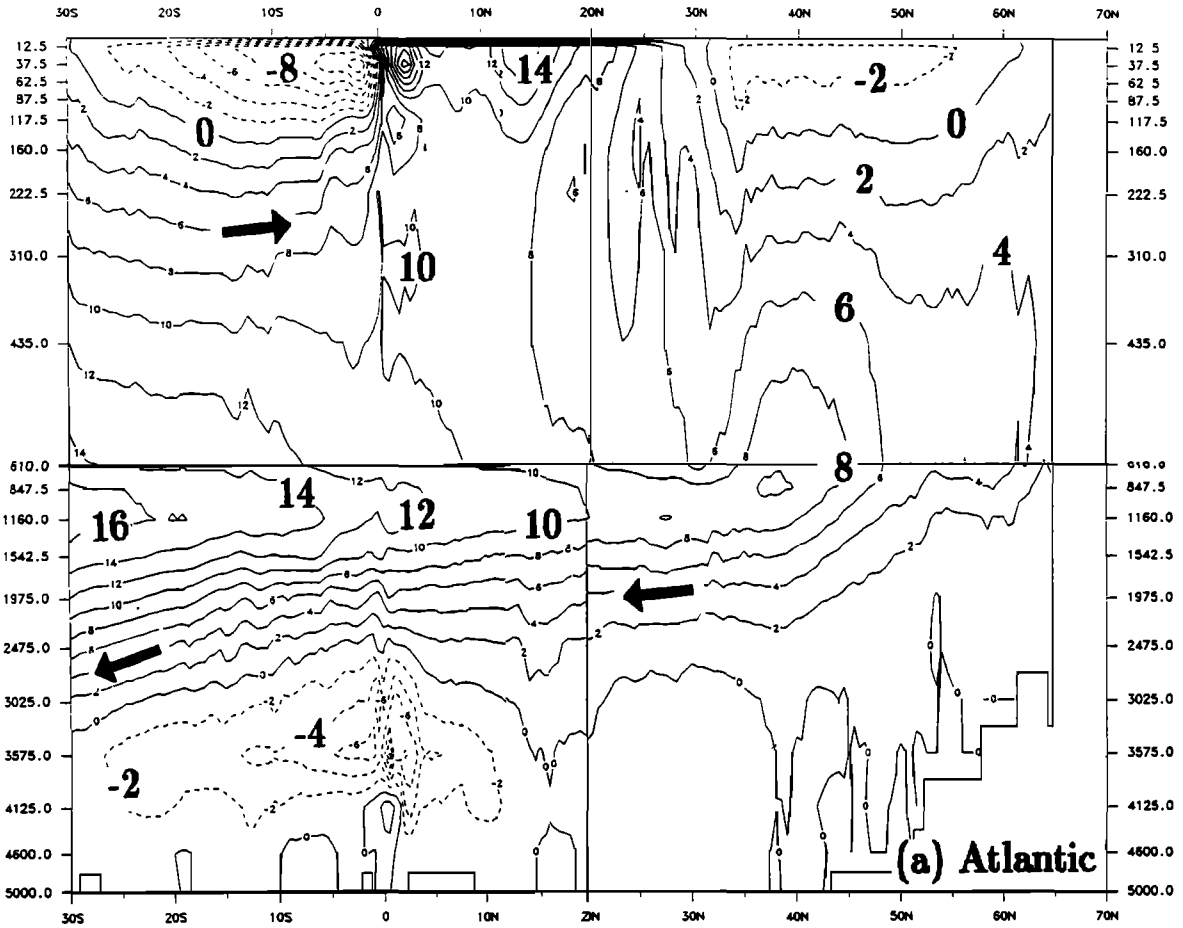

Fig. 9. Meridional stream functions (sverdrups) for (*a*) the Atlantic, (*b*) the Indo-Pacific, and (*c*) the global ocean. Flow is clockwise around local maxima.

This has also been suggested by *Gordon* [1986]. Conversely, the wind-driven aspects of the ACC are augmented by thermohaline effects as well, both from participation in the conveyor belt circulation and from differential heating at the sea surface. Thus the ACC may also be significantly driven by both thermal and wind forcing.

It is clear from the results of this section that a conveyor belt circulation with a relatively high speed core exists in the global ocean. Although the concept of a conveyor belt is a simplification of three-dimensional thermohaline circulation, that concept has merit in explaining a dominant connection between the largest tropical ocean, the Pacific, and the largest polar ocean of the northern hemisphere, the Atlantic joined to the Arctic. However, there are many connections of this idealized circulation to the rest of the world ocean. In particular, water masses form the deep basins of the world ocean undoubtedly cycle in and out of the conveyor belt as it travels along. Furthermore, the interconnectedness with Antarctic Circumpolar Current is extensive, both in the deep water where the two coincide along half the path around Antarctica and at the surface where the two pass close to each other and interact in the Agulhas Extension and Retroflection regions. Thus the total connectedness of the global ocean circulation must still be emphasized.

5. Variability

Variability is an important aspect of ocean general circulation because it is a basic measure of the dynamics of the system. Model fields may provide validating information that can be used to assess how well models perform by comparison with variability fields from the real ocean, such as those obtained with satellite altimeters, intensive hydrographic surveys, or in situ moorings of current meters and thermistors. Some aspects of the simulated variability are briefly examined in this section.

The stream function of volume transport is first examined. However, before looking at its variability, it is useful to examine the long-term mean field. Figure 10 shows the time mean stream function for the case of seasonal forcing. (Since the stream functions are almost identical for cases with annual mean and seasonal forcing, only one will be shown.) Mid-latitude integrated flows obey Sverdrup dynamics [cf. *Godfrey*, 1989], with discontinuities of wind-driven interior transport conspicuous only in the Indian Ocean throughflow, the Tasman Front near 30°S, and the South Atlantic cross-flow at 25°–30°S. It is easy to think of the South Atlantic and South Indian circulations as one gyre which is constricted by the intrusion of the southern tip of Africa. In fact, the −20 and −30 Sv contour lines are not cut off there but connect the South Indian and the South Atlantic. Similarly, one can see a Pacific influence by following the −10-Sv contour line from Indonesia until it ultimately crosses the Atlantic, as well as for compensating flow in the Antarctic Circumpolar Current from the Atlantic back into the Pacific via the Campbell Plateau south of New Zealand.

In low latitudes the North and South Equatorial currents,

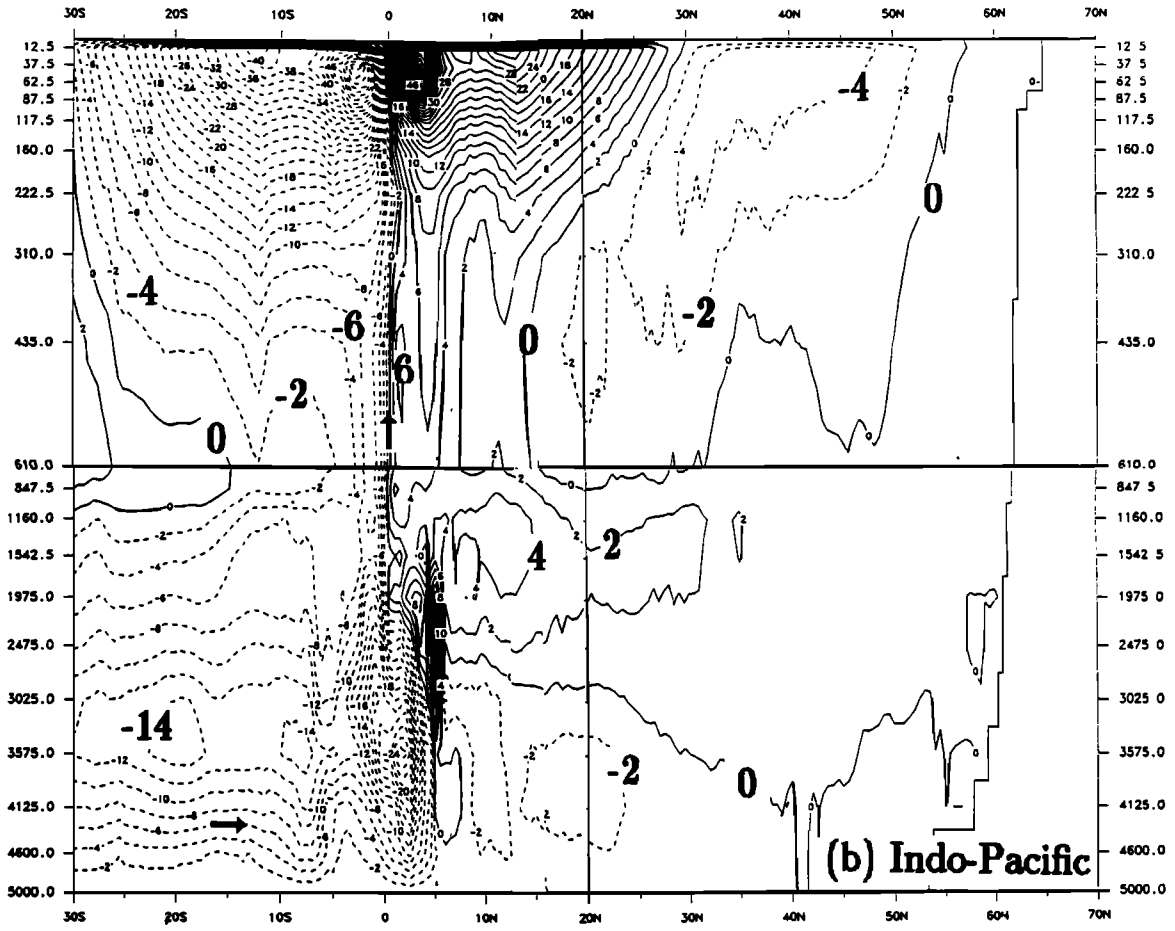

Fig. 9. (continued)

the Equatorial Undercurrent, and the North Equatorial Countercurrent are evident in the central Pacific. Bottom topography is not felt very strongly in middle and low latitudes, although some topographic influences can be seen in the eastern basins of the Atlantic and Pacific. In high latitudes, however, the ACC is strongly affected by topography and seeks to follow constant f/H lines except in the southwest Atlantic. Finally, transport estimates are obtained for all western boundary currents, the time dependence of which will be examined in detail later in this section.

The standard deviation of stream function with annual mean forcing is shown in Figure 11. (A southern hemisphere polar view of this field is given by *Semtner and Chervin* [1990].) Mid-ocean cellularity suggests the influence of bottom topography. Western boundary regions and separated jets are quite active, as are selected parts of the ACC, where interaction with topography or with the mid-latitude Indian and Atlantic gyres occurs. The north subtropical Pacific, equatorial Pacific, and south subtropical Indian Ocean are moderately energetic. By contrast, the southeast Pacific and several smaller regions are "eddy deserts."

Figure 12 indicates that tropical variability is enhanced in all three oceans by seasonal forcing. This enhancement includes the Somali Current, the Pacific North Equatorial Current and Countercurrent, and the North Brazil Current. Seasonal variability of the subarctic gyre in the North Pacific is evident. Variabilities in certain parts of the south Indian and South Pacific oceans are also heightened by seasonal forcing.

Figure 13 shows the standard deviation of yearly averages of transport stream function for years 6–10 with seasonal forcing. The seasonal cycle of transport stream function should be suppressed by this simple technique, and the very high frequencies of the low latitudes should also be filtered out. What remains is a map of the low-frequency intrinsic (mesoscale, not seasonal) variations in mass transport. The map has some similarities to variability maps made from Geosat height fields [*Fu et al.*, 1988], although the variables are quite different. The important areas of variability are the Kuroshio, the Gulf Stream, the Brazil-Malvinas confluence, the Agulhas Extension and Retroflection, and most of the Antarctic Circumpolar Current. Also variability at the southeast corner of New Guinea is simulated, although there is very little evidence that this occurs in nature.

Consider now the field of surface height, which serves as a streamline map for the geostrophic component of surface flow. The surface height in the present rigid-lid model is the equivalent elevation of the sea surface that would give the modeled surface pressure via the hydrostatic relation. Prior to a discussion of variability, examination of the mean field is useful to disclose regions with sharp gradients where heightened activity might be seen in the variability maps. Figure 14 shows the time-averaged flow patterns of upper ocean geostrophic flow with seasonal forcing. (Again, there is little difference between annual mean and seasonal forcing.) Influence of topography is less evident than in the

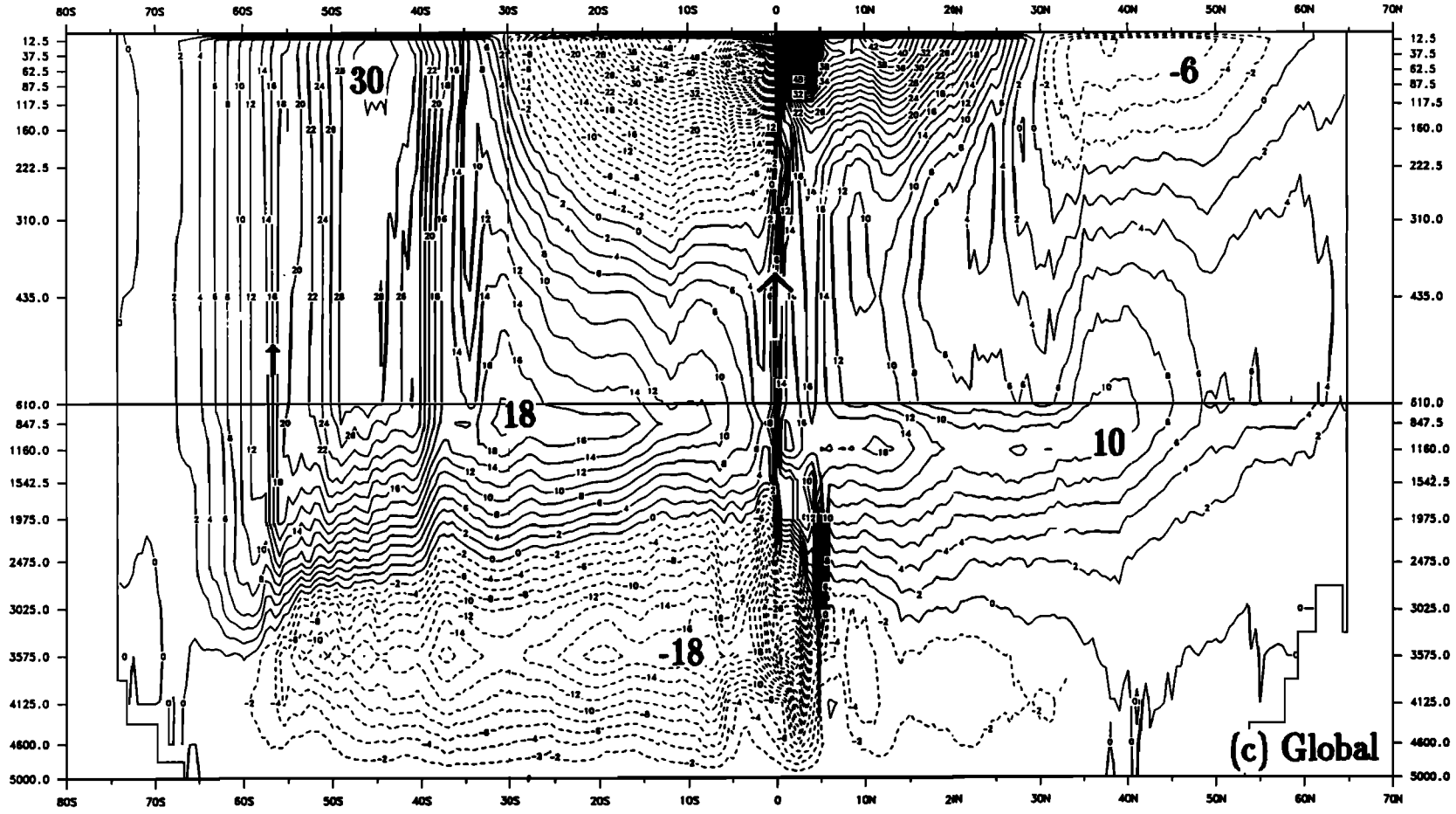

Fig. 9. (continued)

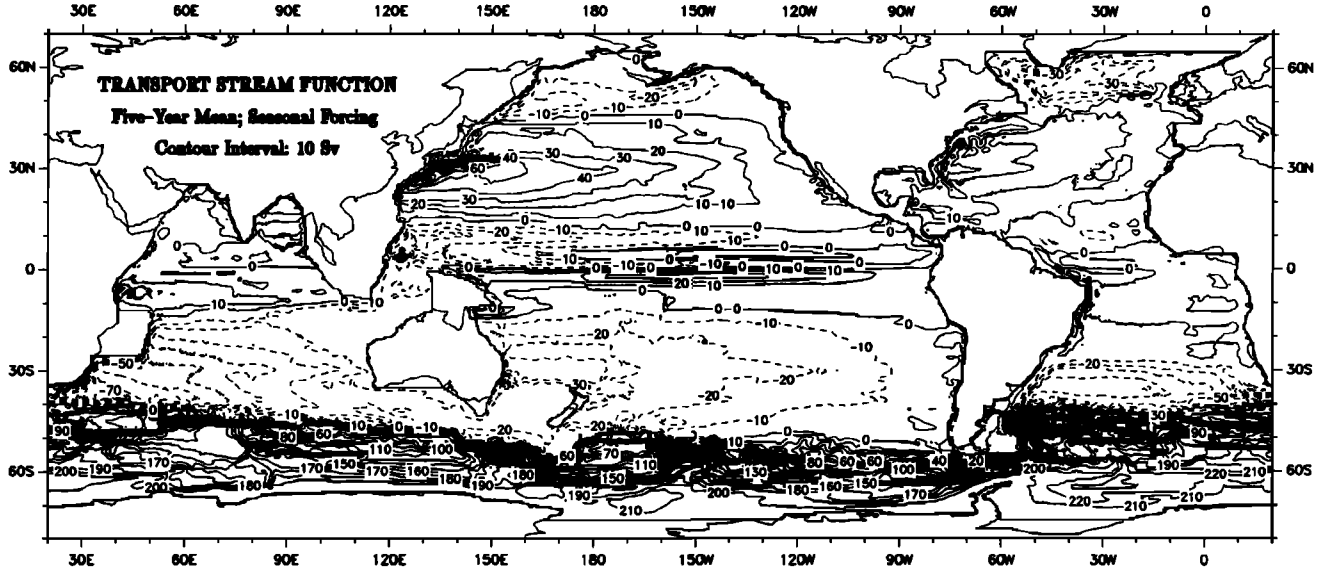

Fig. 10. Time mean stream function for seasonal forcing. Contour interval is 10 Sv.

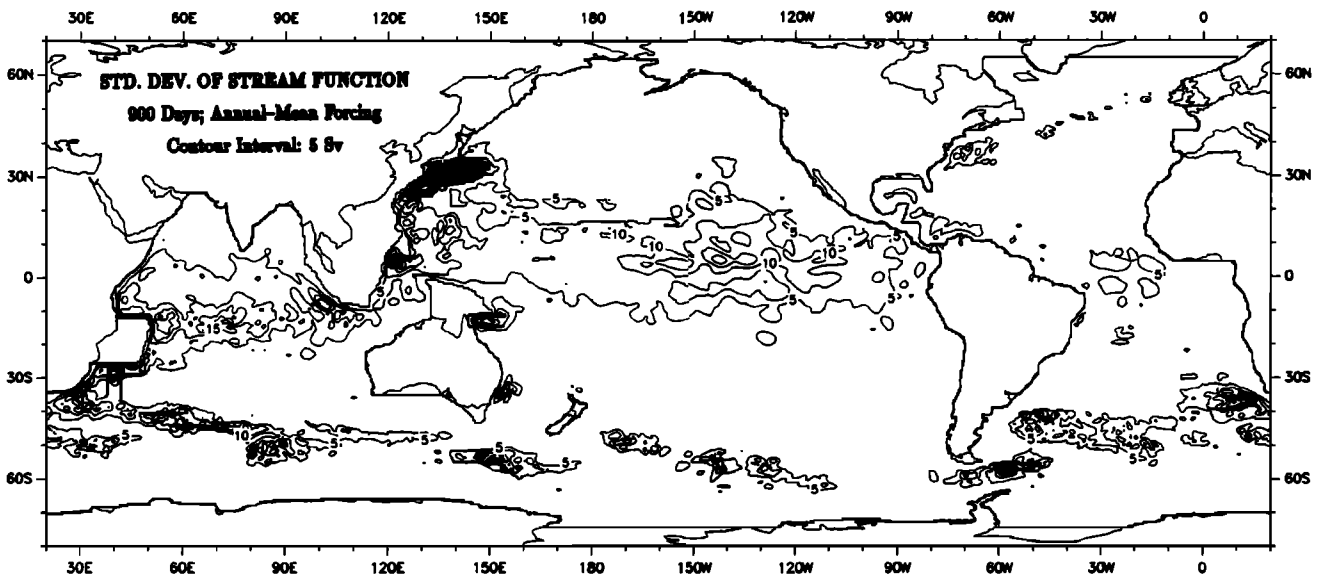

Fig. 11. Standard deviation of stream function for annual mean forcing. Contour interval is 5 Sv.

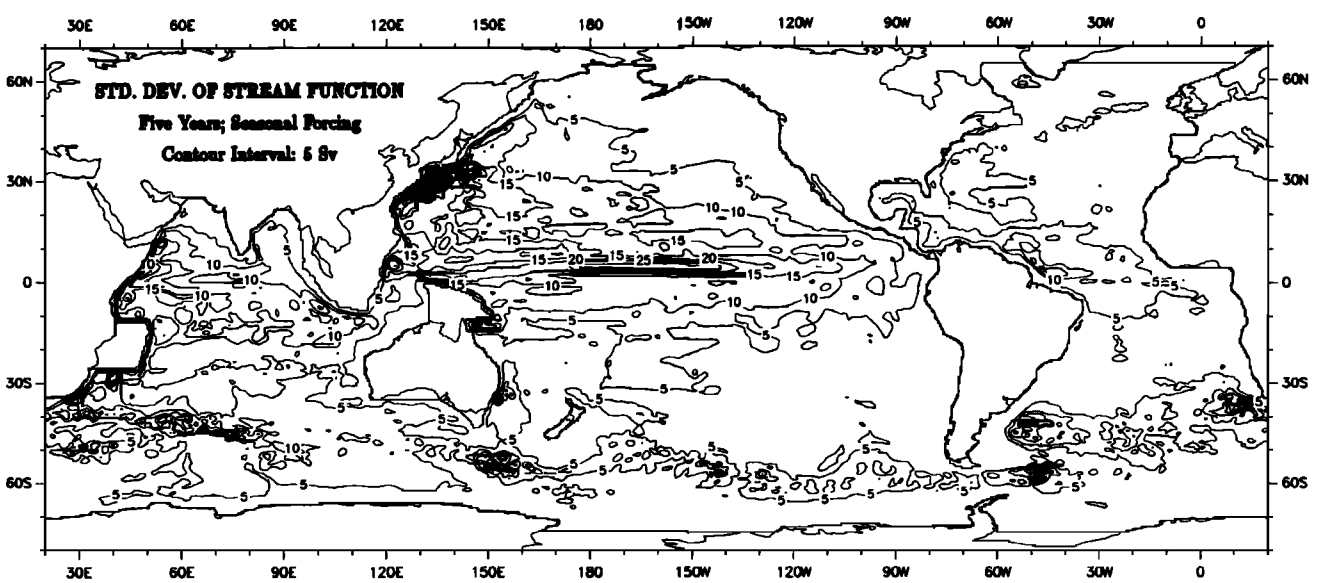

Fig. 12. Standard deviation of stream function for seasonal forcing. Contour interval is 5 Sv.

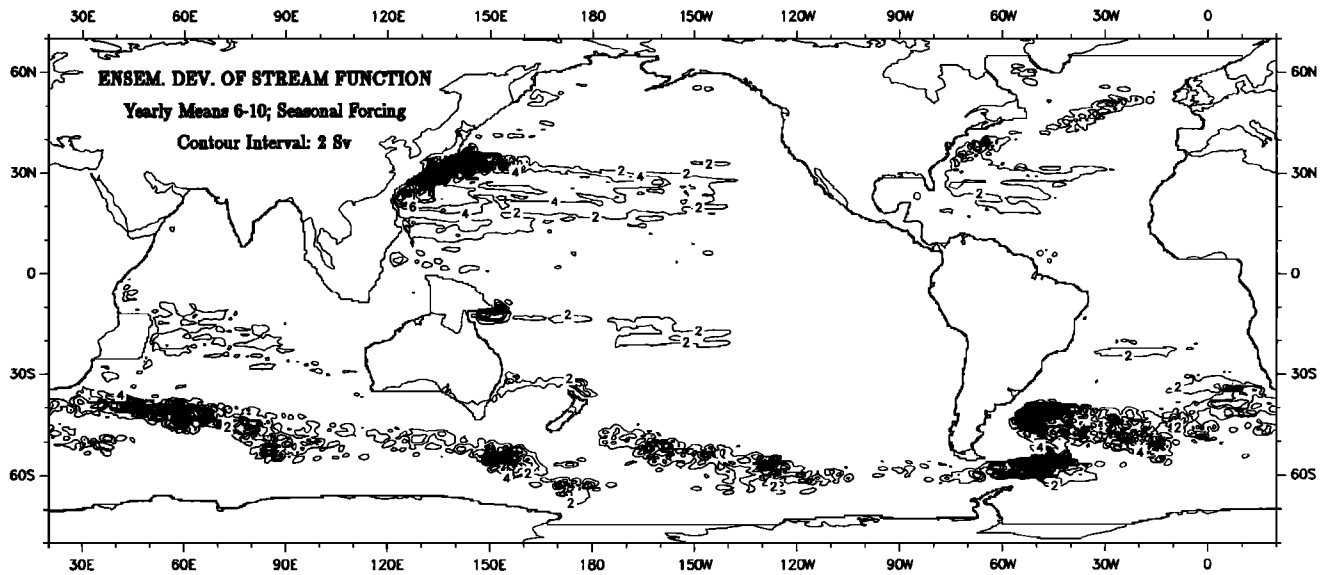

Fig. 13. Ensemble standard deviation of yearly averaged stream function for seasonal forcing over years 6–10. Contour interval is 2 Sv.

stream function fields because of the baroclinic compensation of pressure with depth. Strong mid-ocean flows occur in the Gulf Stream, the Kuroshio, the Oyashio, the Pacific North Equatorial Current, the Indian South Equatorial Current, and the flow along the Tasman Front. Also, there is a northwest flow across the South Atlantic, as part of the thermohaline circulation in the upper ocean. The surface flow of the ACC is remarkably straight compared with thermocline average currents of Plate 5, but locations of flow though narrow constrictions at depth show up in the intensity of the surface flow.

The standard deviation of surface slope is a good indicator of mesoscale instabilities. Figure 15 shows this field for the annual mean case. Sea slope variability clearly shows regions of intrinsic instability, but the field is not useful very near the equator. The most unstable currents are the Gulf Stream, the Kuroshio, the Agulhas, the Brazil-Malvinas, and the Antarctic Circumpolar currents. Moderately unstable zones exist for the East Australia Current, the Loop Current in the Gulf of Mexico, and in the middle of the Labrador Sea. Two bands of variability cross the Indian Ocean to Madagascar, one from Southeast Asia and the other from southwest Australia. These bands are associated with the thermohaline circulation "warm water route" in the upper ocean, which primarily flows north of Australia through Indonesia and secondarily flows around Tasmania and along the south coast of Australia.

Figure 16 for the seasonal-forcing case shows that new

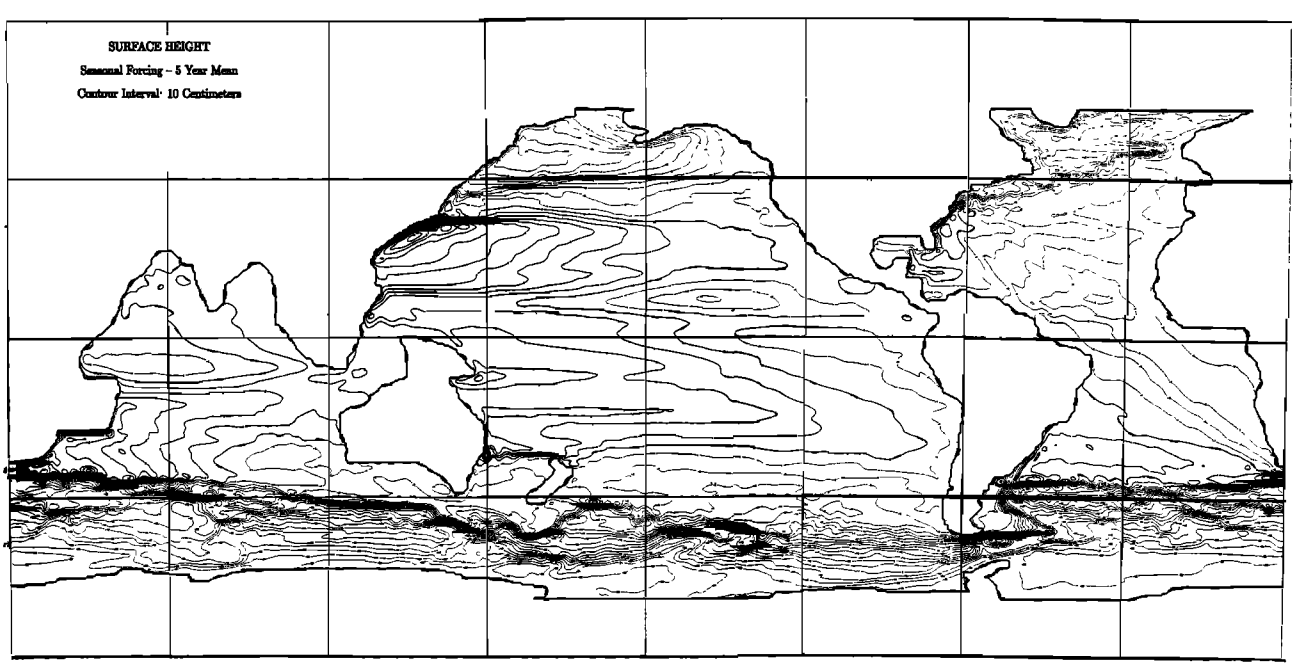

Fig. 14. Time mean surface height for seasonal forcing. Contour interval is 10 cm.

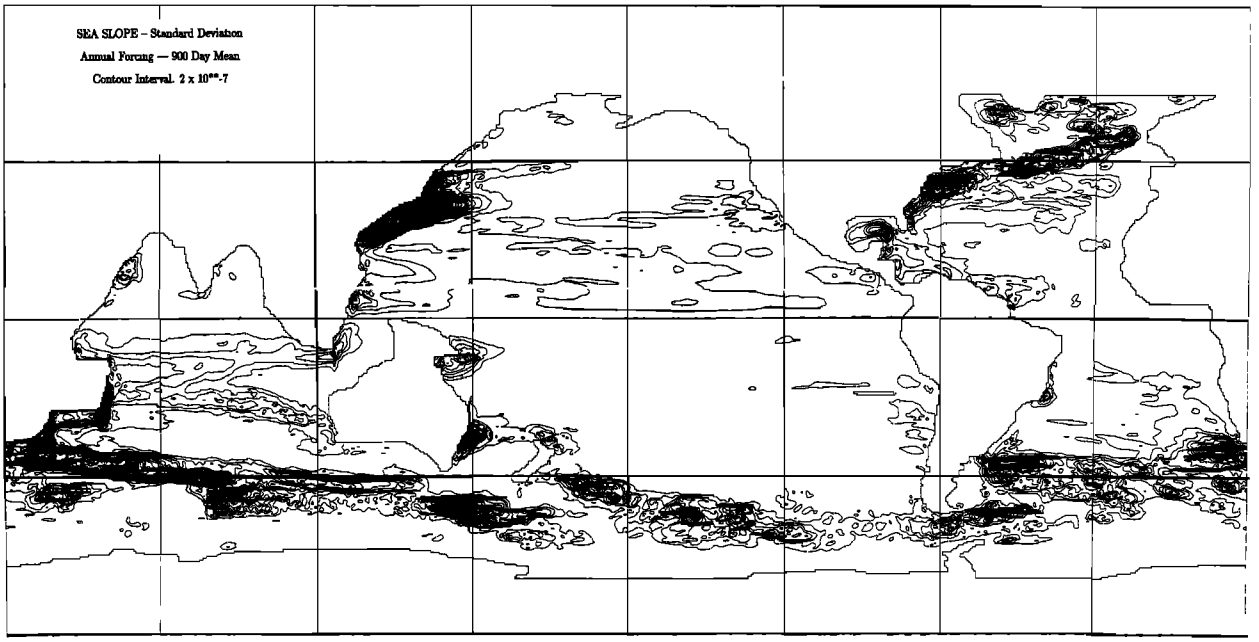

Fig. 15. Standard deviation of sea slope for annual mean forcing. Contour interval is 2×10^{-7}.

areas of activity occur which give a closer match to observed variability from Geosat observations (for example, see the sea slope variability map of *Sandwell and Zhang*, [1989]). These are along the Somali coast, Indian east coast, north Brazil coast, western Alaskan coast, and also in the mid-latitude interiors of all the ocean basins. In particular, zonal bands extending east from Central America at about 15°N and west from Australia at about 20°–25°S correspond well with those in Geosat observations. In the high latitudes, the modeled maxima are typically smaller than those in the observations by a factor of 2 or more. Further discussion of the modeled variability and comparisons with observations for the South Atlantic and northwest Pacific is given by S. Garzoli et al. (Analysis of a general circulation model product, 1, Frontal systems in the Brazil-Malvinas and Kuroshio-Oyashio regions, submitted to *Journal of Geophysical Research*, 1992) and Z. Garraffo et al. (Analysis of a general circulation model, 2, The distribution of kinetic energy in the South Atlantic and Kuroshio-Oyashio systems, submitted to *Journal of Geophysical Research*, 1992).

Figures 17–19 are vector plots which depict 0- to 500-m depth-integrated variability of two types. The longitudinal vector component is $\langle u'u' \rangle$, the square of the zonal eddy velocity, and it serves as a good indicator of regions of high

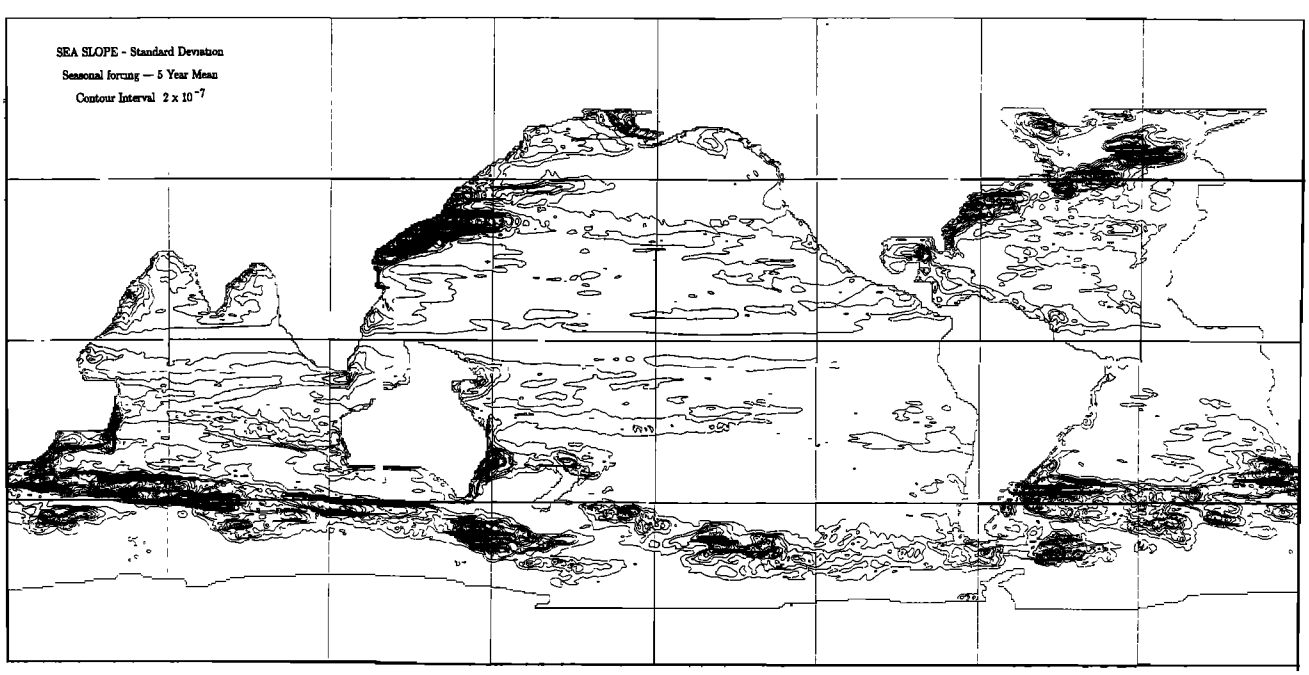

Fig. 16. Standard deviation of sea slope for seasonal forcing. Contour interval is 2×10^{-7}.

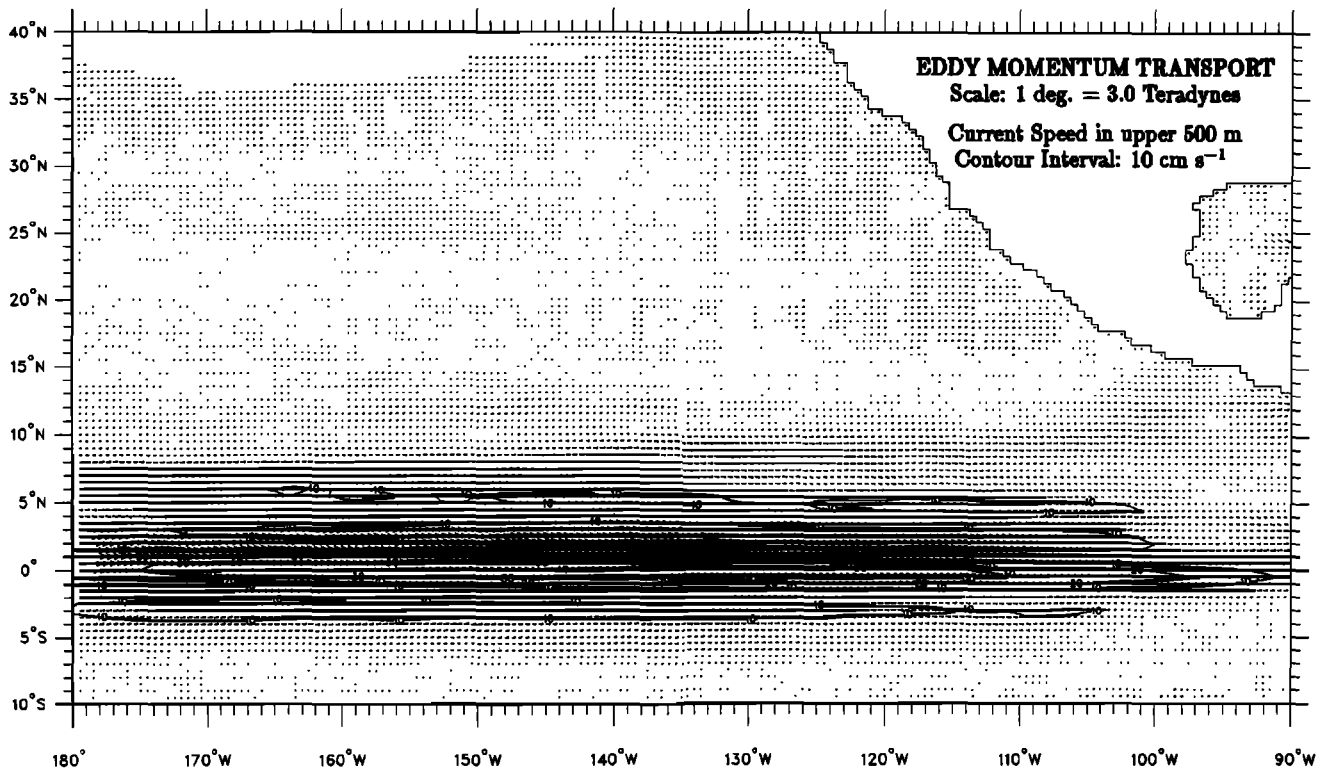

Fig. 17. Vector eddy transport of zonal momentum for the eastern Pacific. A vector of length equal to 1° of latitude/longitude spacing represents an eddy momentum (Reynolds stress) of 3.0 Tdyn. Contour plots of the time mean current speed averaged over the upper 500 m of the water column are also shown. Contour interval is 10 cm s^{-1}.

eddy kinetic energy. The latitudinal vector component is $\langle u'v' \rangle$, the covariance of the zonal and meridional velocity components, and it gives a measure of the meridional transfer of zonal momentum by eddies. The divergence (or convergence) of the vector fields is a measure of the net deceleration (or acceleration) of the time mean zonal velocity by eddy effects. Vector scales accordingly are given in dynamical units of teradynes. Included with the vector plots are contours of the mean current speed in the upper 500 m of the water column, with a 10 cm s^{-1} contour interval. The three plots are for the eastern Pacific Ocean, the Indian Ocean, and the North Atlantic Ocean. These same areas will also be examined in subsequent sections in regard to eddy fluxes of heat and salt.

Figures 17–19 all show significant eddy kinetic energy in zonal currents near the equator and in low-latitude western boundary currents. Mid-latitude western boundary currents and certain portions of the Antarctic Circumpolar Current have large zonal eddy kinetic energy as well.

The meridional transport of zonal momentum by eddies is not very large by comparison with the other component of the vector field in most currents, other than in the low-latitude western boundary currents. In particular, this means that inferences about negative viscosity effects are not very reliable on the basis of looking only at the derivative of the latitudinal component of the vector fields, when the derivative of the longitudinal component could easily be much larger and of a different sign. (These latter effects redistribute momentum along the cores of the strong currents.) A few exceptions are found in the Antarctic Circumpolar Current near 55°E and 75°E, where negative viscosity effects appear to converge momentum into the current core. Similar effects appear in the Gulf Stream near 65°W and in the North Atlantic Current near 50°W, but these are considerably weaker than those in the ACC.

We now discuss time series and spectra of stream function at 16 key locations. The time series are based on 3-day instantaneous sampling for a 10-year period, and unsmoothed spectra are computed from those records. Respectable levels of mesoscale variability will be demonstrated, in spite of the somewhat marginal 0.5° grid spacing. Also a variety of time-dependent behaviors will be noted, which could provide a fairly stringent test for the validity of the model in representing the complexity of ocean currents on a global basis.

Figure 20 shows many interesting features. The Gulf Stream off Cape Hatteras varies between 15 and 45 Sv and shows a broad maximum of variability in the range of 100-day to yearly periods. The Kuroshio off Japan is much stronger (up to 200 Sv) owing to a recirculation which builds with a time scale longer than a year. The Brazil Current at 40°S oscillates about a mean of 75 Sv with a noticeable annual cycle. At the Drake Passage, oscillations of about 8 Sv with annual and semiannual frequencies ride a mean flow of about 200 Sv. The Indonesian throughflow is 17 ± 5 Sv, with 20- to 40-day waves in addition to seasonal effects. The Agulhas flow at 70 Sv is fairly devoid of a seasonal cycle, but has 30- to 50-day waves. The Somali and Oyashio currents have strong seasonal cycles with internal variability near 50 and 30 days, respectively. The Labrador Current of 40 Sv has seasonally forced oscillations only. The Madagascar Current of 45 Sv has a broad range of fluctuations in the range 30–100 days. The California Current is weak but has a seasonal reversal and 30-da, waves. The East Australia

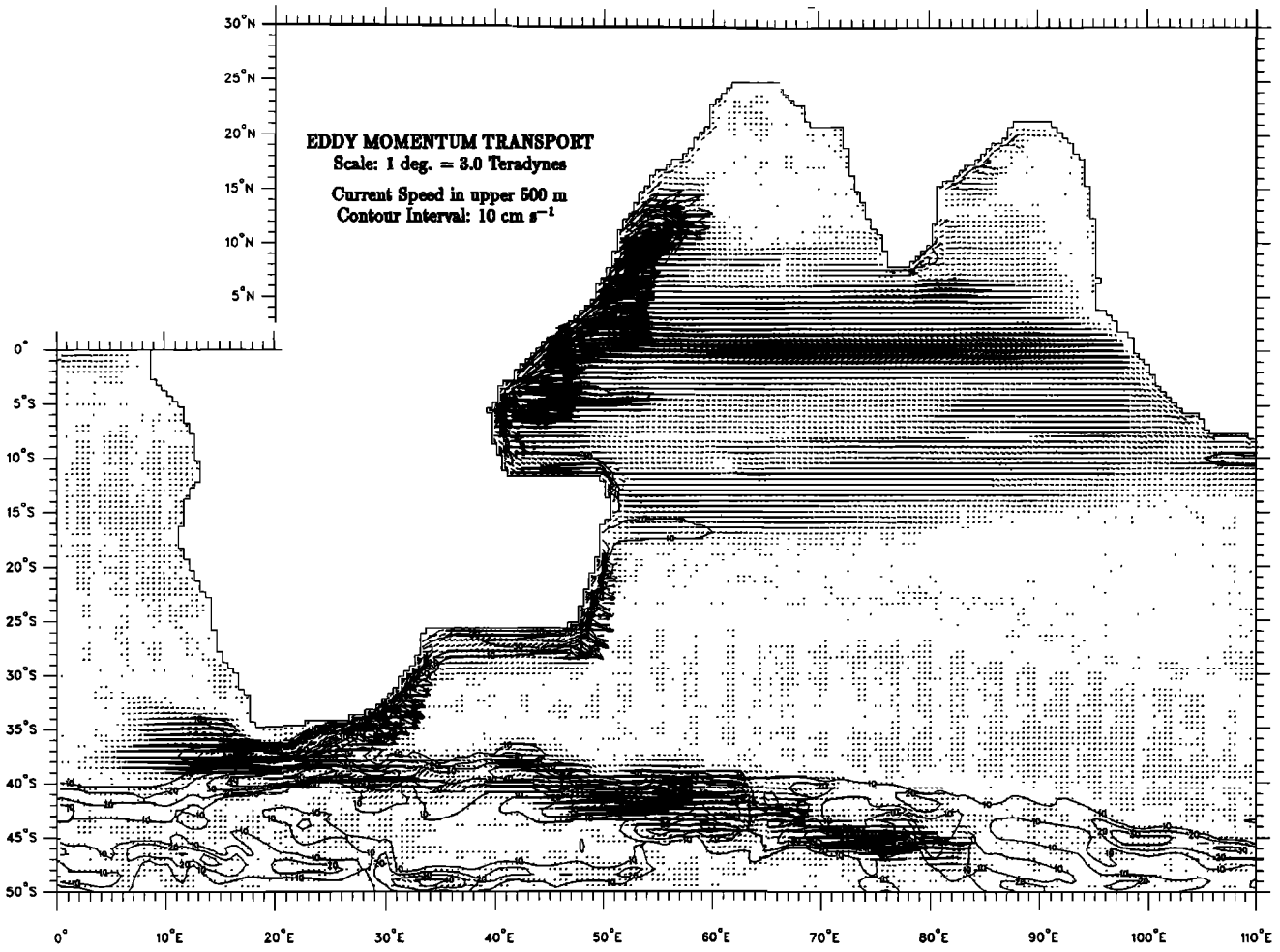

Fig. 18. As in Figure 17, but for the Indian Ocean.

Current at 30°S shows low-frequency activity in the range 100-400 days, while the transport through the Tasman Sea shows higher frequencies. The North Brazil Current crossing the equator has a strong seasonal cycle plus 50-day waves. The Loop Current in the Gulf of Mexico shows broad variability at 200–400 days. Finally, the Gulf of Alaska has a clear seasonal cycle with monthly variations.

We now examine time series and spectra of v velocity at 37.5 m for eight locations, to determine whether the magnitudes of currents as well as their variability are realistic. These are given in Figure 21. The Gulf Stream flow is strong in spite of small net transport (80 cm s^{-1} with much fluctuation). The flow in the Gulf of Mexico looks semiannual. The Somali Current has an impressive annual range from -60 to $+120$ cm s^{-1}. The east central Pacific is dominated by 30-day waves of 50 cm s^{-1} magnitude. The Agulhas is strong southward with high-frequency fluctuations. The East Australia Current is dominated by seasonal forcing. Fluctuations of tens of centimeters per second and with a broad frequency distribution are found in two unstable regions of the Antarctic Circumpolar Current, near the Kerguelen Plateau and the Macquarie Rise.

A further discussion of the modeled variability of the meridional velocity field in the tropical oceans, with particular emphasis on the Pacific, is given by R. M. Ponte and D. S. Gutzler (Forty- to sixty-day oscillations in the western tropical Pacific: Results from an eddy-resolving global ocean model, submitted to *Journal of Geophysical Research*, 1992). They find a preponderance of 50-day variability in the western tropical Pacific.

Finally, we discuss time series and spectra of temperature at 37.5 m at eight locations. These are shown in Figure 22. Three equatorial Pacific time series have temperature oscillations of about 1°C, with frequencies transitioning from 50- to 30-day prominence in moving from west to east. Both the North Brazil and the ACC in the Drake Passage show seasonal dominance and temperature shifts of about 4°C and 1–2°C, respectively. The Kuroshio, Agulhas, and ACC in the Pacific all show a mix of seasonal cycle and internal instabilities.

The spatial aspects of variability in both the temperature and salinity fields can give considerable insight into the location of seasonal and mesoscale variations in various parts of the world ocean. Discussion of these features is deferred to the two sections which follow.

6. THERMODYNAMICS

It is instructive to begin the discussion of thermal effects by examining the nature of the eddy signal in a well-resolved portion of the model ocean. Figure 23*a* shows instantaneous temperature in early October of year 10 at 37.5 m in the

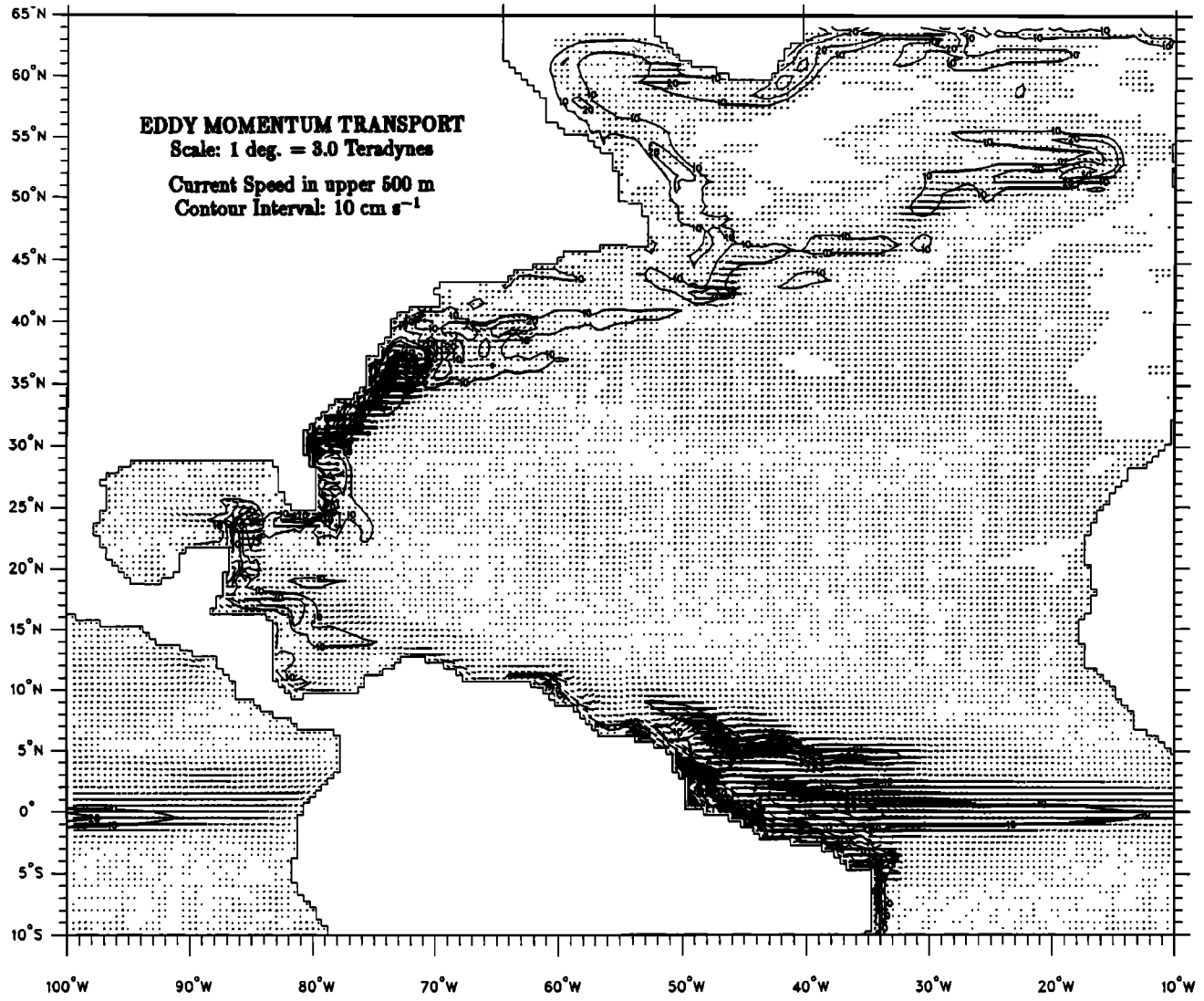

Fig. 19. As in Figure 17, but for the Atlantic Ocean.

tropical Pacific, whereas Figure 23*b* shows the 5-year averaged field. Tropical waves are quite clearly visible on the temperature front in the eastern Pacific between the cold tongue of equatorial upwelling and the warm core of the North Equatorial Countercurrent. The waves are nonlinear and irregular, and they appear to be in somewhat varied stages of wave breaking. Thus they have the appearance of genuine turbulence, in addition to being wavelike. The turbulent nature of the waves is borne out by animation segments on the videotape which is available from the authors.

Note that the time mean thermal field has another front between the NECC warm tongue and the cold extension of the Costa Rica Dome. This area seems eddy active, as does a region further north extending southwestward from Central America at about 15°N. Eddies in this latter area have only been recently identified by a number of observationalists using Geosat data [e.g., *Hansen and Maul*, 1991].

Judging from Figure 23, no area of the tropical Pacific is particularly devoid of eddy activity. This includes areas west of the date line, particularly those near the SECC off New Guinea and near the NECC off the Asian boundary. Also, there are waves east of the date line and south of the equator on the southern side of the tongue of equatorial upwelling.

Figure 24 shows the long-term temperature averaged over the upper two layers of the model (the depth range 0–50 m). This temperature is somewhat freer than that of the uppermost layer, and it thereby gives a better idea of model performance. In particular, some very sharp fronts exist in selected western boundary currents and along parts of the Antarctic Circumpolar Current. Certain of the latter fronts occur when the ACC is constrained to pass through narrow gaps at depth (such as fracture zones in mid-ocean ridges). These fronts could be compared with high-resolution observations made during seasons where surface mixed layers did not obscure frontal structures. Of course, these fronts in the depth range 0–50 m are much sharper than those of the surface-forcing data, even after model variability is averaged in time.

Cold upwelling signatures are present in the tropical Atlantic, the west Indian Ocean, and along the west coasts of Africa, North America, and South America. The warm pool of the western Pacific extends through the Indonesian passage. In high latitudes, subarctic seas of the northern hemi-

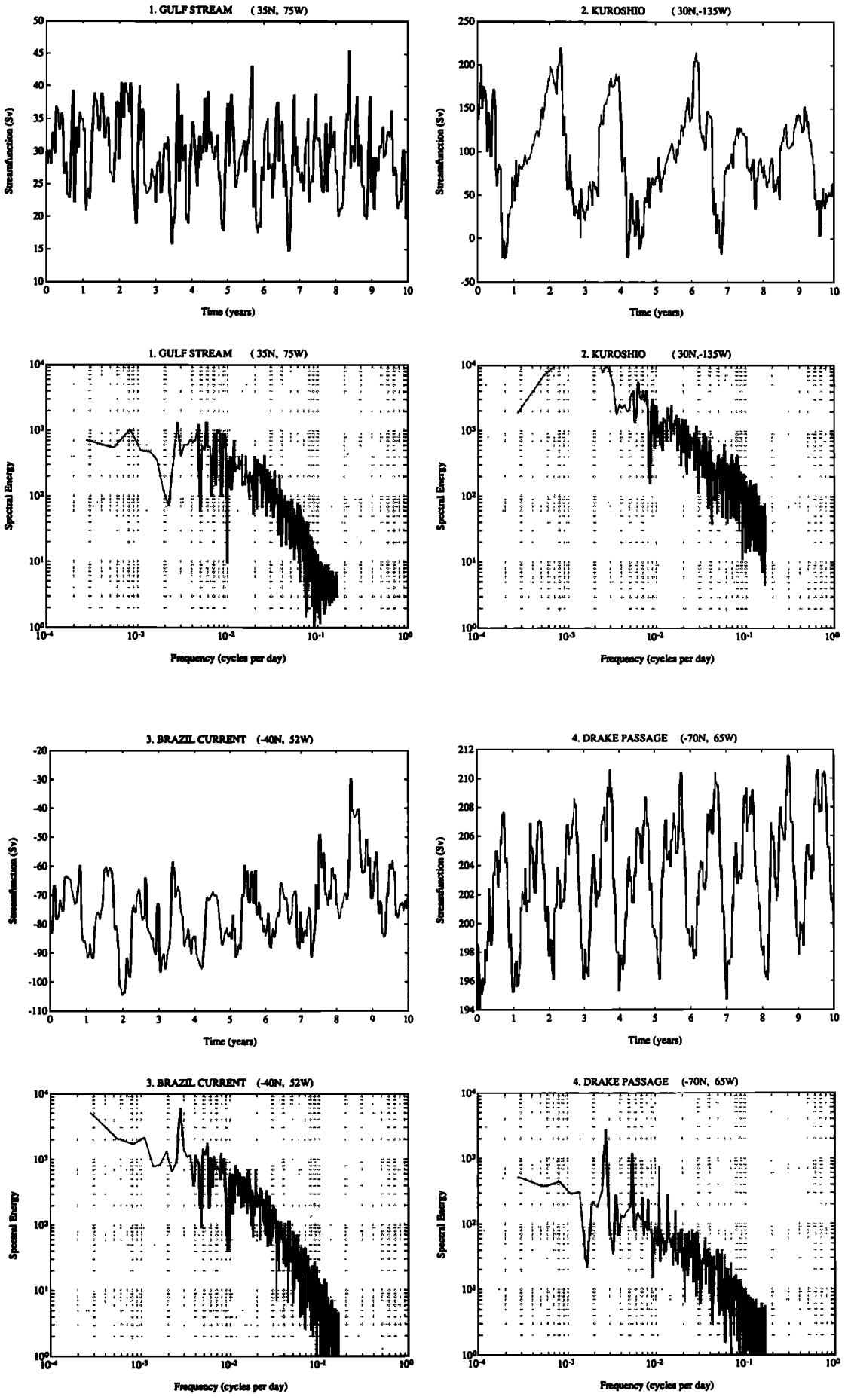

Fig. 20. Spectra of transport stream function for the 10-year seasonal run. Locations are indicated above each plot.

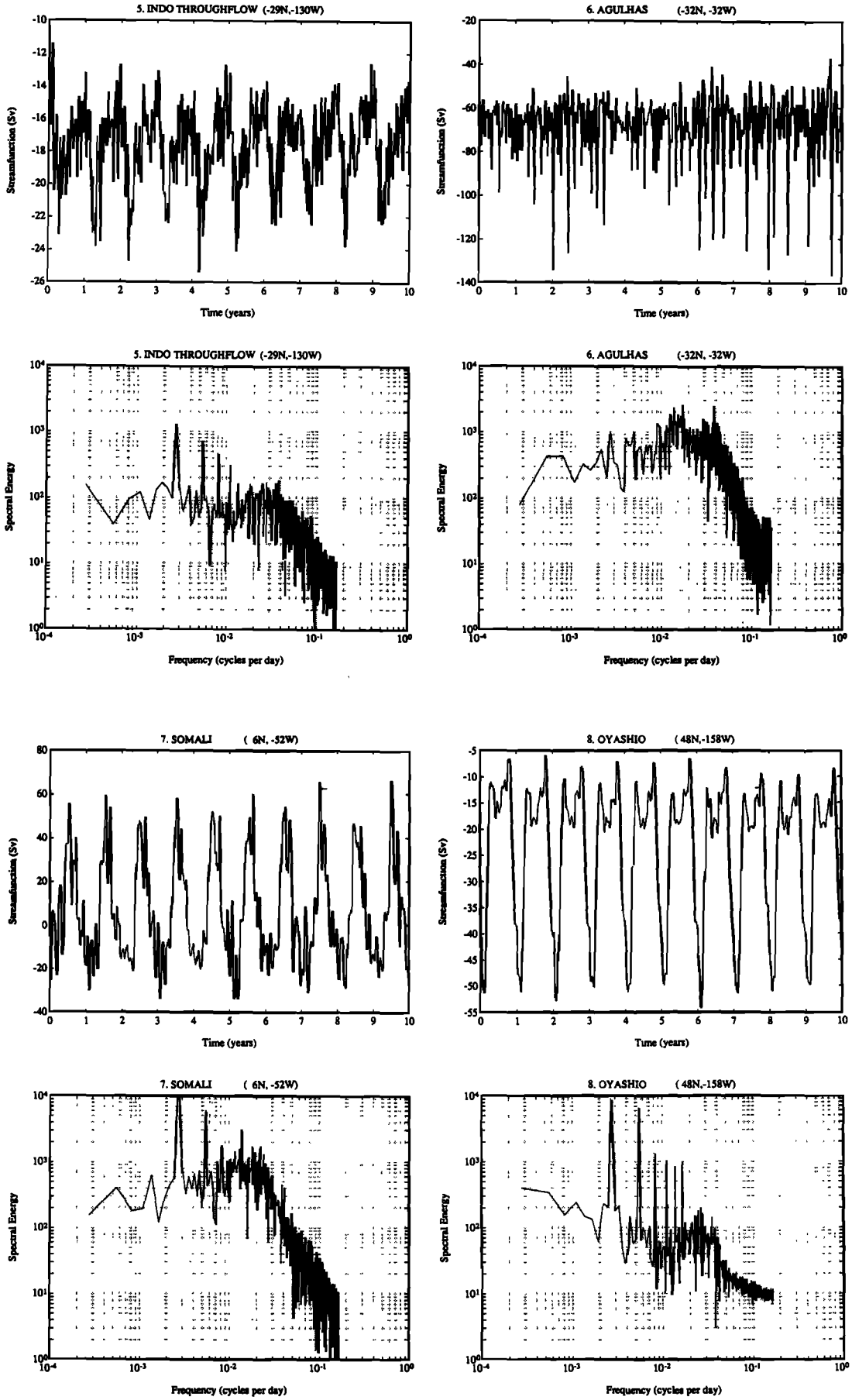

Fig. 20. (continued)

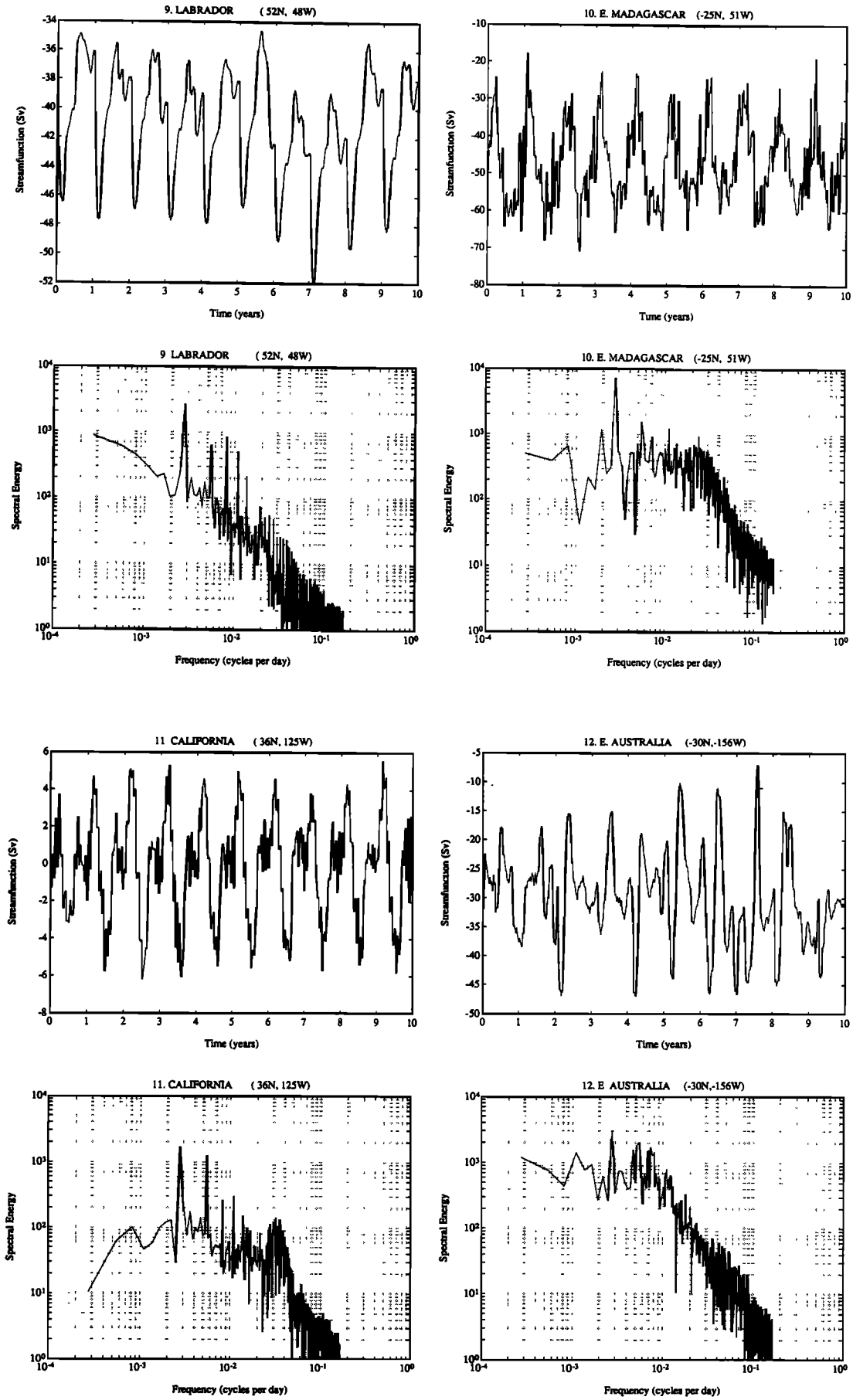

Fig. 20. (continued)

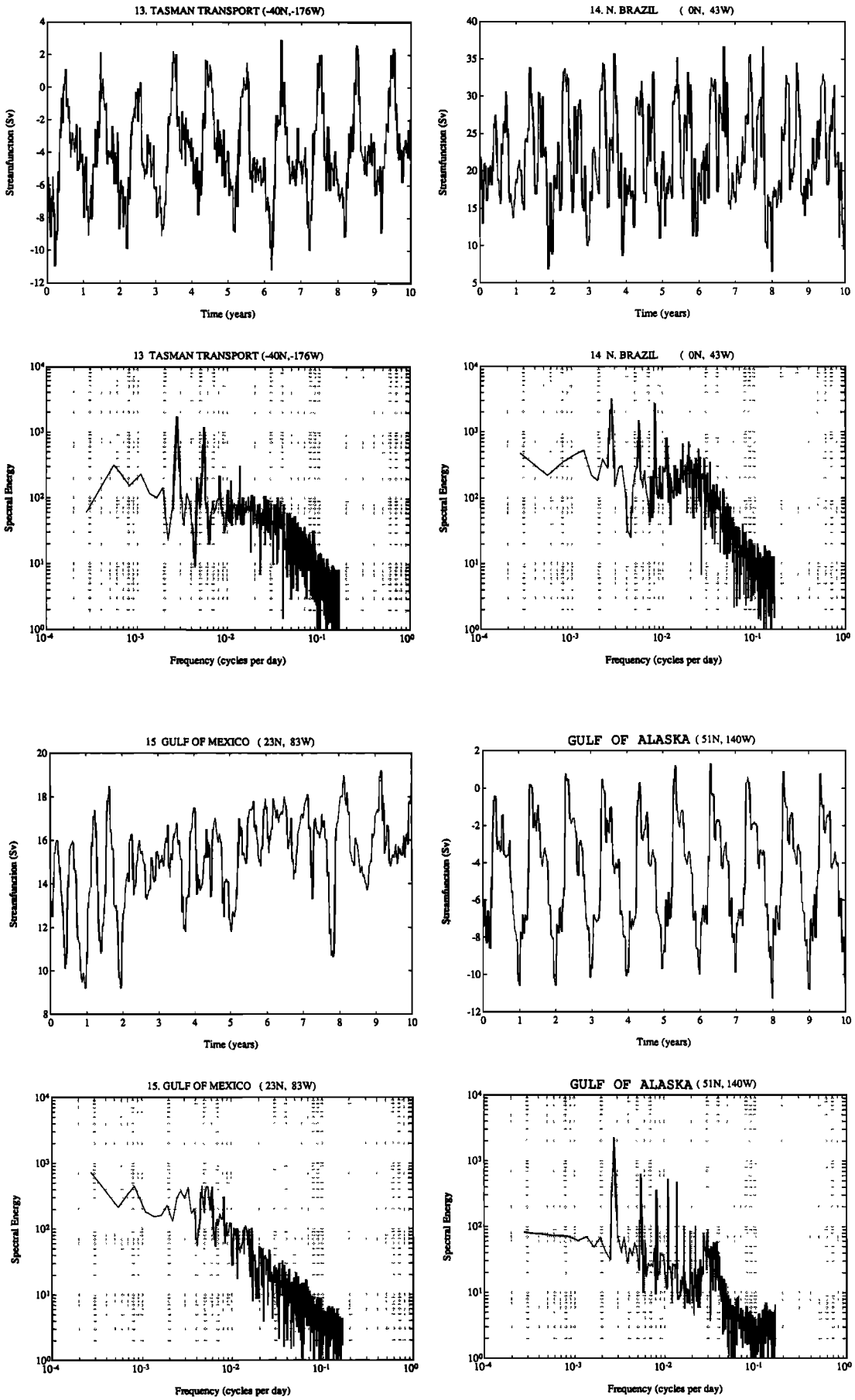

Fig. 20. (continued)

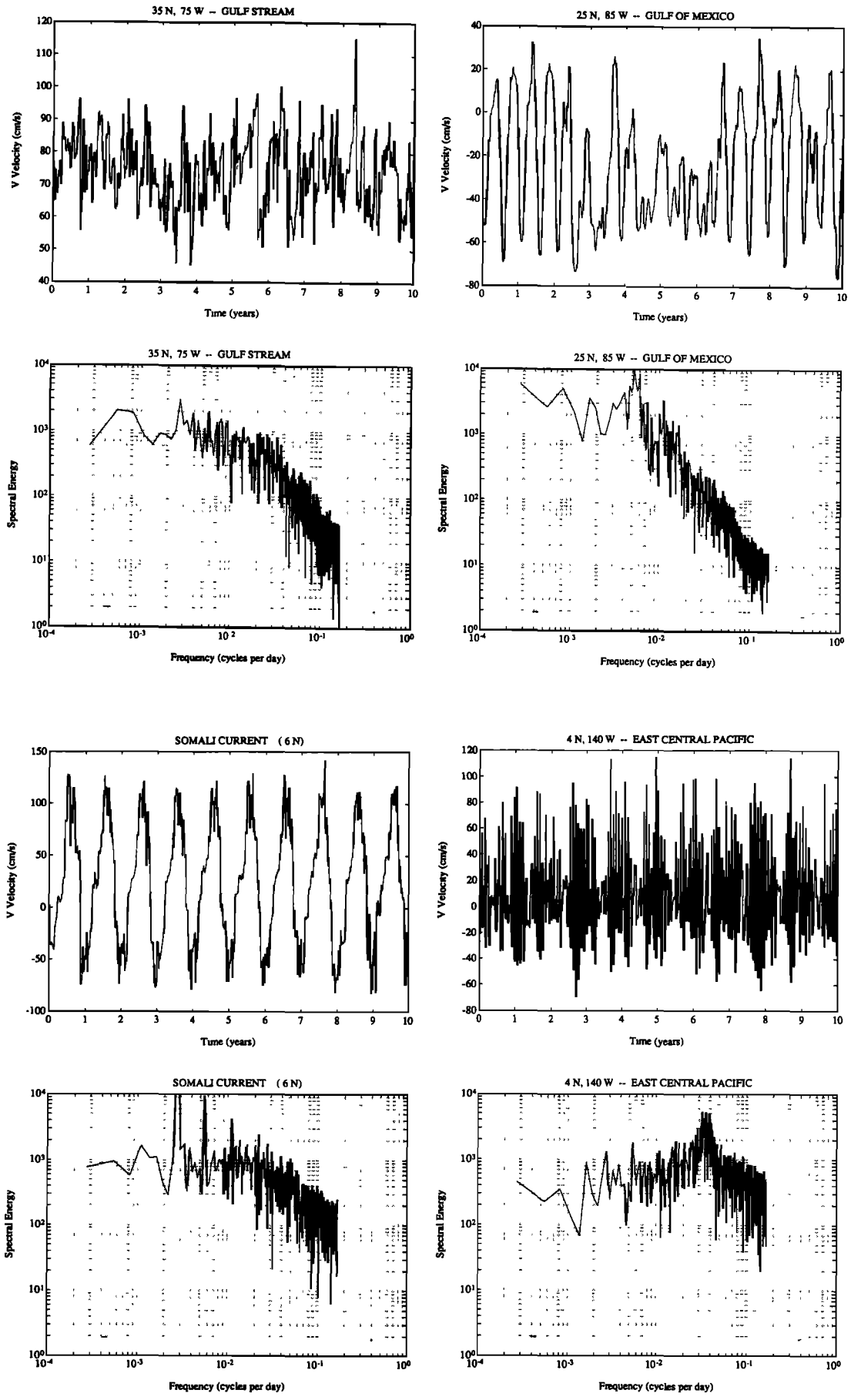

Fig. 21. Spectra of v velocity component at 37.5 m.

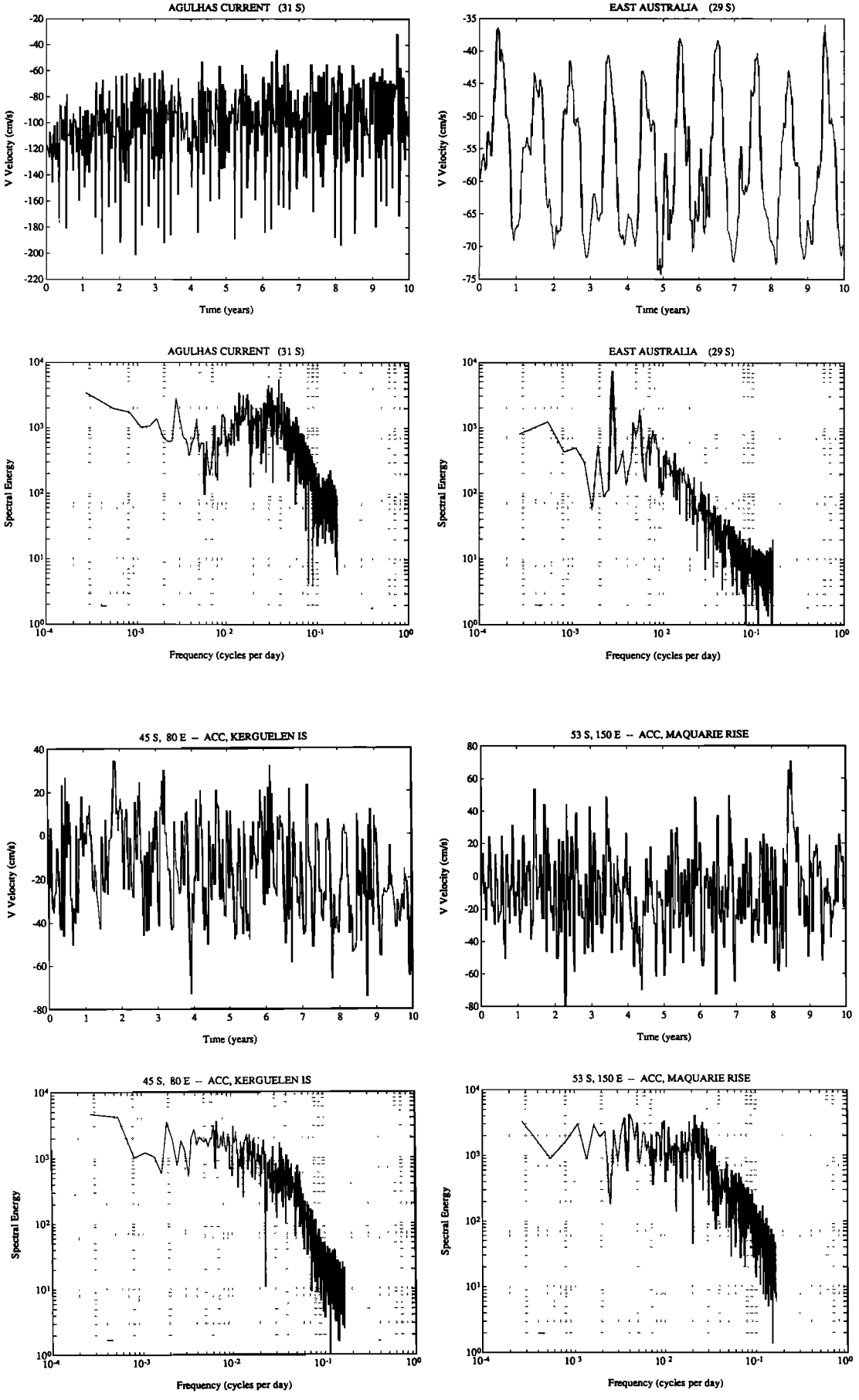

Fig. 21. (continued)

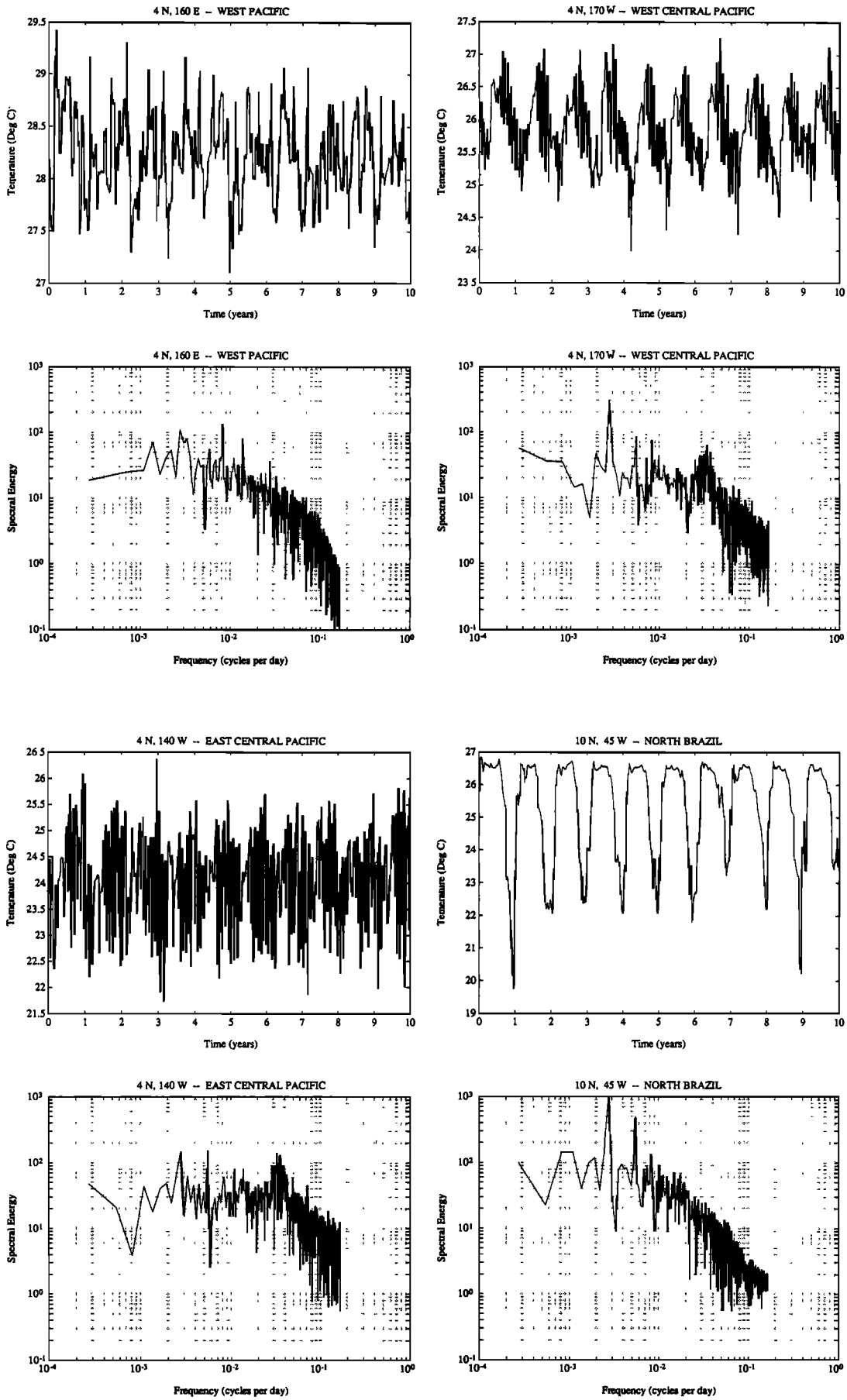

Fig. 22. Spectra of temperature at 37.5 m.

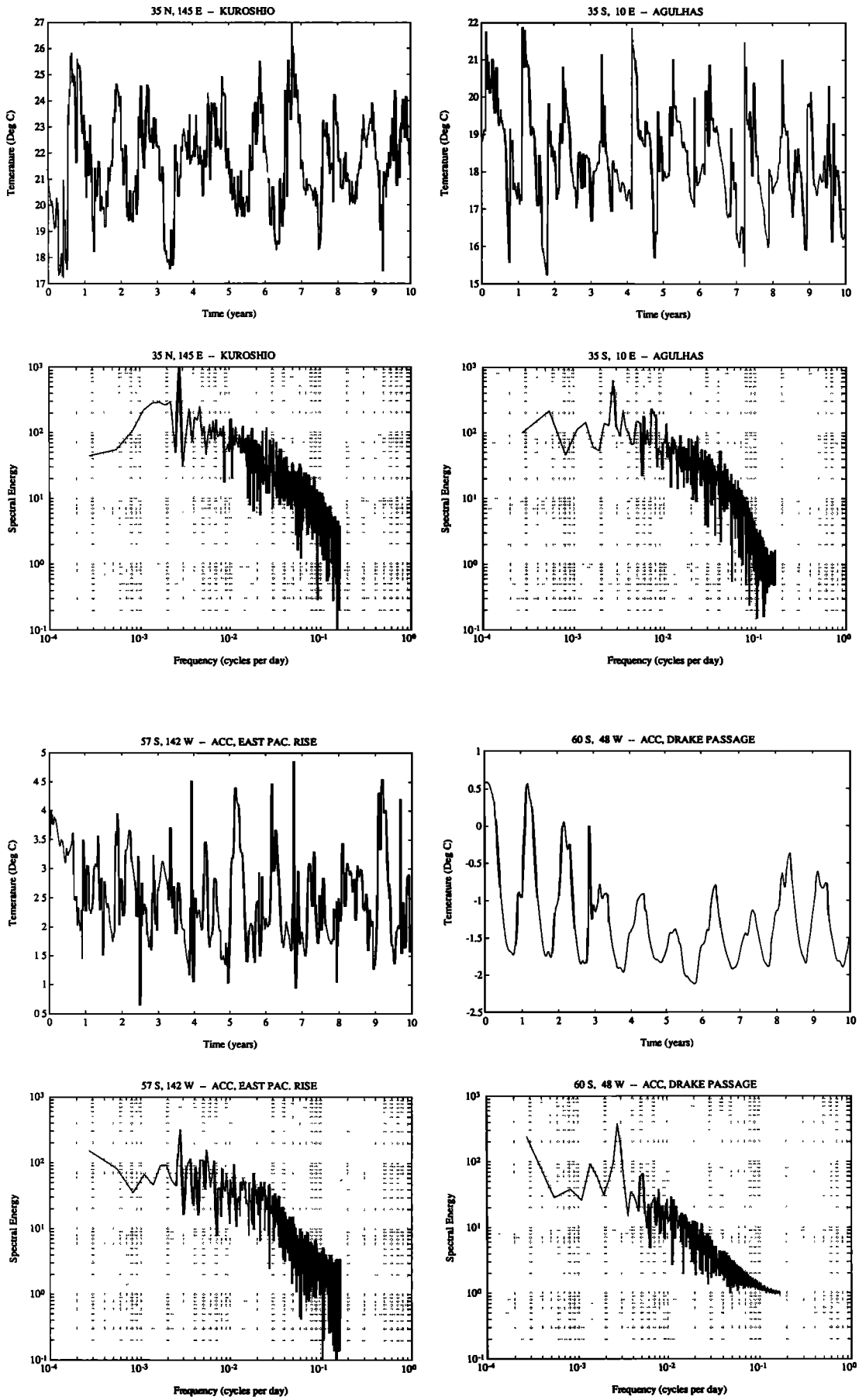

Fig. 22. (continued)

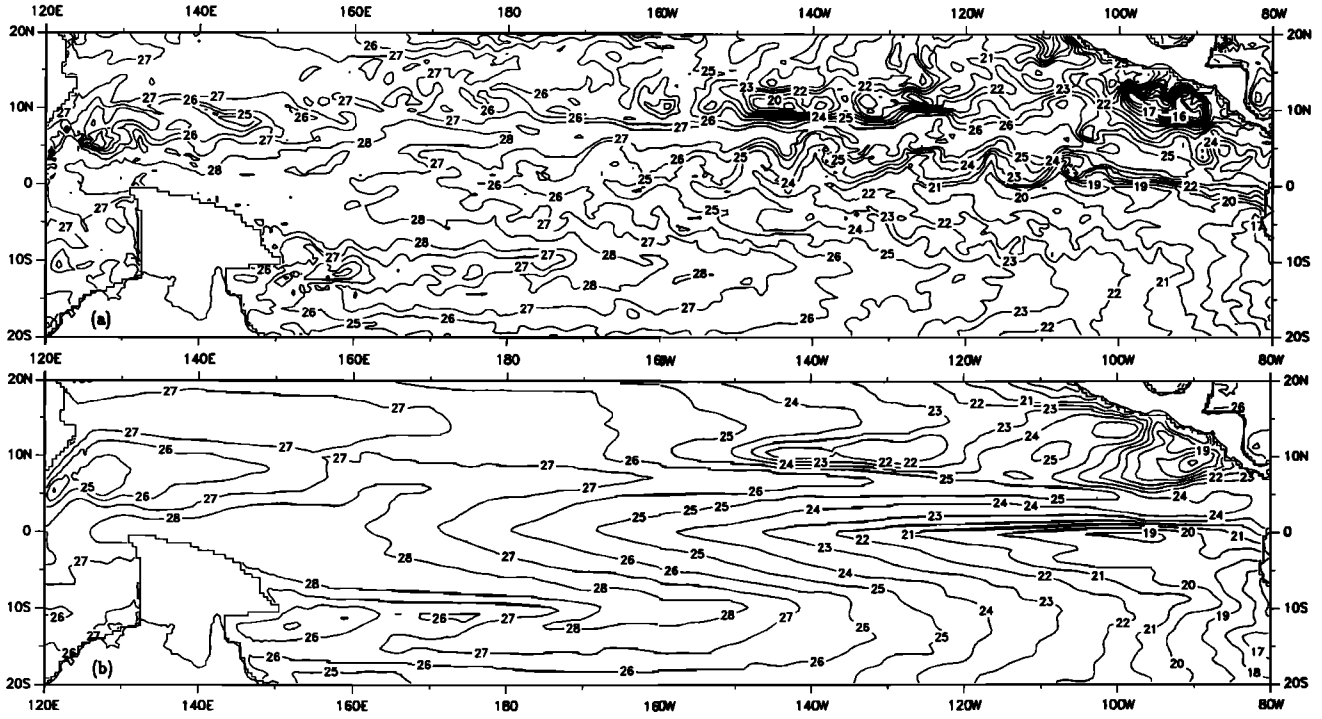

Fig. 23. Simulated (*a*) instantaneous and (*b*) 5-year average temperatures in the tropical Pacific at 37.5-m depth (model level 2). The instantaneous field is for early October in year 10 of the seasonally forced extension run, and the smooth field is averaged for years 6–10. Contour interval is 1°C.

sphere are not as cold as observed, especially in the Atlantic where an artificial wall turns flow westward that would normally enter the Arctic marginal seas. Subzero temperatures are found around Antarctica, showing sea ice coverage implicit in the Levitus data set used for surface forcing.

Figure 25 gives the standard deviation of model surface temperature (12.5 m), which represents primarily the effect of seasonally varying forcing and secondarily the effect of eddies. The amplitude of a sinusoidal seasonal cycle would be twice as large as indicated, of the order of 4°–5°C in mid-latitudes away from coasts. Some of the strongest signatures are those of Somali upwelling, California coastal upwelling, and confluence areas. The confluence regions (Kuroshio-Oyashio, Brazil-Malvinas, Gulf Stream–Labrador, and Agulhas-ACC) may be showing the signs of eddy activity at strong fronts more than seasonal circulation changes. Finally, mid-ocean seasonal variability is rather small in the tropics away from lateral boundaries.

The distribution of long-term average surface heat flux is shown in Figure 26. A contour interval of 20 W m^{-2} was

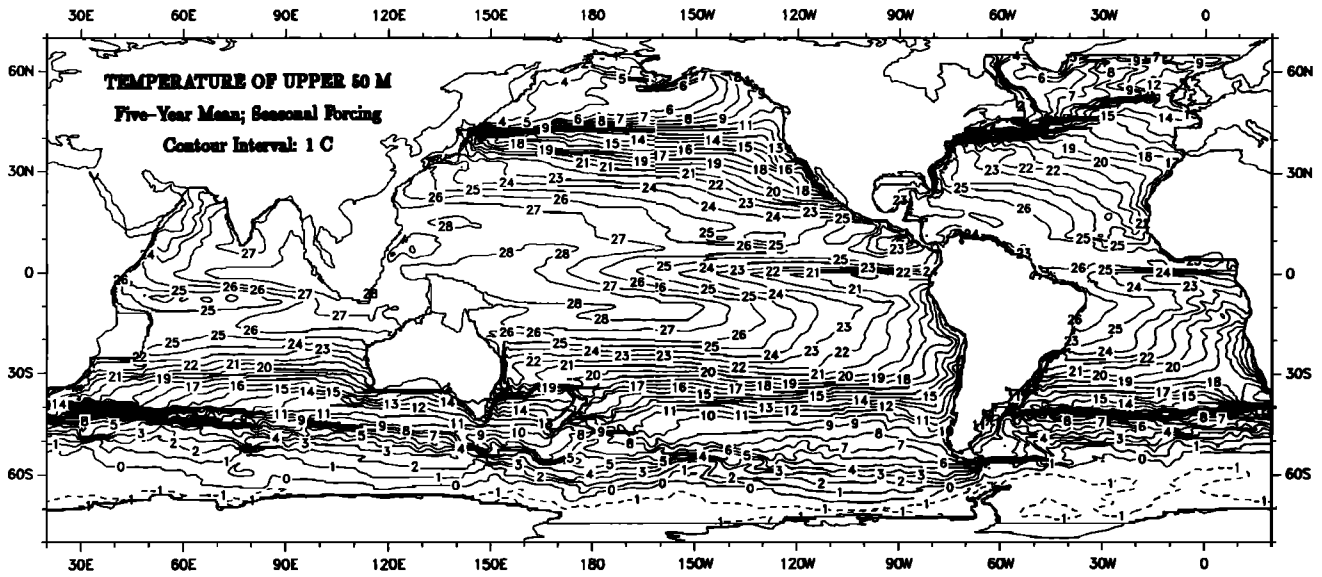

Fig. 24. Five-year average of temperature in depth range 0–50 m for the seasonal-forcing case. Contour interval is 1°C.

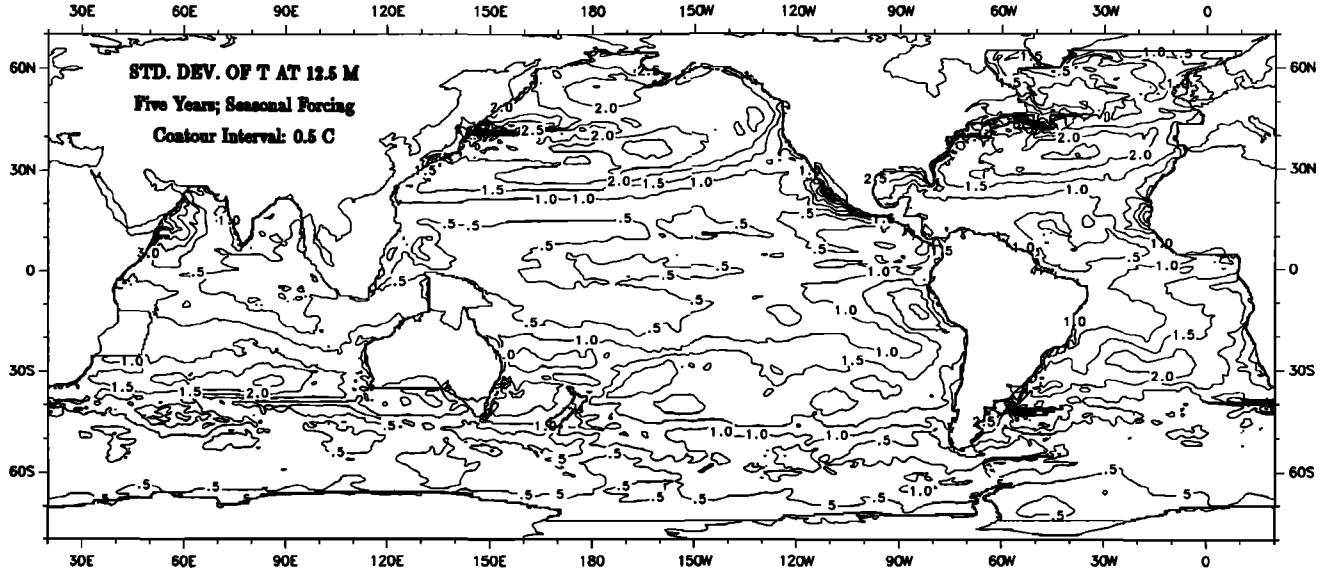

Fig. 25. Standard deviation of annual average temperature for years 6–10 of the seasonal run. Contour interval is 0.5°C.

chosen to enhance the detail of the large, relatively featureless mid-ocean, mid-latitude zones, which complicate satellite estimates of ocean heat flux. Tropical areas show large, consistent zones of positive heat flux, which are related to upwelling, as do some eastern boundary regions. Large heat losses occur in the Kuroshio and the Gulf Stream regions. However, the high-latitude zones of the southern hemisphere are difficult to interpret, being complicated in part by many positive and negative areas where fluxes are unsmoothing Levitus surface data in response to complexities in the simulated ACC. However, as is shown by McCann et al. (1992), the net flux out of the southern ocean is nearly zero, an issue that we will return to later when we discuss heat transport.

Figure 27 shows the vertically integrated heat fluxes due to the robust diagnostic forcing below 710 m, plus any such forcing in the thermocline within 10° of the northern and southern boundaries. The contour interval is the same as for the surface fluxes. Other than in the small enclosed Sulu Sea, where the deep forcing data were rather poor (S. Levitus, personal communication, 1988), there are no significant deep fluxes between 30°S and 30°N. A small amount of forcing in the North Pacific is needed to augment convection in the upper water column. In the southern ocean, deep restoring is required to sustain cold temperatures around Antarctica and below the ACC, implying insufficient direct production and spreading of Antarctic Bottom Water. In the North Atlantic, large heat fluxes out of the thermocline and deep water are required to maintain the temperature signatures not only of North Atlantic Deep Water but also of the East Greenland Current, since neither inflow occurs at the 65°N wall.

The core of North Atlantic Deep Water in the real ocean consists of overflow water from the Denmark Strait and the Iceland-Scotland Ridge system. The dense overflow rate has

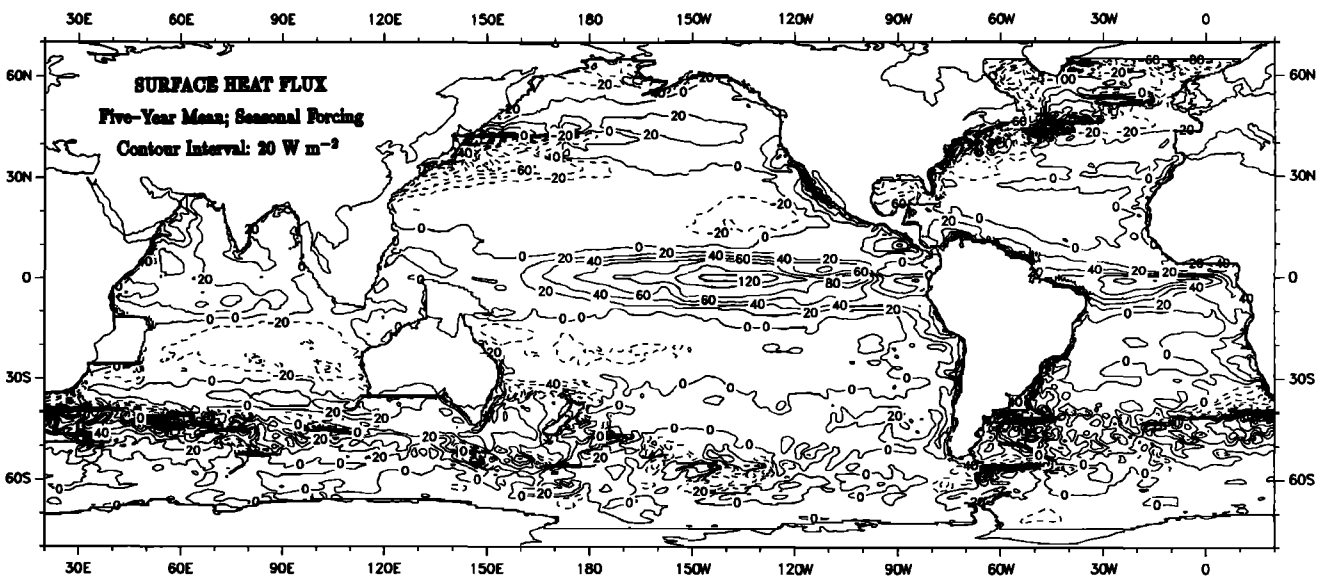

Fig. 26. Surface heat flux for years 6–10 of the seasonal case. Contour interval is 20 W m^{-2}.

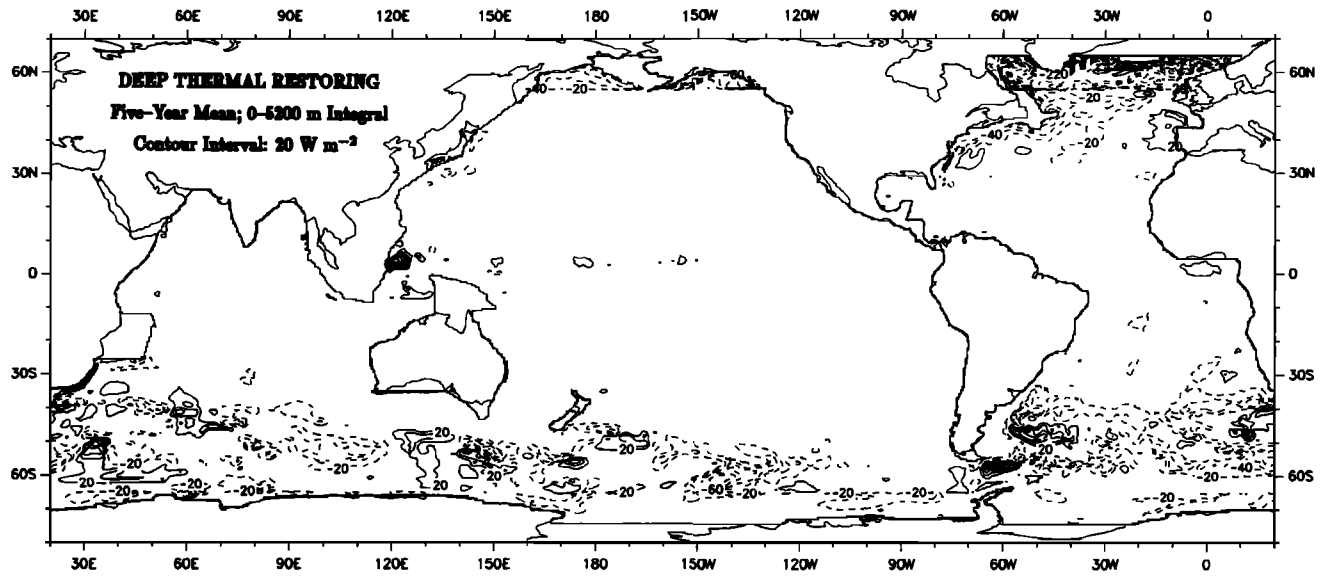

Fig. 27. Deep heat flux for years 6–10 of the seasonal case. Contour interval is 20 W m^{-2}.

been estimated from direct measurements to total 5.6 Sv [*Dickson et al.*, 1990]. Additional outflow in surface currents such as the East Greenland Current brings the total contribution of mass from the Arctic to be about 10 Sv (as was estimated earlier by *Worthington* [1976]). The surface outflow affects the Labrador Current and ultimately could play a role in causing the Gulf Stream to separate at Cape Hatteras rather than farther north as modeled. The lack of a proper connection to the Arctic understandably creates difficulties in the model, and this will be remedied in future studies.

Figures 28 and 29 are intended to highlight areas of intrinsic variability due to mesoscale eddies. Figure 28 shows the standard deviation of annual mean temperatures at 37.5 m for years 6–10 of the seasonally forced run, whereas Figure 29 shows the standard deviation of 37.5-m temperature in the 900-day period with annual mean forcing. Although Figure 28 has a lot of sampling noise, the simple statistical technique does identify the regions of intrinsic (nonseasonal) variability, since they agree in large part with those in the annually forced case. The most thermally active areas are the Gulf Stream and Gulf Stream Extension, the Oyashio-Kuroshio region, the Brazil-Malvinas confluence, the Agulhas Extension and Retroflection, and the East Australia Current. There are numerous areas of weaker activity which appear in both figures. Among these, a few of the areas may be yet undetected regions of eddy activity in the real ocean, and several of these are only recently identifiable in statistical analyses of Geosat height data. Additional maps of thermal variability at deeper levels in the annual-forcing case are given by *Semtner and Chervin* [1990].

Figures 30–32 are regional views of the eddy heat trans-

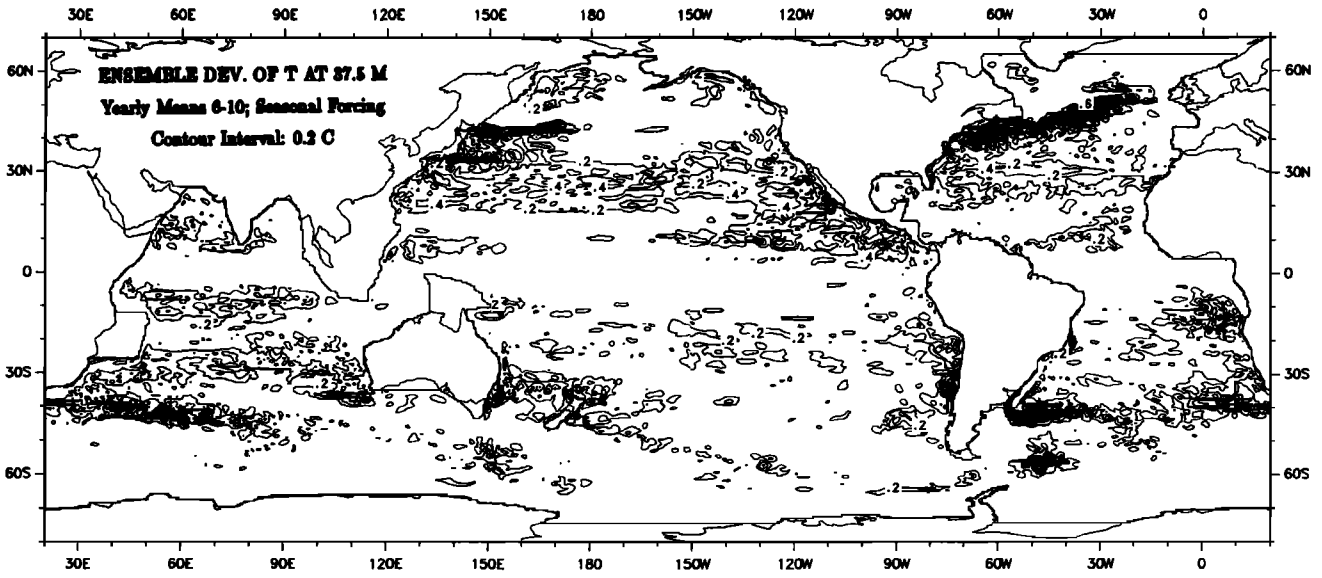

Fig. 28. Ensemble standard deviation of annual average temperature at 37.5 m. Contour interval is 0.2°C.

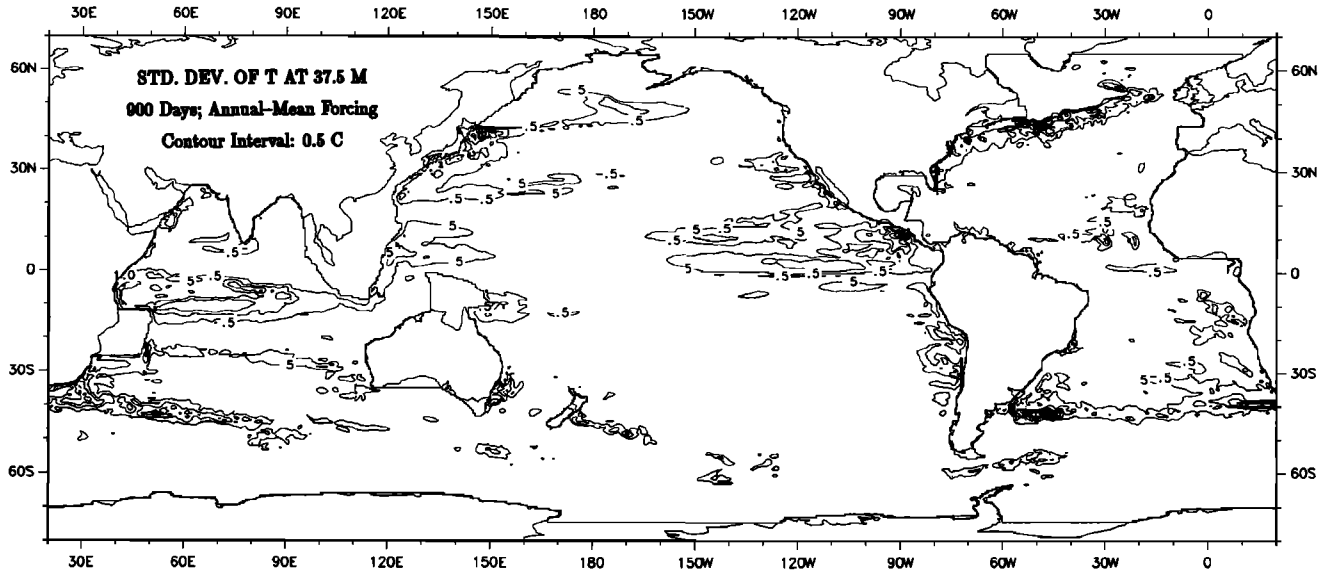

Fig. 29. Standard deviation of 37.5-m temperature for annual mean forcing. Contour interval is 0.5°C.

port, with components $\langle u'T' \rangle$ and $\langle v'T' \rangle$, over the final 5 years of the seasonally forced experiment. The transport has been integrated over the upper 500 m of the water column at each grid point and plotted with a vector scale such that 1° of latitude/longitude represents a heat transport of 1.5 TW. To assist in the interpretation of the transports, the time mean temperature is shown averaged from the surface down to 500 m (or the bottom if that comes first).

Figure 30 for the eastern tropical and mid-latitude Pacific shows very large eddy heat transports to the east in the latitude belt 4°–8°N and large transports to the west in the belt 1°–3°S. These are the latitude ranges of the North Equatorial Countercurrent and the equatorial branch of the South Equatorial Current. The eddies produce a significant transport of heat in the direction of the mean flow which is not included in that by mean currents. At least some of this transport is associated with the seasonal cycle. In the latitude band 2°–5°N, there are large transports between the

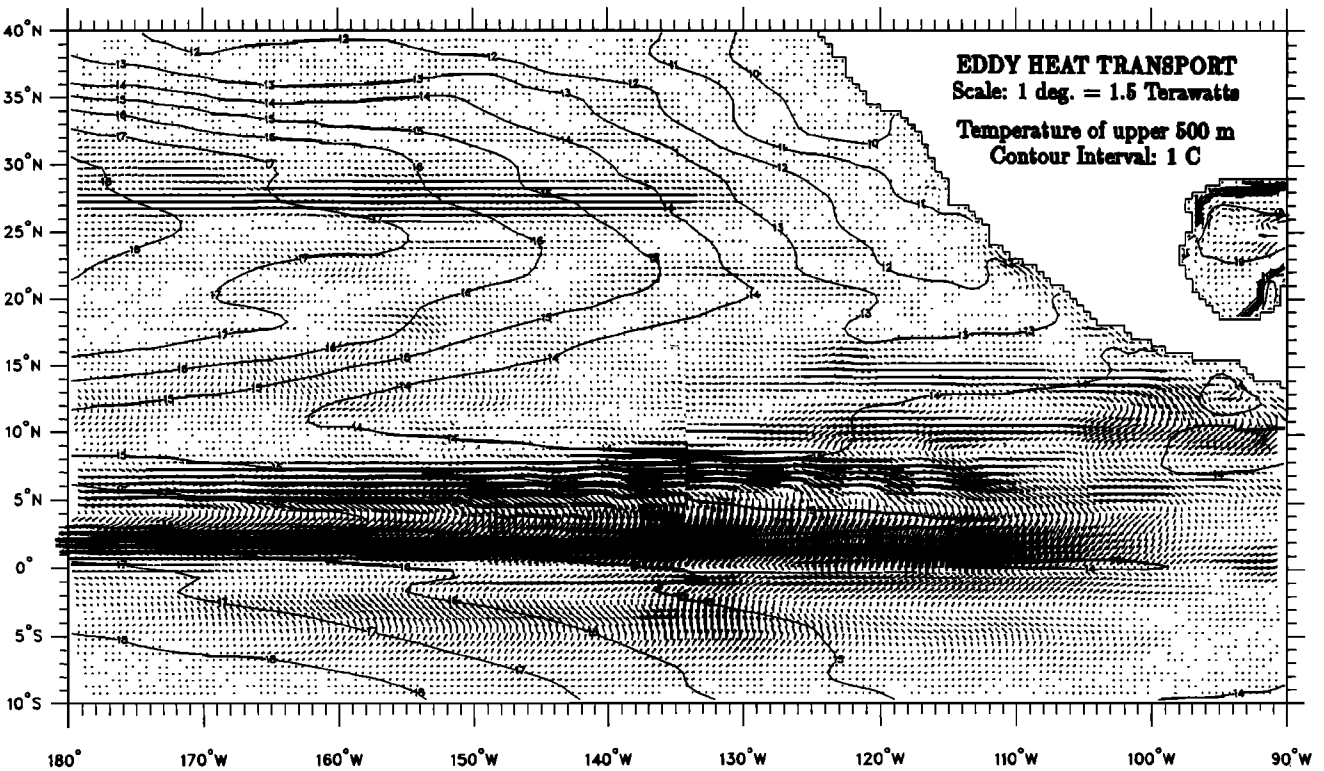

Fig. 30. Vertically integrated eddy transport of heat for the eastern Pacific. A vector of length equal to 1° latitude/longitude spacing represents an eddy heat transport of 1.5 TW. Contour plots of the time mean temperature averaged over the upper 500 m of the water column are also shown. Contour interval is 1°C.

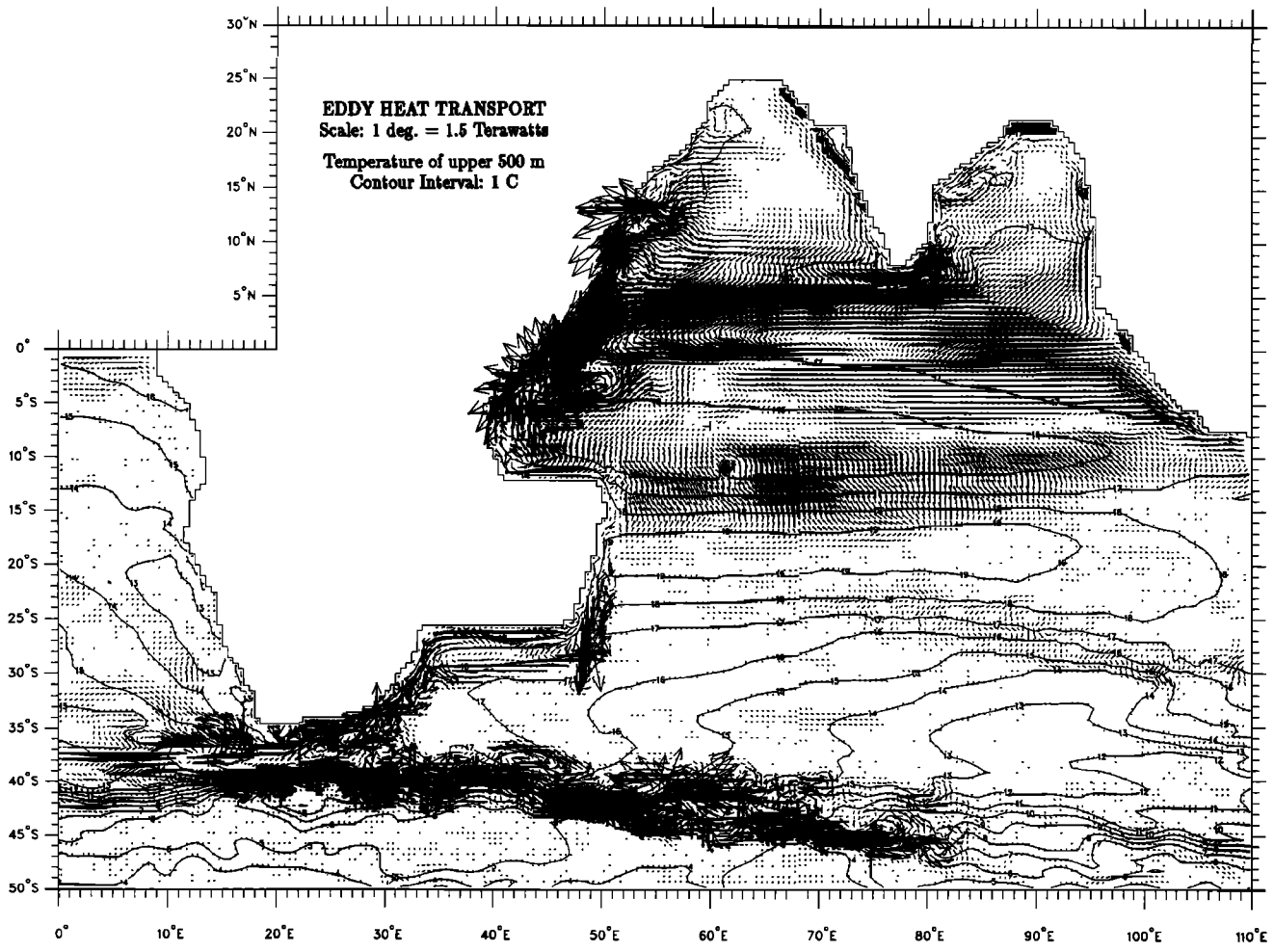

Fig. 31. As in Figure 30, but for the Indian Ocean.

warm core of the NECC and the cold core of the SEC which are primarily down the temperature gradient and related to instabilities. South of the equator in the band 0°–7°S, there are weaker downgradient transports toward the equator. All of these transport are evidently associated with warming the upwelling water on the equator, a portion of which is from the thermohaline conveyor belt circulation described in section 4. It is worth mentioning that these eddy transports are significantly enhanced east of the date line, based on a comparison with plots west of the dateline, which are not shown. West of the date line, a connection to the thermohaline upwelling from the abyssal Pacific is obstructed by deep topography (see Plate 9).

Figure 31 shows the eddy heat transports in the Indian Ocean. There are massive amounts of heat transport by eddies toward the Somali Coast between the equator and 15°N. They are fed from source regions such as the Arabian Sea, the Bay of Bengal, and the area of Indonesian throughflow. Also, a concentrated stream of eddy transport passes south of India near 5°N. Along the equator, transports are eastward on the eastern side of the Indian Ocean; and further south in the range 9°–17°S, they are northward and downgradient into a broad band of cold upwelling water. In the strong currents south of 25°S, such as the Agulhas with its extension and retroflection and the northern branch of the Antarctic Circumpolar Current, there are large transports along the currents as well as away from the current cores. The along-current transports augment those by mean flows alone. The transport away from the current cores may be downgradient on the average; but there are relatively complicated patterns in the vector fields, some of which are against the gradient of temperature. This suggests that the patterns of eddy heat transport in strong currents may not be easily parameterized in coarser-grid models.

Figure 32 shows eddy heat transports in the equatorial and north Atlantic Ocean. The patterns of heat transport toward the equator and toward upwelling zones along the South American coast are evidently downgradient. The retroflection of the North Brazil Current is clearly visible as a seasonal mechanism for transporting heat offshore. The Gulf Stream has a complicated pattern of along-current and cross-current transports, as does the extension of the Gulf Stream in the North Atlantic Current. Finally, weak zonal heat transports at about 31°N appear in the mid-Atlantic which may be similar to those in the eastern Pacific at 26°–29°N (Figure 30); these may indicate marginal instability of mid-ocean flows in these latitudes.

Many of the largest heat transports are organized following the meanders of the time mean isotherms of the current cores. These meanders may become less pronounced in simulations with higher resolution, when a greater range of unstable wavenumbers is allowed. If the meanders persist

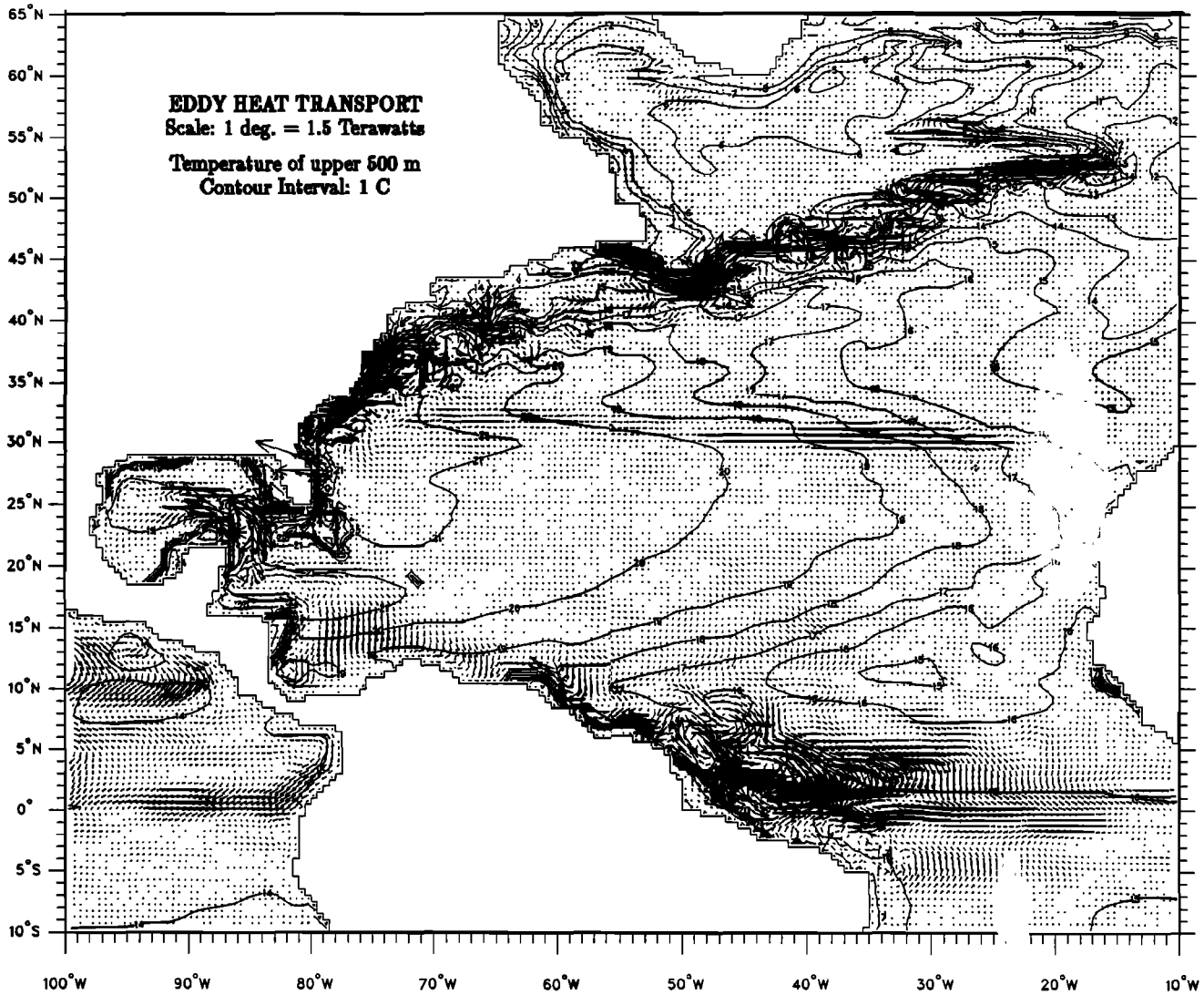

Fig. 32. As in Figure 30, but for the Atlantic Ocean.

with increasing resolution, then they indicate standing waves of an offshore or topographic nature, and their associated heat transports may retain the complex patterns already exhibited in this study. If that should be the case, then it would be difficult to obtain representative eddy transports on a regional-averaged basis from pointwise in situ measurements. The granularity of eddy variability in certain strong-current regions, as recently measured by Geosat height observations, may indicate that standing waves are quite prevalent in current cores.

Our discussion of eddy heat transport does not rule out the possibility that in many part of the ocean, the net heat transport by the total currents may not be as sensitive to the inclusion of eddies as suggested by the present results. A number of previous studies in idealized mid-latitude basins have shown this to be the case [cf. *Bryan*, 1986]. From a climatic point of view, the total heat transport is the dominant quantity of interest. However, from an oceanographic point of view, the eddy heat fluxes are measurable quantities which are directly related to the intrinsic dynamics of the system.

Figure 33, from McCann et al. (1992), shows the meridional heat transports, both by eddies and by the total currents. These are shown for the Atlantic, the Indo-Pacific, and the global ocean. Total transport in the Atlantic is northward between 33°S and 65°N, as required by the conveyor belt mechanism and as confirmed by the observations of *Hastenrath* [1980]. Atlantic eddies transport a small amount of heat southward to warm the conveyor belt as it rises from intermediate depths while crossing the equator to the north. They also weakly transport heat northward in the latitudes of the Gulf Stream. The Indo-Pacific total transport is almost entirely poleward, with an augmentation of southward transport by about 0.5 PW down to the latitude of Cape Agulhas that can feed the conveyor belt in the South Atlantic. Very large equatorward eddy fluxes near the equator are evidently required to warm the equatorial upwelling, which connects to the deep conveyor belt, as described in section 4. Their convergence has the equivalent effect in the model of a surface heat flux of 200 W m^{-2}, which is close to the observational estimate of 240 W m^{-2} made by *Bryden and Brady* [1989]. Submaxima at about 12°N and 14°S are probably due to baroclinic instability in a variety of tropical areas which are identifiable in Figures 30 and 31. Very weak

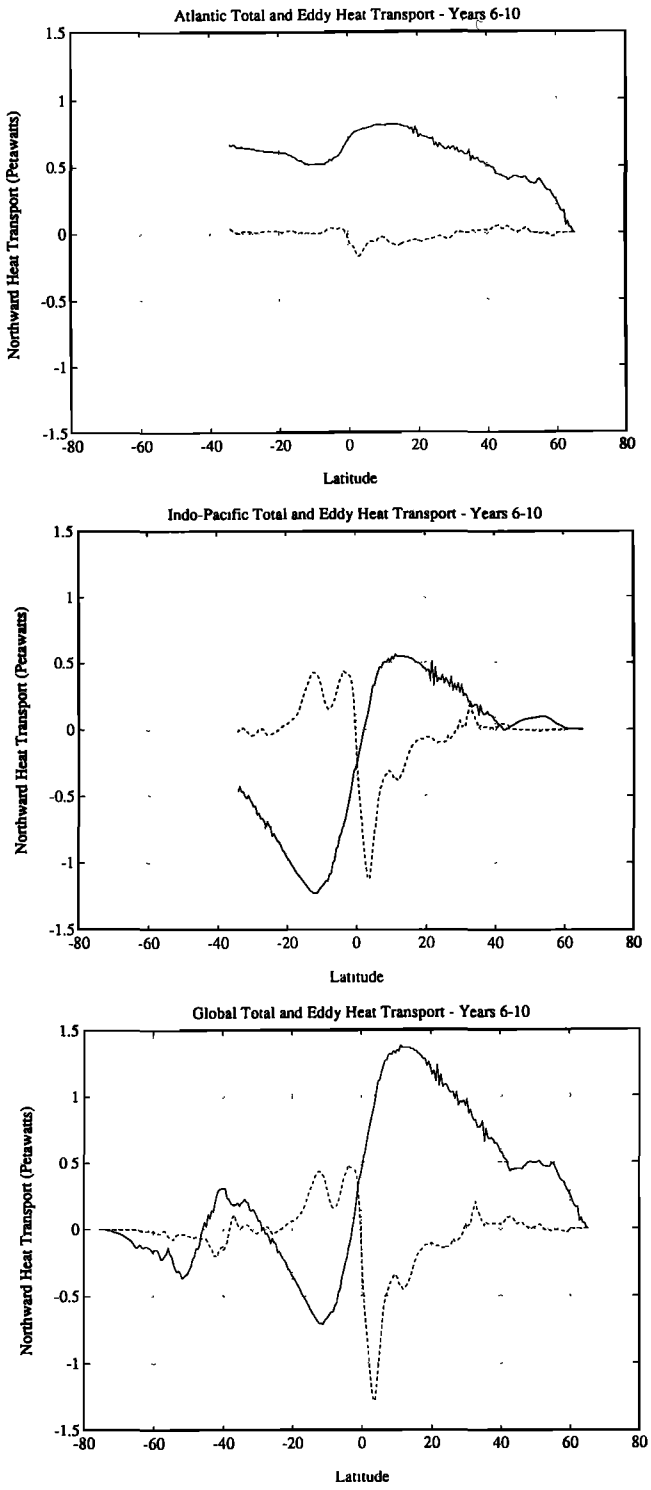

Fig. 33. Meridional heat transports (petawatts) for the Atlantic, Indo-Pacific, and global ocean.

poleward transport exists at the latitude of the Kuroshio. One would expect eddy transports across both the Kuroshio and the Gulf Stream to enlarge considerably as future increases in model resolution allow eddy shedding as observed in nature.

The global heat transport curve shows a peak poleward transport in the northern hemisphere of 1.35 PW at 14°N. The value of 1.1 PW at 24°N is slightly more than half what has been estimated from ocean observations by *Bryden et al.* [1991] for the Pacific and by *Hall and Bryden* [1982] for the Atlantic, and it is slightly below the combined error bars of the measurements. In the southern hemisphere the poleward total transport peaks at 0.7 PW at 12°S and crosses zero at 28°S. Northward transport prevails till 47°S. This behavior is at odds with observational estimates [e.g., *Trenberth*, 1979], and it may be related to insufficient transport of heat poleward by unstable eddies in the ACC, particularly near the Brazil-Malvinas confluence and Agulhas Retroflection regions. This behavior could also be related to insufficient resolution. Previous modeling studies with very coarse resolution [e.g., *Meehl et al.*, [1982] seem to have avoided this problem by virtue of the large explicit diffusion of heat which parameterizes eddy effects in an ad hoc way. The present study may be at an awkward intermediate point between adequately resolved eddies and large explicitly prescribed diffusion.

It is also possible that surface values of temperature and salinity in the southern ocean are very biased toward summertime values, and that the overturning cell which should produce AABW is inhibited, with a consequent reduction in poleward heat transport. Numerical experiments by *England* [1992] suggest the advisability in simulations which employ the Levitus data set for surface forcing of using higher salinity near Antarctica, in order to produce more realistic overturning. That should also increase poleward heat transport. It should increase surface heat losses as well.

7. Haline Dynamics

From both oceanographic and climatic points of view, it is important not to neglect the role of salt and the cycle of fresh water in the global ocean. This section provides a treatment for haline processes which is comparable in scope to that of the previous section for thermodynamics.

Figure 34 shows the salinity at 37.5 m in the tropical Pacific, for early October in year 10 (Figure 34*a*) as well as averaged for years 6–10 of the seasonally forced run (Figure 34*b*). This gives a clear indication of the 800- to 1000-km waves near the equator, whose corresponding velocity and temperature fields were shown in Plate 2 and Figure 23, respectively. Highly nonlinear waves are evident between the date line and 110°W. These mix salt northward across a salinity front which is quite prominent in the upper few hundred meters, as can be seen in Figure 5. Judging from the smoothness of the 5-year average field, the instantaneous field has eddy variability throughout the tropical Pacific. Quite a few waves in several different areas have pronounced cusps or appear to have broken recently into fragments. This process of turbulent mixing of salt is captured by the videotape animations as well. The entire process of wave breaking seems rather well represented in these tropical latitudes by the ocean model.

Figure 35 shows the 5-year mean salinity in the upper 50 m of the water column. As was the case for temperature in Figure 25, the upper half of this depth range has strong (30 day) restoring to Levitus data as a proxy for surface water flux, but the lower half is fully prognostic. The expectation is that something representative of 0- to 50-m salinity in the real ocean is obtained this way. The figure shows subtropical maxima in all ocean basins. The low salinity of the North Pacific is evident, particularly north of the subarctic front, as

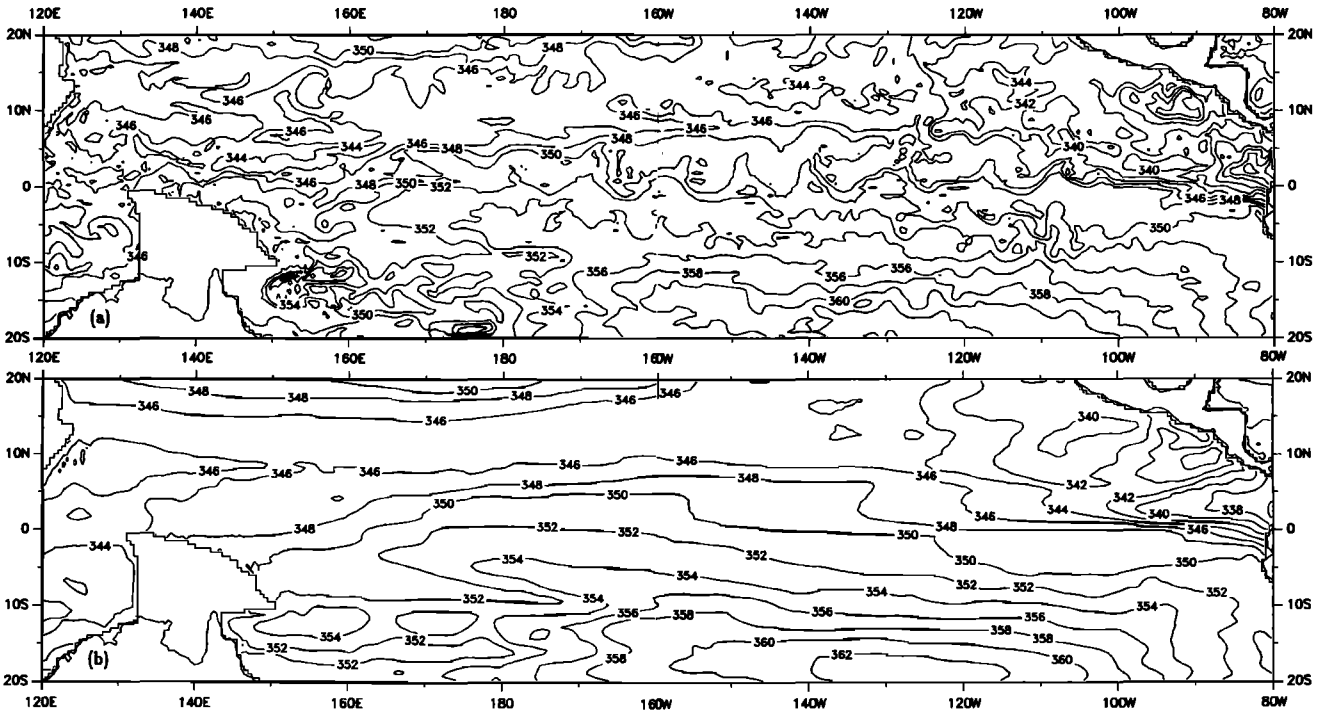

Fig. 34. Simulated (*a*) instantaneous and (*b*) 5-year average salinities in the tropical Pacific at 37.5-m depth (model level 2). The instantaneous field is for early October in year 10 of the seasonally forced extension run, and the smooth field is averaged for years 6–10. Contour interval is 0.2 ppt.

is the low salinity of the Labrador Current and of the region north of the Gulf Stream. Low salinities related to runoff are found in the Bay of Bengal and in the tropical Atlantic where the North Brazil Current advects Amazon River discharge. In the extreme eastern equatorial Atlantic and Pacific, equatorial upwelling produces low salinities.

Indonesian throughflow should be noticeable in salinity fields, as suggested by *Gordon* [1986]. This should be particularly evident in the depth range 0–500 m, where the known inflow is concentrated (M. Fieux et al., unpublished manuscript, 1992). To verify this, Figure 36 shows the 5-year mean salinity, the Levitus salinity, and the difference of the two for the depth range 100–250 m. The agreement between prognostic model salinity and observations is within about 0.2 ppt as the salinity tongue crosses the entire Indian Ocean from the area of the Pacific inflow to Madagascar.

Figure 37 shows the 5-year standard deviation of surface salinity. This is comparable to Figure 25 for surface temperature deviation, in that it should show a combination of seasonal and mesoscale effects. Because there may be much

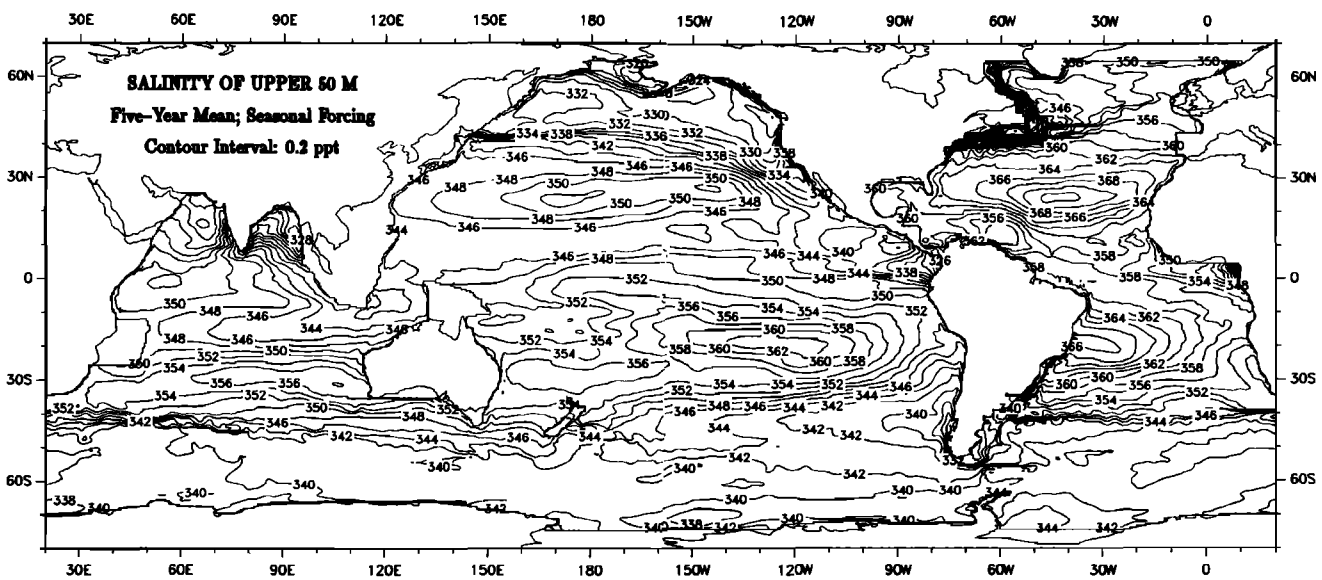

Fig. 35. Five-year average of salinity in depth range 0–50 m. Contour interval is 0.2 ppt.

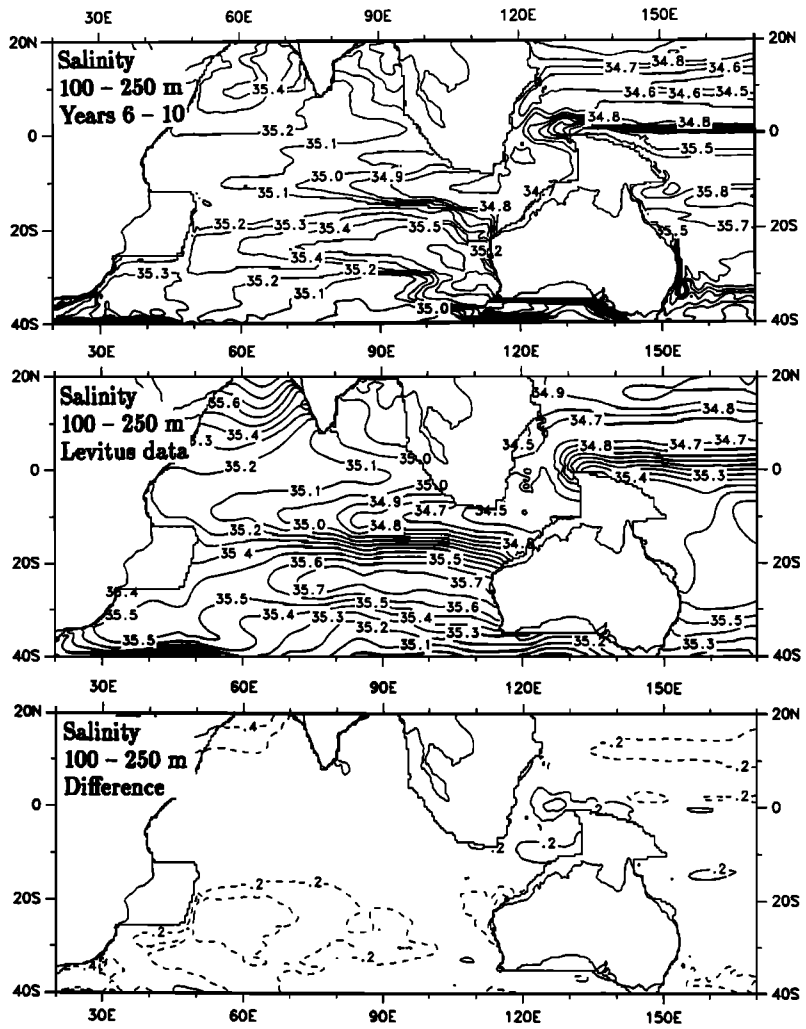

Fig. 36. (Top) Simulated salinity in the depth range 100–250 m in the Indian Ocean, (middle) observed 100- to 250-m salinity from *Levitus* [1982], and (bottom) the difference of the two fields. Contour intervals are 0.1, 0.1, and 0.2 ppt.

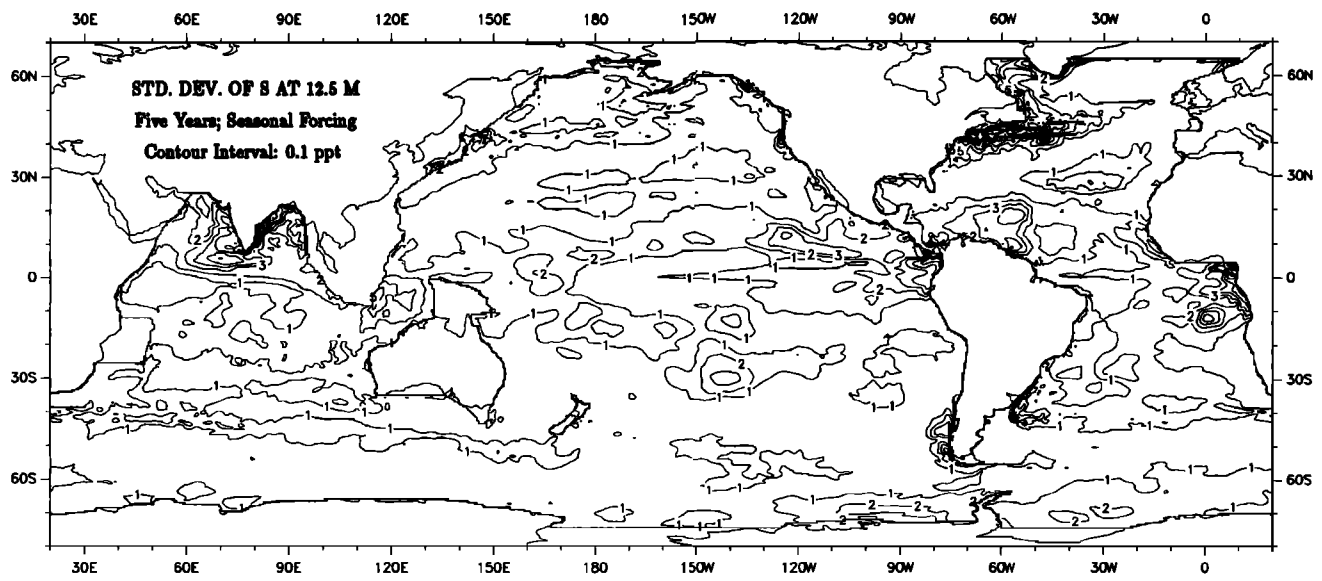

Fig. 37. Standard deviation of surface salinity for 5 years. Contour interval is 0.1 ppt.

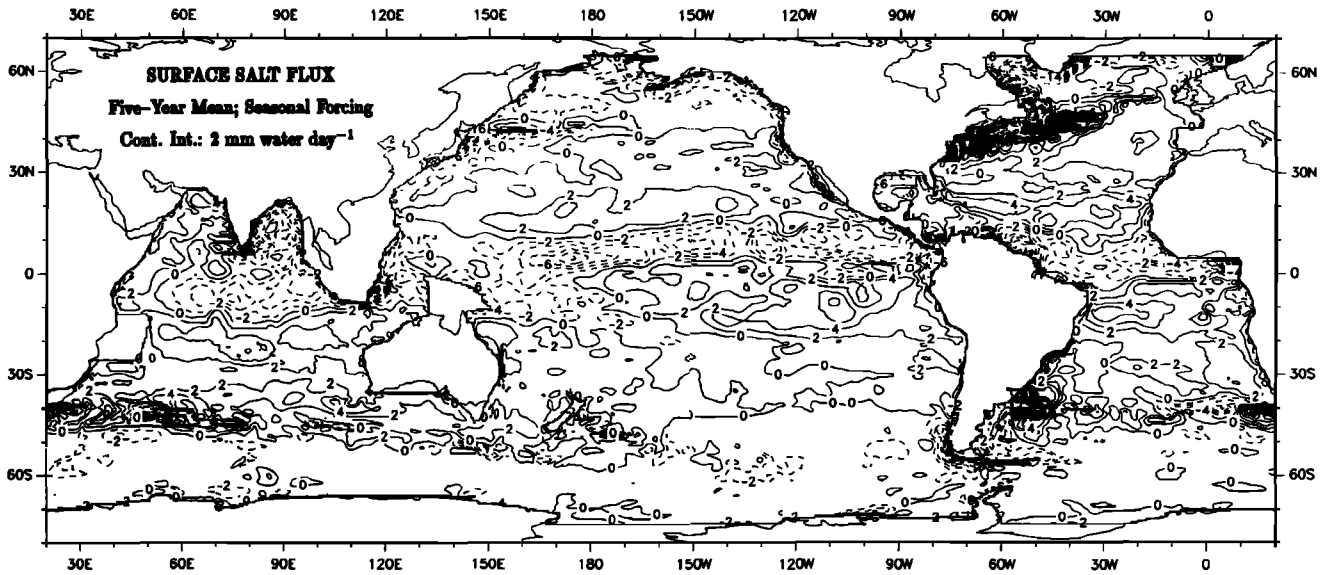

Fig. 38. Surface salt flux for years 6–10 of the seasonal case. Contour interval is in equivalent water flux units of 2 mm d^{-1}.

less of a seasonal cycle in the prescribed forcing of salt as opposed to heat, this field appears to show mainly eddy variability in areas where salinity gradients are particularly strong, such as the areas already mentioned above. In addition, there are interesting local maxima in the subtropical eastern Atlantic, near the Angola Dome in the South Atlantic, near 120°W in the tropical Pacific, in the middle South Pacific, in the Brazil-Malvinas confluence, and finally off the southwest tip of South America.

Figure 38 shows the surface boundary flux for salinity, in water flux units of millimeters per day, for the average of a 5-year period. The use of the simple "Haney boundary condition" [*Haney*, 1971] on salt produces a fairly realistic distribution for the combined effects of precipitation in tropical convergence zones and runoff from tropical rivers. The general pattern of mid-latitude evaporation and high-latitude precipitation is reproduced as well. In the North Atlantic, the excess of evaporation over precipitation is shown to be large; in fact, a net flux of 0.26 Sv from the Atlantic north of 15°N is found in the model (McCann et al., 1992). Some frontal regions show that alternating-sign unmixing of Levitus smooth data is occurring, but there are more systematic losses of water from warm currents in high latitudes. This latter phenomenon would explain the large fluxes in the Gulf Stream and in the Agulhas Current and Retroflection.

Figure 39 shows the vertically integrated effect of all subsurface robust diagnostic forcing terms on salinity. The same contour interval is used as for Figure 38, and the zero line is omitted. Diagnostic restoring to observed salinity is quite small over almost all of the ocean. The largest positive signal corresponds to the missing Mediterranean outflow,

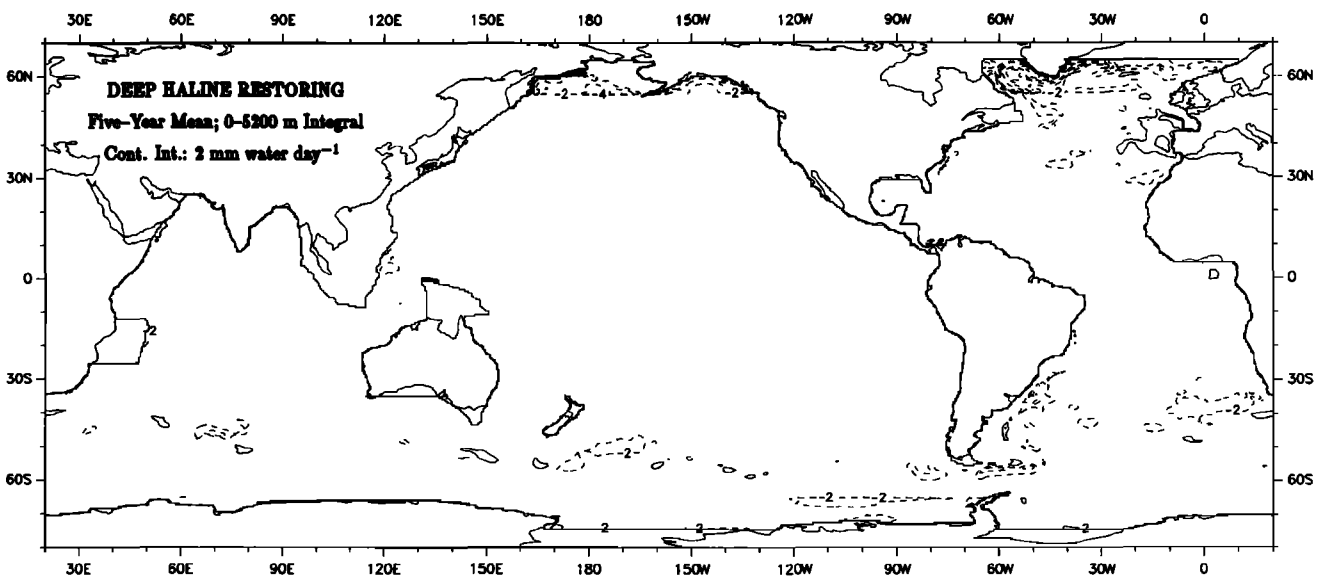

Fig. 39. Deep salt flux for years 6–10 of the seasonal case. Contour interval is in equivalent water flux units of 2 mm d^{-1}.

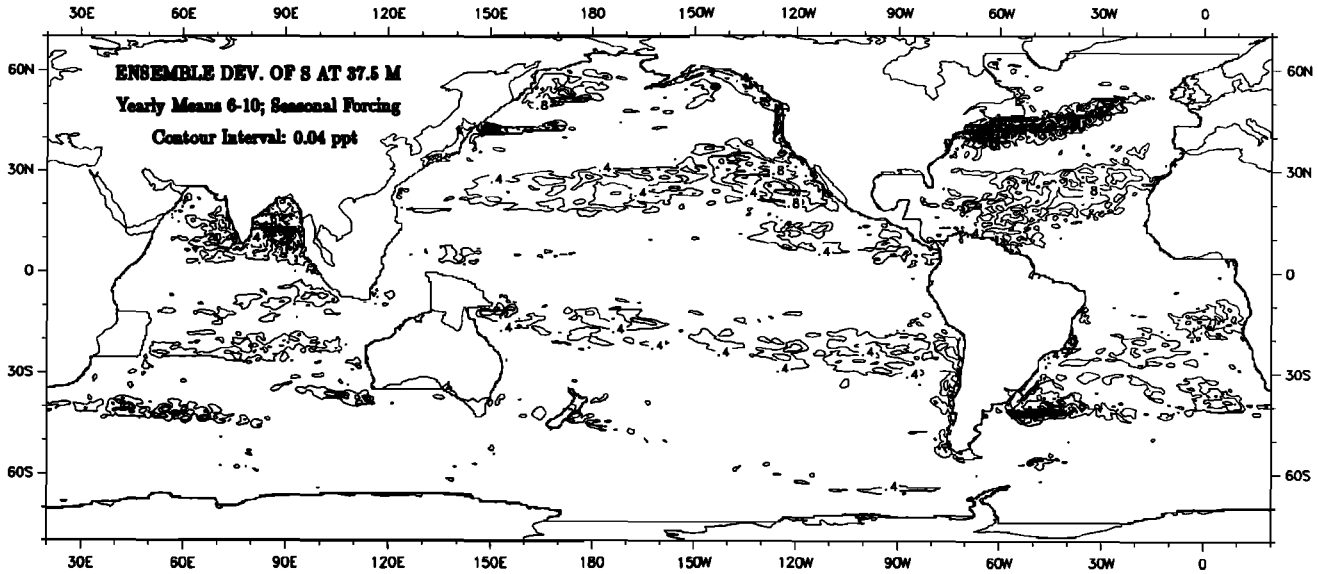

Fig. 40. Ensemble standard deviation of annual average salinity at 37.5 m. Contour interval is 0.04 ppt.

and the largest negative one to the missing East Greenland Current and flow from the Arctic. Lacking these marginal seas, the model puts some of the missing effects back in through the robust diagnostic terms. Otherwise, the amount of diagnostic restoring required by this high-resolution model is quite minimal.

Figures 40 and 41 are provided to characterize the intrinsic eddy effects on near-surface salinity. They are similar to Figures 28 and 29 for temperature, but they detect variability in those areas where large-scale salinity gradients exist in the time mean flow. Figure 40 is the standard deviation of five yearly averages of salinity at 37.5 m (model level 2) in the seasonally forced run, whereas Figure 41 is the 900-day standard deviation of 37.5-m salinity in the run with annual mean forcing. As was the case for temperature, the first variability field shows a lot of sampling noise superimposed on the regional patterns, and it misses intrinsic variability of some high-frequency phenomena in the tropical waveguides. Nevertheless, both figures give insight into what regions of the global ocean manifest intrinsic mesoscale variability, as seen in the salinity field. Interesting areas of agreement between the two fields are the Gulf Stream region, the subtropical North Atlantic, the offshore part of the California Current system, the Subarctic Front of the North Pacific, the Bay of Bengal–Eastern Arabian Sea, the Agulhas Extension and Retroflection, the 20°–25°S belt in the Indian Ocean, the Brazil-Malvinas confluence, a region southwest of New Zealand, and the 20°–25°S belt of the eastern Pacific. Not all of these areas of mesoscale variability may have been identified yet in observational data sets.

Figures 42–44 depict eddy salt transports, with components $\langle u'S' \rangle$ and $\langle v'S' \rangle$, for the final 5 years of the seasonally forced simulation. The figures are similar to those in section 6 for the corresponding transports of heat. Here,

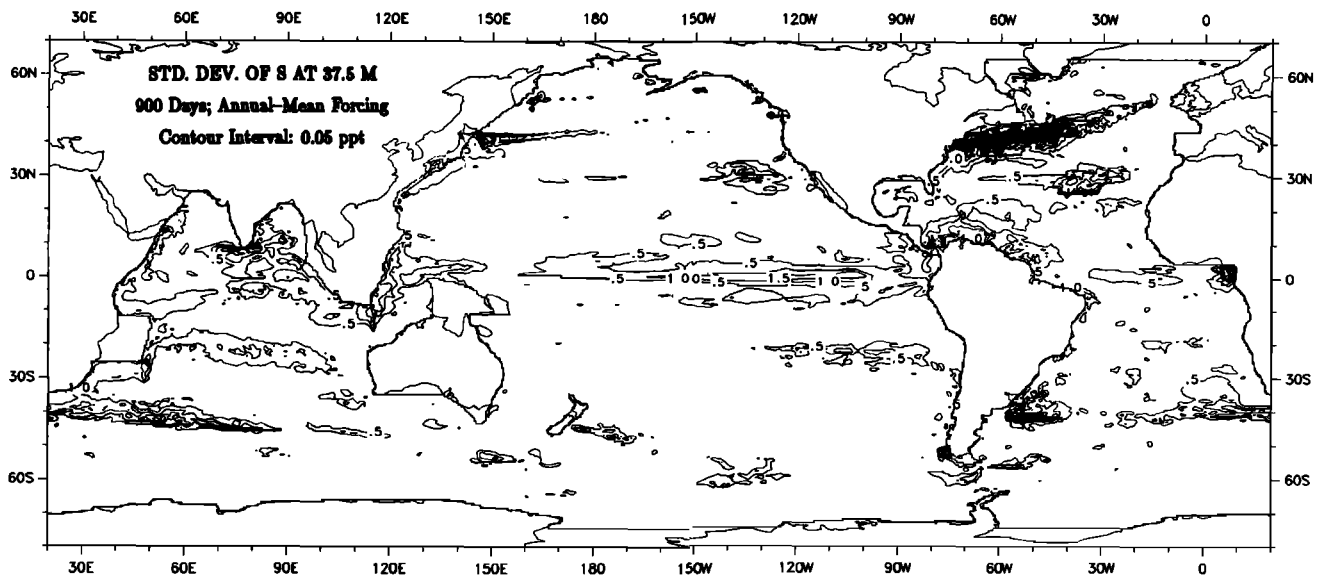

Fig. 41. Standard deviation of 37.5-m salinity for annual mean forcing. Contour interval is 0.05 ppt.

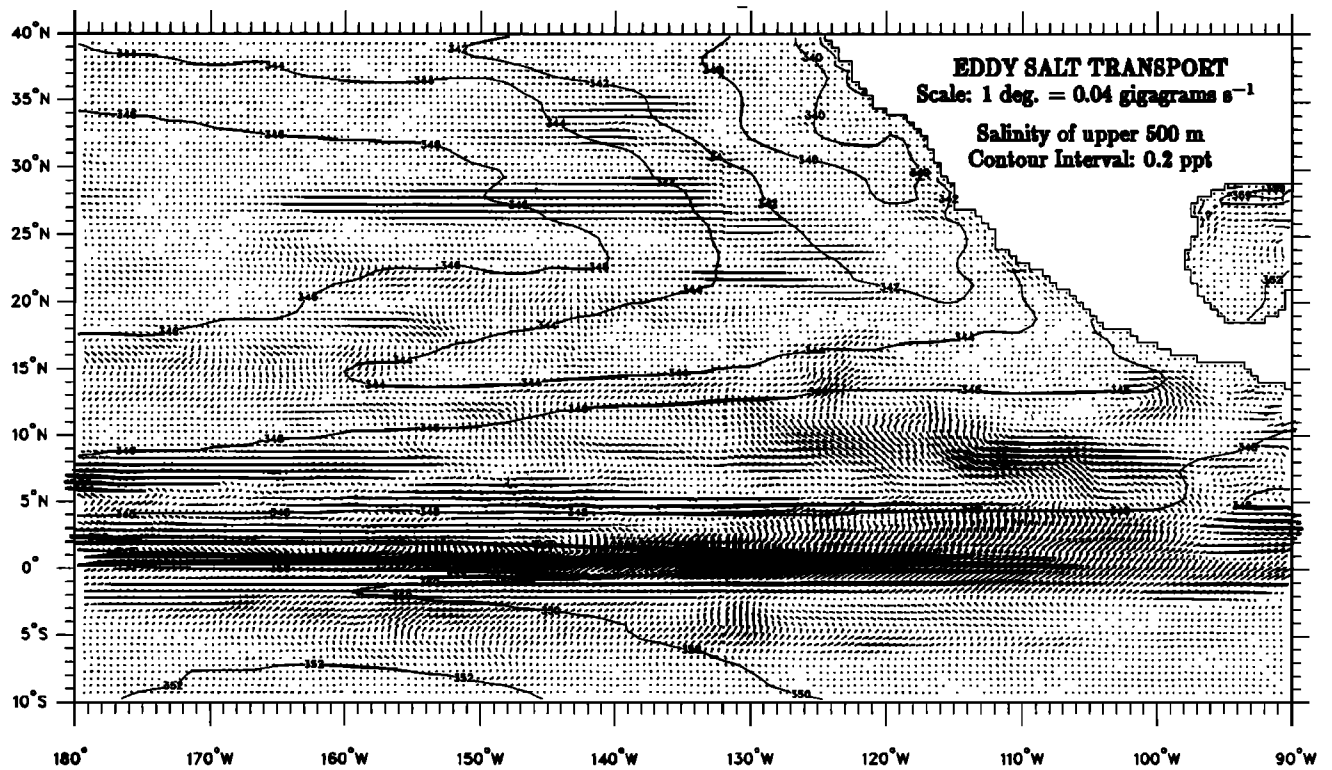

Fig. 42. Vertically integrated eddy transport of salt for the Eastern Pacific. A vector of length equal to 1° latitude/longitude spacing represents an eddy heat transport of 0.04 Gg s^{-1}. Contour plots of the time mean salinity averaged over the upper 500 m of the water column are also shown. Contour interval is 0.2 ppt.

isolines of average salinity in the upper 500 m of the water column are superposed on the vector fluxes.

Figure 42 for the eastern Pacific depicts an organized large-scale eddy transport of salt across the equator into the North Pacific. This is confined relatively near the equator in the longitude range from the date line to 140°W. East of 140°W, northward transports of salt by eddies are evident in broad zones extending to 15°N. Some transports near 90°W are converging on a low-salinity region in the Gulf of Panama (as can better be seen in Figure 44). Almost all of these transports appear to be downgradient.

Figure 43 for the Indian Ocean shows massive amounts of eddy salt transport into the relatively fresh Bay of Bengal. These are concentrated in a zonal band south of India and near the equator in the eastern ocean. Salt transports by eddies are away from the Arabian Sea and also down the Somali Coast. Almost all of these transports are downgradient as well. The region of the Agulhas Retroflection as joined to the northern branch of the ACC has transports with significant along-stream as well as across-stream components. These are clearly organized following the meanders of the time-averaged current cores. Finally, a northwestward eddy transport of salt from the Agulhas Extension feeds into the South Atlantic, in a similar fashion to that for eddy heat transport, as can be seen in Figure 31.

Figure 44 shows eddy salt transports of the North Atlantic. Strong eastward transports near the equator appear to originate in a tightly retroflected branch of the North Brazil Current. Salt transports converge around the perimeter of an offshore area which is fed by discharges from the Amazon River (as specified in the surface salinity forcing). Further north, salt transports cross a weak front at the boundary of the subtropical water which is significantly influenced by evaporation and Mediterranean outflow. The Gulf Stream and its extension into the North Atlantic Current have complicated transport patterns similar to those of Figure 43 for the region of the Agulhas Retroflection. As was remarked in the preceding section in regard to heat transports, these effects may be hard to parameterize in coarse-grid models. As also mentioned earlier, if the standing-wave patterns are indicative of real ocean behavior, then it will be difficult to obtain representative regional estimates of eddy transports from pointwise in situ observations.

Figure 45, from McCann et al. (1992), shows salt transports by mean flows and eddies in the Atlantic, Indo-Pacific, and the global ocean. The salt transports in the present rigid-lid model can be converted to equivalent freshwater transports by dividing by a factor of -0.035. The results compare fairly closely to the freshwater flux deduced from the atmospheric water cycle by *Wijffels et al.* [1992]. Further discussion is given by McCann et al. (1992). Considering that the model calculations of transports use ocean surface salinity with the relatively simple *Haney* [1971] boundary condition, these are only approximate estimates. However, many sources of error also exist in the observational estimation of evaporation, precipitation, and runoff; and a relatively close agreement between the two methods is encouraging.

On a final note, the eddy salt transport is maximal in the Pacific near the equator. The salt transport by this mechanism is clearly illustrated in the video animation of the frontal structure in the equatorial Pacific, and also visible in Figure 34. Eddy salt transports in higher latitudes are

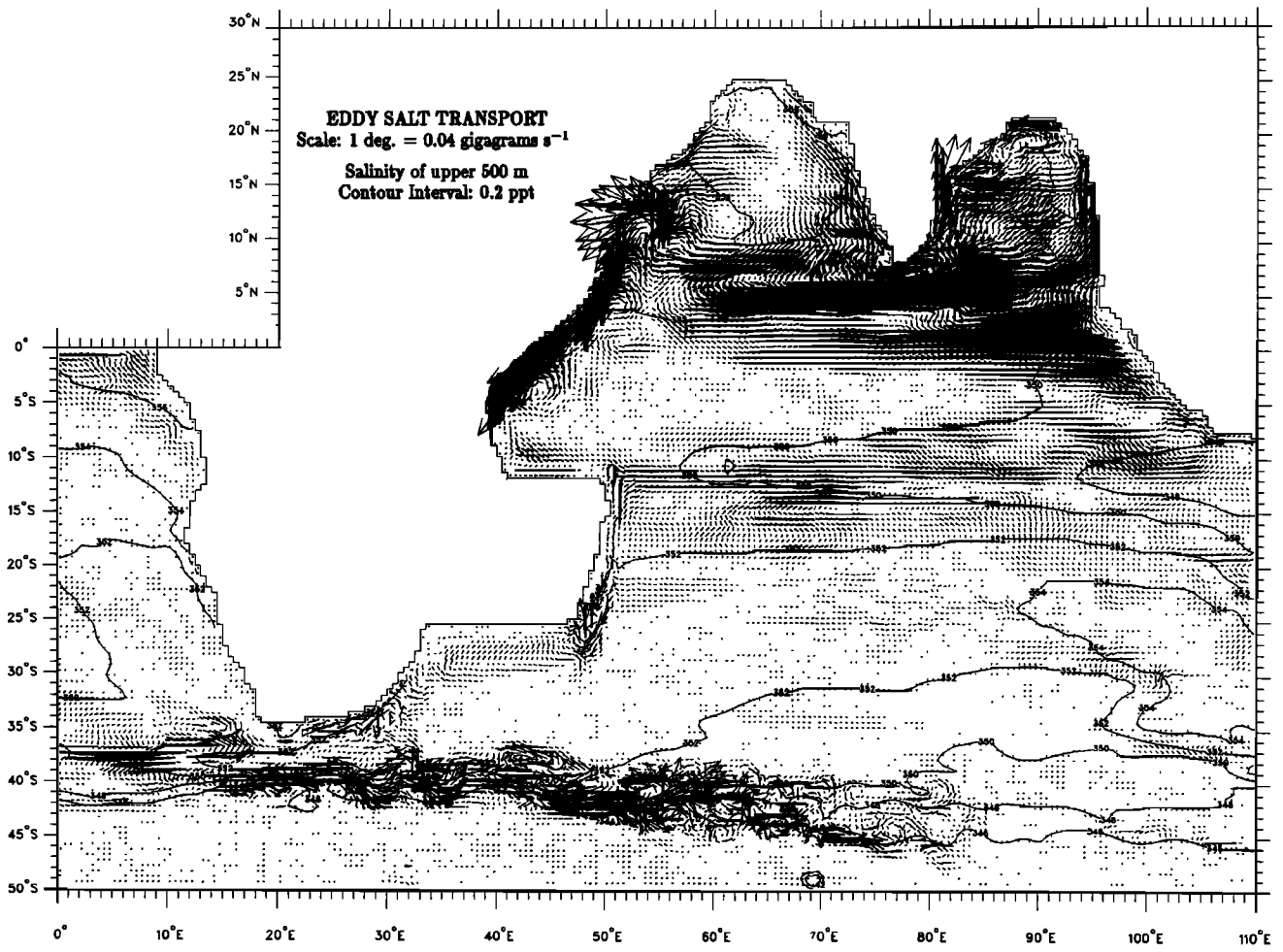

Fig. 43. As in Figure 42, but for the Indian Ocean.

probably underestimated because of the marginal resolution in the present experiment.

8. Conclusions

The preceding sections have described results from a high-resolution model that uses known bathymetry, observed ship winds, and the historical archive of temperature and salinity to simulate the global ocean circulation of the present day. After due account for the weak restoring below 710 m to observed temperature and salinity and the substitution of pseudofluxes for surface heat and moisture fluxes, the results are basically unconstrained, in that information in the thermocline range 25–710 m outside of polar latitudes has established itself freely over a simulated period of more than 20 years. Certain features of the deep circulation have clearly established themselves as well, notably the deep thermohaline circulation and the deep Antarctic Circumpolar Current. Since no changes of model geometry, forcing functions, or diffusion coefficients were made except in the course of including new physical processes, any conclusions that emerge are basically untuned and come from first principles. The conclusions are as follows.

1. In the mid-latitudes, gyre circulations have relatively simple Sverdrup interiors in the time mean, except where interbasin connectivity is involved, such as the Tasman Front, the Indonesian throughflow, and the Atlantic crossflow at 30°S. (The crossflow is somewhat north of the southern tip of Africa by virtue of vorticity advection from the Indian Ocean.) Western boundary currents are unstable to varying degrees, especially after separation from the coast (as in the Gulf Stream, Kuroshio, and Brazil currents) or in areas where a break in coastline occurs (Gulf of Mexico, Tasman Sea, Agulhas region). Some weak interior instabilities exist as well, whose locations are relatively consistent with recent Geosat observations. However, mid-latitude instabilities are not as strong in the model as in the observations, and grid sizes smaller than the local radius of deformation will be needed to improve the simulation of eddy effects.

2. Equatorial currents are strong, zonal, and usually unstable. Many aspects of near-surface tropical circulation have been quantified, including relationships to circulations outside the tropics. Seasonal countercurrents and low-latitude western boundary currents are also quite unstable. Well-resolved tropical phenomena include the well-known mid-ocean 30-day waves and western ocean variability in the 40- to 50-day range.

3. In high southern latitudes the Antarctic Circumpolar Current is strong, vertically coherent, and highly filamented by topography. It has complicated instability patterns related to bottom topography along its path, and these agree well (in location if not in magnitude) with very recent Geosat

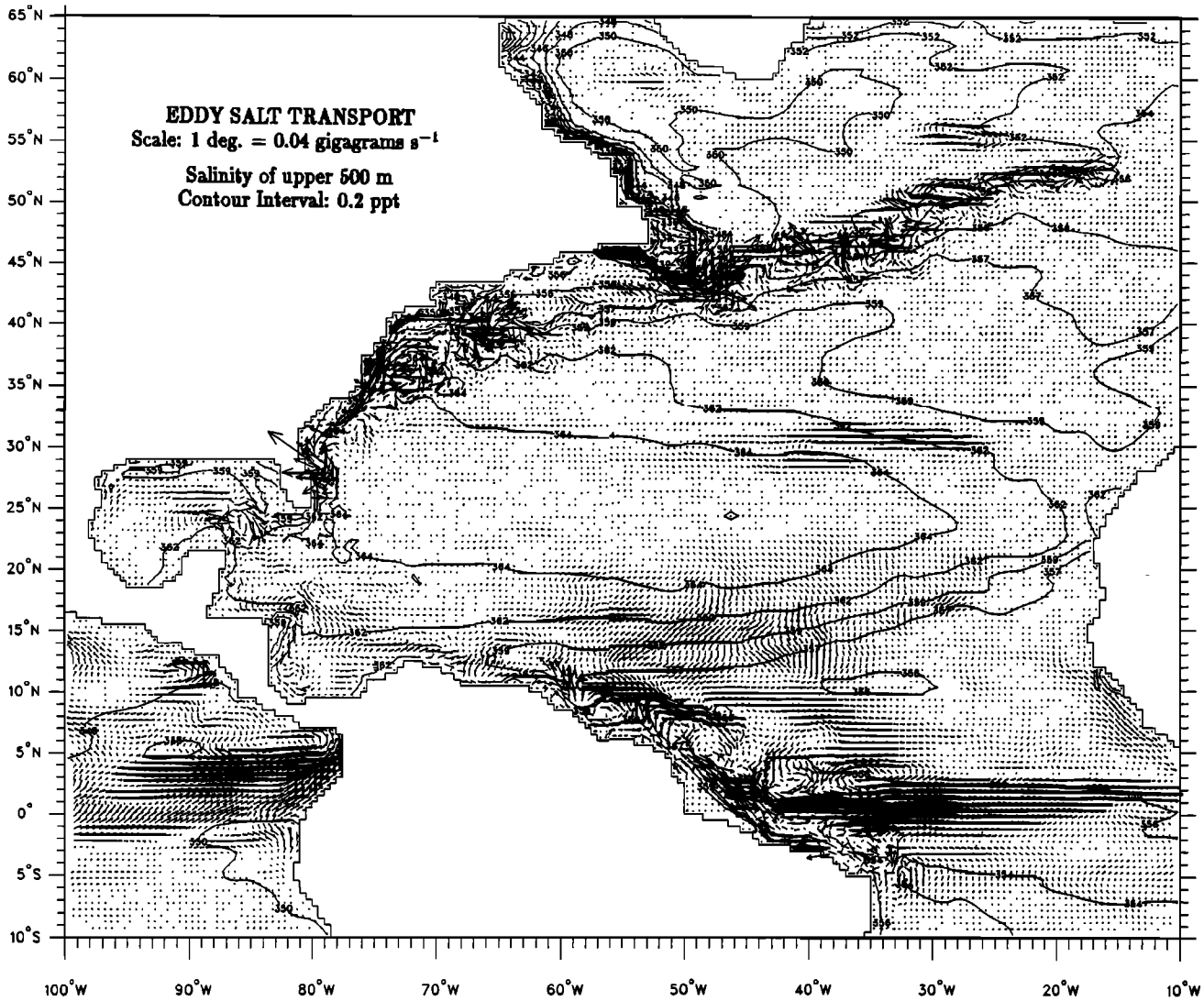

Fig. 44. As in Figure 42, but for the Atlantic Ocean.

observations. Baroclinic instability and the negative viscosity effect help to maintain the mean flow in some parts of the current. Strong interactions with mid-latitude gyre circulations occur in the South Atlantic and South Indian oceans.

4. In high northern latitudes, subpolar gyres exhibit considerable variability, e.g., in the Labrador Sea, North Atlantic Drift, Pacific Subarctic Front, and Bering Sea. This variability is somewhat intensified when seasonal forcing is involved.

5. On a global basis, a three-dimensional global thermohaline circulation stands out, with eddy-rich surface flow from the Pacific through the subtropical Indian Ocean to the Atlantic associated with combined driving by heat and moisture fluxes. The deep compensation by North Atlantic Deep Water is in western boundary undercurrents connected through the South Indian Ocean by the ACC. The conveyor belt circulation preferentially rises at the equator in equatorial jets which are known to have observational counterparts in the deep Pacific. The upper part of the thermohaline circulation rounds Australia to the north through the Indonesian passage and to a lesser extent to the south through the Tasman Sea and along the southern coast of Australia. Transport estimates of the order of 10–15 Sv are found at many key points along the primary path of this mean circulation.

6. Additional exchanges occur among many flows in different ocean basins. The deep southward flow in the South Pacific accelerates eastward into the ACC, passes through the Drake Passage, and upwells in the South Atlantic as a significant cold water route back to the North Atlantic. The ACC and the conveyor belt circulations interact at depth by being coincident between the South Atlantic and the South Pacific and at the surface along the retroflected Agulhas Current across much of the South Indian Ocean. Interconnection can be applied in terms of mechanisms as well, since it is likely that each of the ACC and conveyor belt circulations has both wind-driven and thermohaline aspects to its maintenance.

7. The seasonal cycle of ocean currents appears quite linear, in that annual mean currents in a seasonally forced case differ little from those with annual mean forcing, except in low-latitude western boundary currents. However, seasonal forcing greatly enhances the variability of the transport stream function in all latitudes. Sea slope variability is

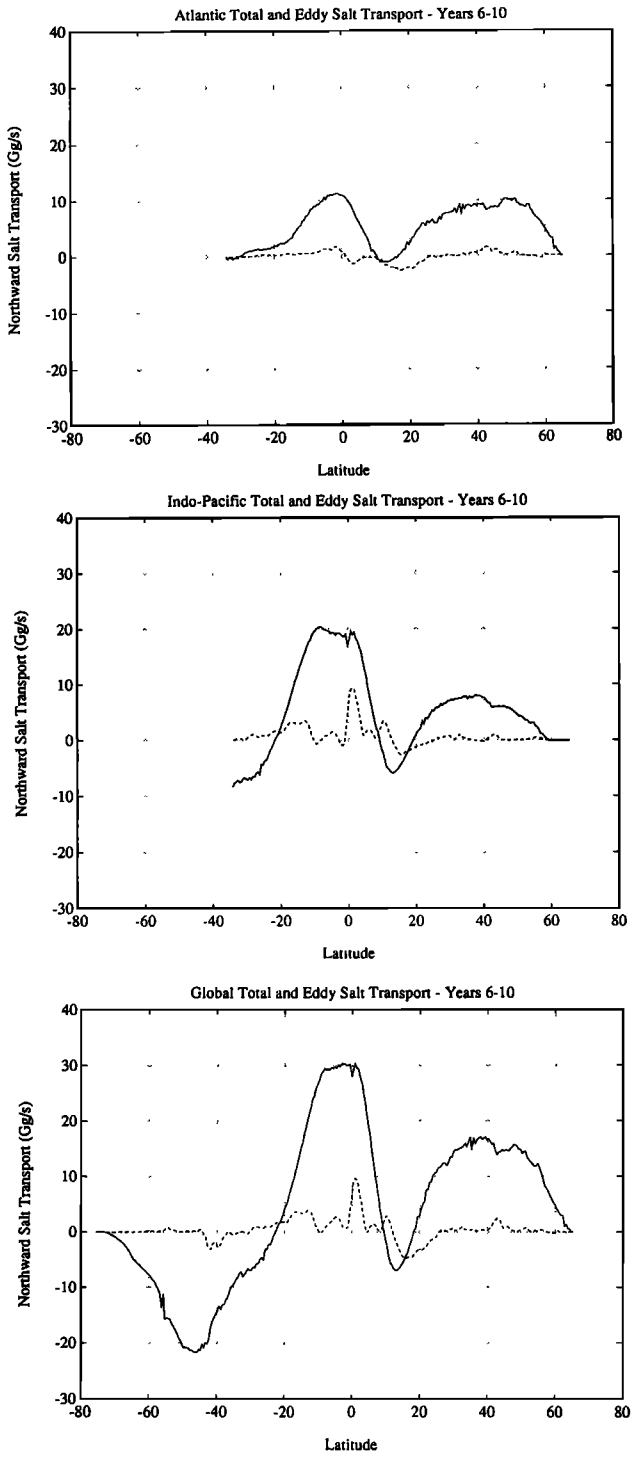

Fig. 45. Meridional salt transports (gigagrams per second) for the Atlantic, Indo-Pacific, and global ocean.

enhanced in certain seasonal current systems, producing improved agreement with Geosat measurements. Variability is strongly influenced by topography. The global variability fields of the model provides an excellent baseline for making comparisons with other observational datasets and with higher-resolution model output.

8. Regarding the overall thermodynamic effect of eddies, they can be very large locally (several terawatts). However, the heat transport are not large in the zonally averaged sense, except in the tropics and (to a lesser extent) in the latitude belt of 40°–50°S. Eddy transports in the tropical Pacific similar to those observed are instrumental in warming the rising water of the conveyor belt. The heat transport by eddies in the ACC may be underestimated owing to insufficient resolution in high latitudes. Also, the patterns of heat transport by eddies, not only in the ACC but also in mid-latitude ocean jets, are complex and may be difficult to parameterize. (However, in some oceanic areas, the net transport of the total currents may be climatologically controlled and therefore not as sensitive to parameterization as the present results suggest.)

9. Salt transports in the model give an estimate of the oceanic contribution to the global water budget. Total salt transports are toward the tropical atmospheric convergence zones and away from mid-latitude evaporation belts. Eddy effects are largest near the equator in the Pacific, where they act to remedy the large-scale imbalance in surface hydrological forcing between the North Pacific and the North Atlantic.

The preceding conclusions have emphasized the physical aspects of the model results. The following conclusions relate somewhat more to modeling considerations, and in particular to which aspects of the formulation worked well and which may need improvement.

10. Overall, the representation of global ocean circulation with 0.5° grid size and biharmonic mixing is reasonably good. Nevertheless, modeling the instabilities of midlatitude western boundary currents and those of the Antarctic Circumpolar Current will require improved resolution. The outlook for improved simulations at 0.25° grid size is optimistic.

11. Laplacian closure shows broad quasi-steady flows in certain regions where time mean flows with biharmonic friction are narrow and strong. This is true even with the smallest allowable Laplacian friction for the 0.5° grid size. Some negative viscosity effects of eddies may require proper parameterization in major strong currents. Also the more scale-selective biharmonic viscosity may simply allow higher-velocity cores in some currents.

12. Surface *Levitus* [1982] values in the southern ocean may have a bias which adversely affects the surface heat and salt balances there. More importantly, the production of Antarctic Bottom Water may be seriously affected.

13. Walling off the Arctic Ocean causes problems which the robust diagnostic forcing cannot completely remedy. The effect of the Arctic Ocean and its marginal seas on the production of North Atlantic Deep Water, as well as on the separation of the Gulf Stream, should be investigated by adding the Arctic domain to the model.

14. Convection and other high-latitude processes seem poorly treated, even with a seasonal cycle of forcing. More effective treatments of these processes will be required in the future. To examine present-day ocean circulation, diagnostic forcing can be employed to augment convective adjustment and maintain deep and bottom waters of the North Atlantic and the southern ocean.

9. PLANS

A number of physical and numerical improvements in the model have been suggested by model results and by other considerations. In the former category, inclusion of the

Arctic Ocean and better parameterization of convection have been noted. In the latter category, the inclusion of sea ice, with both thermodynamics and dynamics of ice, is desirable. An earlier coupled model which could be adapted for handling both the Arctic Ocean and sea ice is that of *Semtner* [1987]. A new treatment of sea ice by *Flato and Hibler* [1992] would improve the computational efficiency of the sea ice component. Also, the treatment of the oceanic barotropic mode by the free-surface method of *Killworth et al.* [1991] will reduce computer requirements significantly with grid sizes smaller than 0.5° and it will improve the physics of the simulation. Very realistic geometry with many islands is easily handled with this method. Finally, additional physical improvements in near-surface mixing and cross-isopycnal mixing would be advisable.

One simple change in the model is to leave out the deep diagnostic forcing terms during extension runs of the earlier integration. This is already being done, and the results are being monitored closely to determine effects on the conveyor belt circulation. Enhanced buoyancy forcing of southern ocean circulation should also be investigated. Prognostic integrations make sense as more physical processes in the high latitudes are added to the model. Additional studies on the interconnectedness of the conveyor belt circulation and the ACC, and their response to changes in wind and buoyance forcing, are also desirable.

The present study is obviously limited by computer power, as it affects the spatial resolution and time span of an experiment. A prototype 0.25° version of the global model exists and runs efficiently on the eight-processor Cray Y-MP at NCAR. Following physical and numerical improvements as discussed above, the model could be spun up with 0.25° spacing on the Y-MP and subsequently moved onto more powerful supercomputers of the near future. As designed by *Chervin and Semtner* [1990], the model can use all available processors of parallel vector machines, in order to maximize scientific output on each machine. The model is already formulated to allow enhanced resolution in high latitudes as an option, and the latitudinal grid spacing in kilometers could be made the same as the longitudinal spacing. Such an approach would improve the treatment of eddies without requiring a reduction in time step. Looking ahead to the not-too-distant future, adaptation of the model to massively parallel computers will allow multicentury integrations with grid spacing as fine as 0.125° and up to 100 vertical levels.

10. Remarks

The primary output of the present study has been an estimate of ocean circulation statistics, including the effects of eddies, on a global basis. This estimation has not been done before with a model. Most oceanographers would concur that observations have yet to produce such a complete estimate. Certainly, many quantitative observational results have only recently been obtained and often have required the use of satellites. In fact, the present model results would have much less data to be tested against without Geosat measurements of global height variability, recent in situ measurements of deep equatorial jets, and new hydrographic sections of Indonesian throughflow.

It would appear that ocean modeling is finally coming of age. As indicated by this study as well as by the CME and FRAM studies, it is now possible to model ocean circulation in realistic geometries with observed forcing, to validate the models against available (and often relatively recent) field observations, and to make predictions of future findings that may prove the models right or wrong. Progress can be made in this way. Scientific progress was difficult to make in the past, when ocean models usually were formulated either for the wrong domain with the right parameters or for the right domain with the wrong parameters.

Ocean modeling still has a long way to go. Geosat observations have confirmed what has long been suspected: that the local radius of deformation is a fundamental length scale for ocean dynamics, and that models should resolve disturbances of this scale as well as smaller scales through some portion of an inertial cascade. This will have to be done for a while, even if parameterizations ultimately are devised and tested for use in long-term simulations of slowly varying ocean circulation. In any event, it is hard to imagine validating any ocean model unless it produces measurables with at least the same length scales of the real ocean. And even the thermohaline circulation apparently has length scales of order the radius of deformation.

As was mentioned earlier, one mechanism that provides hope for further progress in modeling is that of computer performance increases. Even conservative estimates of speedups by massively parallel approaches to computing suggest that a factor of a thousand is likely in the next 10 years. If machines are properly exploited, many oceanographic modeling problems that are otherwise intractable can be solved. Previous limitations regarding domain size, resolution, simulation time, and sensitivity testing will be much less daunting than before.

Thus the future of global eddy-resolving ocean modeling over the next decade is justifiably optimistic. To the extent that the parallelism of modern computers can be effectively exploited, the oceanographic and climatic communities are well on their way toward routine global eddy-resolving modeling.

Acknowledgments. The authors thank Tom Bettge and Gary Strand of NCAR and Mike McCann of the Naval Postgraduate School for sustained technical contributions to the research. They also wish to thank Warren Washington and Bill Buzbee of NCAR for sustained administrative backing of this work. Finally, the authors are grateful to their colleagues at other institutions throughout the world for many valuable suggestions and comments during the course of this research. Fritz Schott and Arnold Gordon, in particular, helped by encouraging the investigation of the simulated thermohaline circulation; and Eric Firing aided in the interpretation of the equatorial deep jets. A.J.S. was supported by grants ATM-8705980 and OCE-8812472 from the National Science Foundation and by contract 079067-A-B1 from Battelle Pacific Northwest Laboratories of the U.S. Department of Energy. R.M.C. was partially supported by a Department of Energy grant from the Carbon Dioxide Research Program to NCAR. Computing resources were provided by the Scientific Computing Division of the National Center for Atmospheric Research. NCAR is sponsored by the National Science Foundation.

References

Bettge, T., An ocean model processor for climate studies, *NCAR Tech. Note TN-279+1A*, 31 pp., Natl. Cent. for Atmos. Res., Boulder, Colo., 1987.

Böning, C. W., R. Döscher, and R. G. Budich, Seasonal transport variation in the western subtropical North Atlantic: Experiments with an eddy-resolving model, *J. Phys. Oceanogr.*, *21*, 1271–1289, 1991.

Broecker, W. S., Unpleasant surprises in the greenhouse? *Nature*, *328*, 123–127, 1987.

Broecker, W. S., The great ocean conveyor, *Oceanography*, *4*, 79–89, 1991.

Bryan, F. O., and W. R. Holland, A high resolution simulation of the wind- and thermohaline-driven circulation in the North Atlantic Ocean, in *Parameterization of Small-Scale Processes, Proceedings of the 'Aha Huliko'a Hawaiian Winter Workshop*, edited by P. Muller and D. Henderson, pp. 99–115, University of Hawaii, Honolulu, 1989.

Bryan, K., A numerical method for the study of the world ocean, *J. Comput. Phys.*, *4*, 347–376, 1969.

Bryan, K., Accelerating the convergence to equilibrium of ocean-climate models, *J. Phys. Oceanogr.*, *14*, 666–673, 1984.

Bryan, K., Poleward buoyancy transport in the ocean and mesoscale eddies, *J. Phys. Oceanogr.*, *16*, 927–933, 1986.

Bryden, H. L., and E. C. Brady, Eddy momentum and heat fluxes and their effects on the circulation of the equatorial Pacific Ocean, *J. Mar. Res.*, *47*, 55–79, 1989.

Bryden, H. L., D. L. Roemmich, and J. A. Church, Ocean heat transport across 24°N in the Pacific, *Deep Sea Res.*, *38*, 297–324, 1991.

Chervin, R. M., and A. J. Semtner, An ocean modelling system for supercomputer architectures of the 1990's, in *Climate-Ocean Interactions*, edited by M. E. Schlesinger, pp. 87–95, Kluwer Academic, Boston, Mass., 1990.

Cox, M. D., A mathematical model of the Indian Ocean, *Deep Sea Res.*, *17*, 47–75, 1970.

Cox, M. D., A primitive equation three-dimensional model of the ocean, *Tech. Rep. 1*, Ocean Group, 250 pp., NOAA Geophys. Fluid Dyn. Lab., Univ., Princeton, N. J., 1984.

Dickson, R. R., E. M. Gmitrowicz, and A. J. Watson, Deep water renewal in the northern North Atlantic, *Nature*, *344*, 848–850, 1990.

England, M. H., On the formation of Antarctic Intermediate and Bottom Water in ocean general circulation models, *J. Phys. Oceanogr.*, in press, 1992.

Firing, E., Mean zonal currents below 1500 m near the equator, 159°W, *J. Geophys. Res.*, *94*, 2023–2028, 1989.

Flato, G., and W. D. Hibler III, On modeling pack ice as a cavitating fluid, *J. Phys. Oceanogr.*, in press, 1992.

FRAM Group, An eddy-resolving model of the southern ocean, *Eos Trans. AGU*, *72*, 169, 174–175, 1991.

Fu, L.-L., D. B. Chelton, and V. Zlotnicki, Satellite altimetry: Observing ocean variability from space, *Oceanography*, *1*(2), 4–11, 1988.

Godfrey, J. S., A Sverdrup model of the depth-integrated flow for the ocean allowing for island circulations, *Geophys. Astrophys. Fluid Dyn.*, *45*, 89–112, 1989.

Gordon, A., Interocean exchange of thermocline water, *J. Geophys. Res.*, *91*, 5037–5046, 1986.

Hall, M. H., and H. L. Bryden, Direct estimates and mechanisms of ocean heat transport, *Deep Sea Res.*, *29*, 339–359, 1982.

Haney, R. L., Surface thermal boundary condition for ocean circulation models, *J. Phys. Oceanogr.*, *1*, 241–248, 1971.

Hansen, D. V., and G. A. Maul, Anticyclonic current rings in the eastern tropical Pacific Ocean, *J. Geophys. Res.*, *96*, 6965–6979, 1991.

Hastenrath, S., Heat budget of tropical ocean and atmosphere, *J. Phys. Oceanogr.*, *10*, 159–170, 1980.

Hellerman, S., and M. Rosenstein, Normal monthly wind stress over the world ocean with error estimates, *J. Phys. Oceanogr.*, *13*, 1093–1104, 1983.

Kawase, M., Establishment of deep ocean circulation driven by deep-water penetration, *J. Phys. Oceanogr.*, *17*, 2294–2317, 1987.

Killworth, P. D., D. J. Webb, D. Stainforth, and S. M. Paterson, The development of a free-surface Bryan-Cox-Semtner ocean model, *J. Phys. Oceanogr.*, *21*, 1333–1348, 1991.

Levitus, S., Climatological atlas of the world oceans, *NOAA Prof. Paper 13*, U.S. Govt. Print. Off., Washington, D. C., 1982.

Maier-Reimer, E., and K. Hasselmann, Transport and storage of CO_2 in the ocean—An inorganic ocean circulation carbon cycle model, *Clim. Dyn.*, *2*, 63–90, 1987.

Mantyla, A. W., and J. L. Reid, Abyssal characteristics of the world ocean waters, *Deep Sea Res.*, *30*, 805–833, 1983.

Meehl, G. A., W. M. Washington, and A. J. Semtner, Experiments with a global ocean model driven by observed atmospheric forcing, *J. Phys. Oceanogr.*, *12*, 301–312, 1982.

Metzl, N., B. Moore, and A. Poisson, Resolving the intermediate and deep advective flows in the Indian Ocean by using temperature, salinity, oxygen, and phosphate data: The interplay of biogeochemical and geophysical tracers, *Palaeogeogr. Palaeoclimatol. Palaeoecol.*, *89*, 81–111, 1990.

Pacanowski, R. C., and S. G. H. Philander, Parameterization of vertical mixing in numerical models of tropical oceans, *J. Phys. Oceanogr.*, *11*, 1443–1451, 1981.

Ponte, R. M., and J. Luyten, Analysis and interpretation of deep equatorial currents in the central Pacific, *J. Phys. Oceanogr.*, *19*, 1025–1038, 1989.

Rintoul, S. R., South Atlantic interbasin exchange, *J. Geophys. Res.*, *96*, 2675–2692, 1991.

Sandwell, D. T., and B. Zhang, Global mesoscale variability from the Geosat exact repeat mission: Correlation with ocean depth, *J. Geophys. Res.*, *94*, 17,971–17,984, 18,239, 1989.

Sarmiento, J. L., and K. Bryan, An ocean transport model for the North Atlantic, *J. Geophys. Res.*, *87*, 394–408, 1982.

Schott, F. A., and C. W. Böning, The WOCE model in the western equatorial Atlantic: Upper layer circulation, *J. Geophys. Res.*, *96*, 6993–7004, 1991.

Semtner, A. J., An oceanic general circulation model with bottom topography, *Tech. Rep. 9*, 99 pp., Dep. of Meteorol., Univ. of Calif., Los Angeles, 1974.

Semtner, A. J., A numerical study of sea ice and ocean circulation in the Arctic, *J. Phys. Oceanogr.*, *17*, 1077–1099, 1987.

Semtner, A. J., and R. M. Chervin, A simulation of the global ocean circulation with resolved eddies, *J. Geophys. Res.*, *93*, 15,502–15,522, 15,767–15,775, 1988.

Semtner, A. J., and R. M. Chervin, Environmental effects on acoustic measures of global ocean warming, *J. Geophys. Res.*, *95*, 12,973–12,982, 13,551–13,552, 1990.

Stammer, D., and C. W. Böning, Mesoscale variability in the Atlantic Ocean from Geosat altimetry and WOCE high resolution numerical modelling, *J. Phys. Oceanogr.*, in press, 1992.

Stommel, H., and A. B. Arons, On the abyssal circulation of the world ocean, II, An idealized model of the circulation patterns and amplitude in ocean basins, *Deep Sea Res.*, *6*, 217–233, 1960.

Toggweiler, J. R., K. Dixon, and K. Bryan, Simulations of radiocarbon in a coarse-resolution world ocean model, 1, Steady state prebomb distributions, *J. Geophys. Res.*, *94*, 8217–8242, 1989.

Trenberth, K. E., Mean annual poleward energy transports by the ocean in the southern hemisphere, *Dyn. Atmos. Oceans*, *4*, 57–64, 1979.

Warren, B. A., Deep circulation of the world ocean, in *Evolution of of Physical Oceanography*, edited by B. A. Warren and C. Wunsch, pp. 6–41, MIT Press, Cambridge, Mass., 1981.

Weaver, A. J., and E. S. Sarachik, On the importance of vertical resolution in certain ocean general circulation models, *J. Phys. Oceanogr.*, *20*, 600–609, 1990.

Wijffels, S. E., R. W. Schmitt, H. L. Bryden, and A. Stigebrandt, On the transport of freshwater by the oceans, *J. Phys. Oceanogr.*, *22*, 155–162, 1992.

Worthington, L. V., On the North Atlantic circulation, *Johns Hopkins Oceanogr. Stud.*, *6*, 110 pp., 1976.

Wyrtki, K., and B. Kilonsky, Mean water and current structure during the Hawaii-to-Tahiti Shuttle Experiment, *J. Phys. Oceanogr.*, *14*, 242–254, 1984.

R. M. Chervin, National Center for Atmospheric Research, Boulder, CO 80307.

A. J. Semtner, Jr., Department of Oceanography, Naval Postgraduate School, Monterey, CA 93943.

(Received September 23, 1991;
revised December 24, 1991;
accepted January 2, 1992.)